

# 3D STROKE CALCULATION AND APPLICATION USING 6-DEGREE-OF-FREEDOM SENSORS

Suk Jae (Steve) Ham, Ben Meyers

Toyota Motor Engineering & Manufacturing North America  
United States of America

Paper Number 19-0185

## ABSTRACT

Time history of movement (stroke) is crucial information for crash test analysis. The stroke is often calculated from double integration of linear acceleration data when direct measurement by a potentiometer is impossible. But this method may not be accurate for the cases with large rotations. Newer crash tests like IIHS small overlap and NHTSA oblique involve large rotation, creating 3-dimensional (3D) occupant motions compared to front rigid barrier tests which are primarily 2D events. To help overcome some of the challenges posed by newer crash tests, the authors developed a method to calculate accurate 3D motion with 6-DOF (Degree-of-Freedom) instrumentation including angular rate sensors (ARS).

The calculation of accurate 3D position and orientation for a rigid body requires data collection of 6-DOF: linear acceleration ( $a_x, a_y, a_z$ ) and angular velocity ( $\omega_x, \omega_y, \omega_z$ ). The mathematical calculation to account for rotation of a rigid body was done by using the screw-axis method. The quaternion was calculated using numerical integration via the 4th-order Runge-Kutta method.

A dynamic component test was designed and conducted with a linear impactor to validate the 3D stroke calculator. The test set up included a 6-DOF sensor pack mounted on a polyethylene stick with an offset. The stick was mounted on a base, which was pushed by a linear impactor with controlled speed. The sensor experienced 3D motion when the stick was decelerated by the base impacting a honeycomb backstop.

This method of 3D rigid body tracking has various crash testing applications. The authors compared occupant head kinematics among three different frontal offset crash modes. A finding of the study was that one test mode resulted in more driver head stroke (relative to vehicle interior) compared to the other two crash test modes. The maximum head stroke, compared to the least, was more by 64% (longitudinal) and 49% (lateral).

## BACKGROUND AND PURPOSE

For crashworthiness engineers, time history of ATD (Anthropomorphic Test Devices) movement is necessary information to help analyze the performance of restraint systems. The movement, or stroke, is often calculated from double integration of linear accelerometers when direct measurement by a potentiometer is not available or too difficult. But this double integration method is may not be accurate enough for the ATD motions with large rotations. For example, a 5th%ile Hybrid III ATD in the front passenger seat experiences rotation (pitching) during rebound after loading the front passenger airbag (Figure 1) in NCAP front crash tests. As a simple solution, a 2D rotation matrix can be used for this type of crash test if pitching angular velocity was measured during the test.

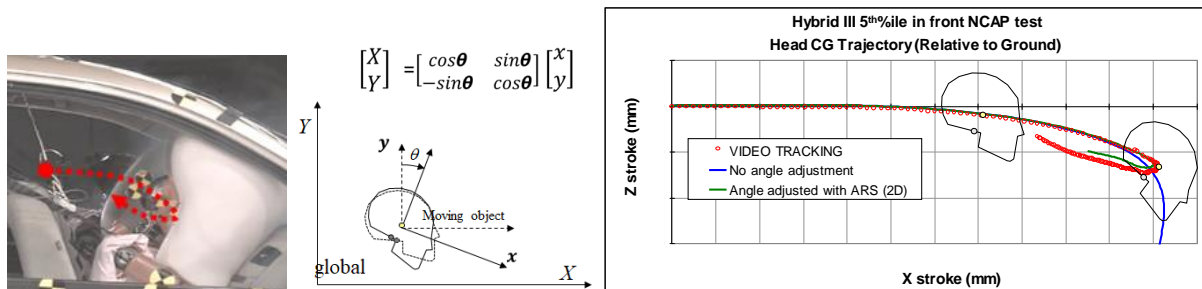


Figure 1. 5th%ile Hybrid III head stroke calculation for front impact crash test.

However, newer frontal crash tests like IIHS small overlap and NHTSA oblique tests, which have less overlap with the impact barriers, involve larger vehicle rotations than full-overlap frontal crash test. These test modes create complex 3D occupant motions compared to front rigid barrier tests. One example is the new NHTSA oblique test shown in Figure 2. In this test, the driver head experiences large rotation and no camera view is good for video tracking. Therefore, getting accurate head movement time history is very challenging. To overcome the challenge to calculate accurate 3D strokes in newer crash tests, the authors developed a calculator to get accurate motion with currently available instrumentation.

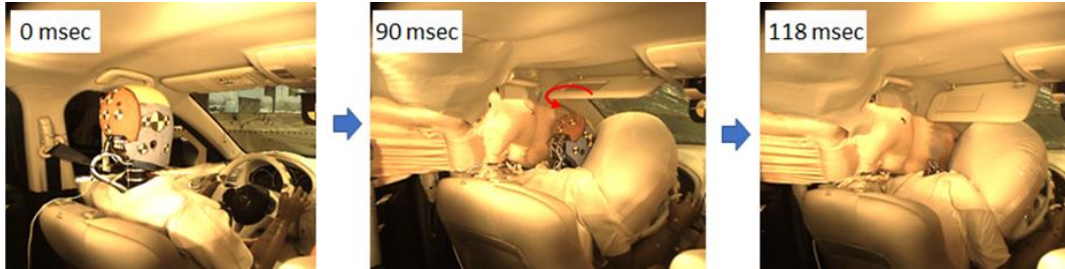


Figure 2. An example of NHTSA Oblique front impact test with large rotation of ATD head [1]

## THEORY AND METHOD

To get accurate 3D position of a moving rigid body, like an ATD head in an offset crash test, all three linear accelerations need to be corrected by calculating three Euler angles by using measured angular velocities [2] before time integration or displacement (Figure 3).

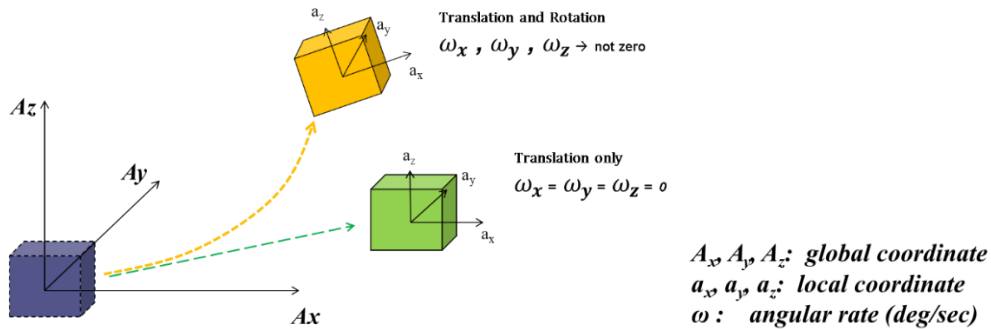


Figure 3. Consideration of angular rates for accurate 3-dimensional motions.

If all three angular velocities ( $\omega_x, \omega_y, \omega_z$ , deg/second) are measured, along with linear accelerations, correction of linear acceleration can be done with a 3D rotation matrix  $[R]$  in figure 4. There are several methods to calculate the rotation matrix, but two methods, successive rotation and screw axis methods [3] were considered in this paper.

$$\begin{bmatrix} X \\ Y \\ Z \end{bmatrix} = [R] \begin{bmatrix} x \\ y \\ z \end{bmatrix}$$

Figure 4. Rotation matrix to adjust linear accelerations (X, Y, Z = corrected with angle and x, y, z = not corrected) [2].

The successive rotation angle method rotates 3 axes continuously to achieve a new position in each time step using angular rate data as shown in Figure 5. It is basically a 3D version of 2D adjustment shown in Figure 1. But this

method has two limitations which are Gimbal lock and complexity of calculation [2]. Gimbal lock is the case when there is more than one solution to the Euler angles calculated from angular velocities. The other challenge point is that this method requires complicated coding which could result in a higher chance of error, leading to a difficult debug process.

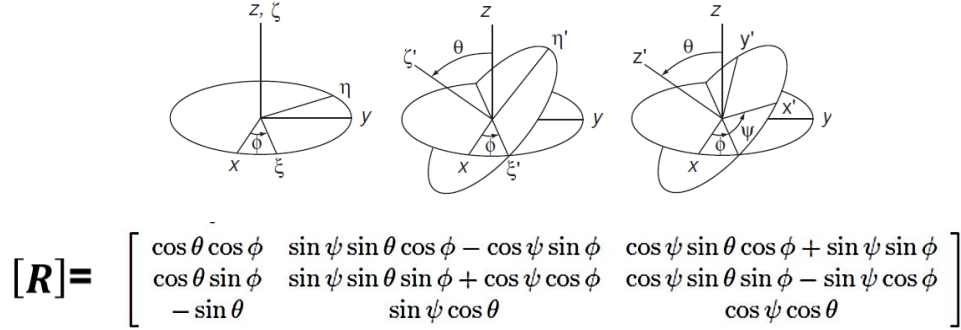
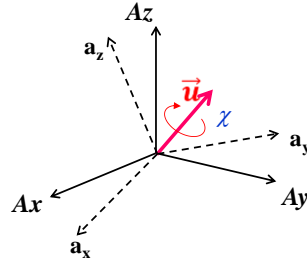


**Figure 5. Successive rotation angle method: Euler angles ( $\phi$ ,  $\theta$ ,  $\psi$ ) and associated rotational matrix equation [2], [3].**

The problem of Gimbal lock can be resolved by using Euler parameters, which are unit quaternions [2]. The screw axis method uses Euler parameters to calculate the 3D rotation matrix as shown in Figure 6. The unit vector  $\vec{u}$  (Figure 6) is the axis for final rotation angle  $\chi$  resulted from 3 Euler angle rotations. This study used the screw axis method for its simplicity in programming and freedom from Gimbal lock.



$$q_0 = \cos\left(\frac{\chi}{2}\right), \quad \vec{q} = [q_1, q_2, q_3] = \vec{u} \sin\left(\frac{\chi}{2}\right), \quad q_0^2 + q_1^2 + q_2^2 + q_3^2 = 1$$

$$[R] = \begin{pmatrix} q_0^2 + q_1^2 - q_2^2 - q_3^2 & 2(q_1q_2 - q_0q_3) & 2(q_1q_3 + q_0q_2) \\ 2(q_2q_1 + q_0q_3) & q_0^2 - q_1^2 + q_2^2 - q_3^2 & 2(q_2q_3 - q_0q_1) \\ 2(q_3q_1 - q_0q_2) & 2(q_3q_2 + q_0q_1) & q_0^2 - q_1^2 - q_2^2 + q_3^2 \end{pmatrix}$$

**Figure 6. Screw axis method: Euler parameters and rotation matrix equation with quaternions [2], [3]**

To get the rotational matrix  $[R]$ ,  $q_0$  and  $\vec{q}$  need to be calculated using angular velocities measured in the physical test. Quaternions are a function of angular velocity, and they form a series of ordinary differential equations as shown in Figure 7. Angular velocities  $\omega_x$ ,  $\omega_y$  and  $\omega_z$  are measured by ARS on a rigid body.

$$\begin{pmatrix} \dot{q}_0 \\ \dot{q}_1 \\ \dot{q}_2 \\ \dot{q}_3 \end{pmatrix} = \frac{1}{2} [Q] \begin{pmatrix} 0 \\ \omega_b \end{pmatrix}, \quad \text{Where, } \omega_b = \begin{pmatrix} \omega_x \\ \omega_y \\ \omega_z \end{pmatrix} \quad \text{and} \quad [Q] = \begin{bmatrix} q_0 & -q_1 & -q_2 & -q_3 \\ q_1 & q_0 & -q_3 & q_2 \\ q_2 & q_3 & q_0 & -q_1 \\ q_3 & -q_2 & q_1 & q_0 \end{bmatrix}$$

**Figure 7. Time derivative of quaternions [2]**

The authors calculated quaternions using numerical integration via the 4<sup>th</sup> order Runge-Kutta method [4]. Four unknown variables (quaternions) were expressed as a system of 4 ordinary differential equations, **f1**, **f2**, **f3** and **f4** shown below. The authors used MS Excel® to calculate quaternions, the rotational matrix **[R]** and the adjusted position of the rigid body. The inputs were 6-DOF data (3 linear accelerometers and 3 ARS) of two objects (i.e. ATD head and vehicle body) and the outputs are the corrected stroke of both objects.

$$\dot{q}_0 = \frac{-q_1\omega_x - q_2\omega_y - q_3\omega_z}{2} = f1$$

$$\dot{q}_1 = \frac{q_0\omega_x - q_3\omega_y + q_2\omega_z}{2} = f2$$

$$\dot{q}_2 = \frac{q_3\omega_x + q_0\omega_y - q_1\omega_z}{2} = f3$$

$$\dot{q}_3 = \frac{-q_2\omega_x + q_1\omega_y + q_0\omega_z}{2} = f4$$

## VALIDATION

To validate the calculation method, a component test was devised to create a complex motion path of a known point. The component test setup allowed for accurate video analysis at multiple angles (top & side) of this point, as seen in Figures 8 and 9. At this known point, a 6-DOF sensor pack was installed. The purpose of the test was to calculate the path of the point using the 3D calculator with the 6-DOF sensor pack, and then compare the calculation result to the known motion of that point based on accurate video tracking.

The component test was comprised of a platform that could slide on tracks toward a rigid wall which would stop the platform's motion. A section of honeycomb was fixed to the wall to reduce the peak g experienced by the platform. A 5/8" diameter flexible plastic (polyethylene terephthalate) shaft approximately 2 feet in length, extending vertically, was attached to the platform. At the top of the shaft was a plate where the 6-DOF pack was mounted. The sensor pack was aligned to the platform so that the platform's sliding motion would be the X-axis, vertical from gravity would be the Z-axis, and the remaining orthogonal axis would be the Y-axis. A cantilever mass was attached to the shaft, offset in the Y-axis at a height of 18" from the base. The purpose of the mass was to introduce a twisting motion of the shaft when the platform was stopped by the rigid wall.

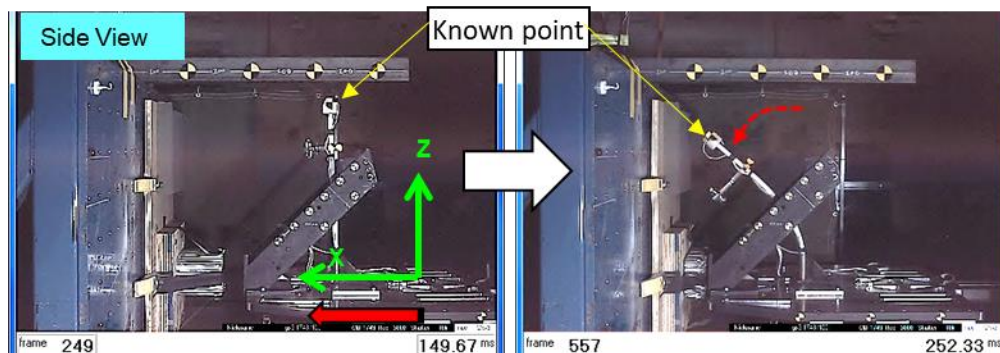


**Figure 8. Side view of component test before impact with the rigid wall (left) and when the shaft is at peak forward rotation (right).**



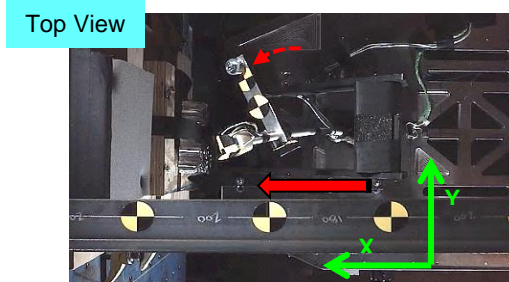


**Figure 9. Top view of component test showing axial rotation of the shaft.**

The result of the component test matched the calculation result explained in this paper as shown in Figure 10. Red color is the calculated stroke and blue is by video analysis. The calculated stroke data showed close correlation to video analysis. For comparison, the calculation result without 3D angular correction is also shown (green).

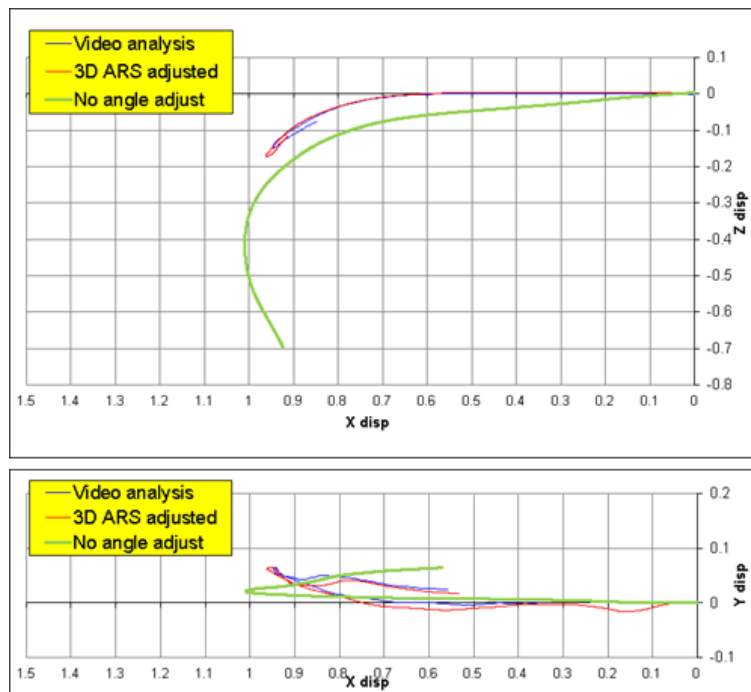


**Figure 10. Comparison of results observed by video analysis vs 3D angular rate (ARS) correction calculation method vs original calculation method without angle adjust.**

## APPLICATION EXAMPLES AND DISCUSSIONS

The authors applied the 3D calculation method to two crash tests. The first application was a comparison of the front passenger head trajectory in an NCAP frontal impact sled test. In most cases, off-board video tracking can provide accurate head stroke information but, in some cases, the video target on the head C.G. becomes invisible due to the passenger airbag or the side curtain airbag blocking the camera view. In either case, 3D stroke calculation can be an alternative to video tracking. Figure 11 shows an example of this application to a front NCAP case study. As shown in Figure 11, maximum head stroke in the longitudinal and vertical axis are distinguishable from test to test, even though the head target was not visible.

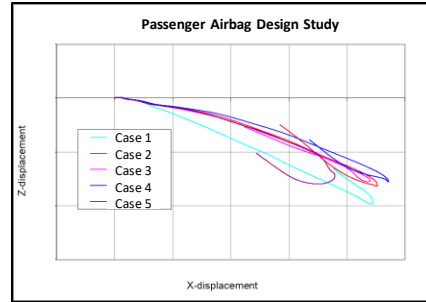


**Figure 11. Example of head stroke analysis (Hybrid III 5<sup>th</sup> percentile head stroke in front NCAP sled test).**

Another example was to compare a driver ATD head motion in three different frontal offset crash modes (TESTS A, B and C). The goal was to compare the maximum head stroke (relative to vehicle) in three (x, y and z) directions. The three test modes had different impact speeds, barrier types and amounts of overlap. Two of the tests used Hybrid III 50<sup>th</sup> percentile and the other used a THOR 50<sup>th</sup> percentile. All three tests were done with the same vehicle model for direct comparison. Data from 6-DOF sensors were measured for both the ATD head and the vehicle floor to calculate relative stroke. Head stroke results in side and top views are shown in Figure 12. In the case of TEST A, it had the largest stroke observed in all three directions. Compared to test B, maximum stroke was greater by 64% in the longitudinal direction and 49% in the lateral direction. Also, the head moved up (relative to vehicle interior) in early timing due to vehicle pitching.

The application is not limited to the examples shown in this paper. Crash tests with large vehicle rotation can get benefit from this 3D calculator as long as 6-DOF data were measured properly.

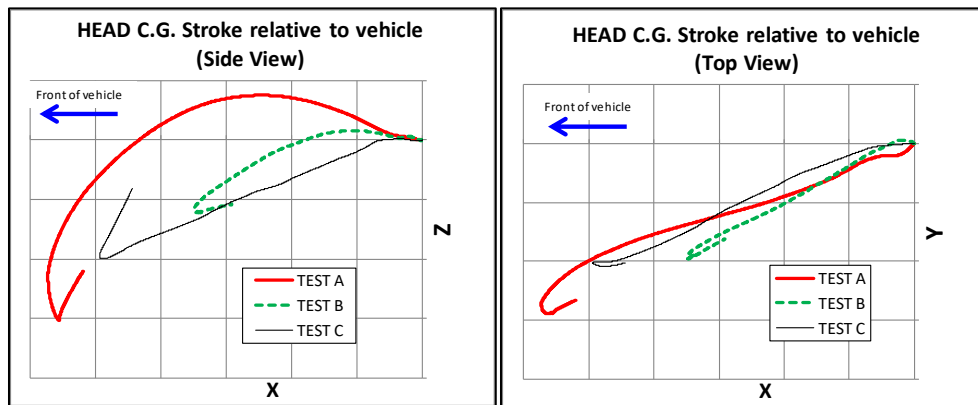


**Figure 12. Example of head stroke calculation method – Comparison ATD head CG stroke relative to vehicle for three different frontal offset crash modes.**

## CONCLUSION

The 3D stroke calculator was developed using the screw-axis method and 4<sup>th</sup>-order Runge Kutta integration in this study. The calculator was validated by component testing, which demonstrated more accuracy than double-integration methods without angular correction. Example studies using the 3D calculator provided accurate stroke of an ATD head relative to the vehicle which could be valuable data for occupant restraint strategy and performance analysis. Furthermore, this 3D calculator could be used on any two rigid-body system with 3D rotational kinematics as long as 6-DOF sensor data and initial condition are measured.

## LIMITATIONS

Theoretically, the method looks promising but there are limitations in actual application. The first limitation is that accurate initial conditions (position and angle relative to the ground) are necessary because this method is a typical initial value problem with explicit time integration. Also, the authors observed that the ARS could give invalid data if the ARS did not include shock-resistance feature or if the sensor mount location on the vehicle was involved in local deformation. The authors recommend the use of shock-resistant ARS mounted in an area with no deformation on the vehicle.

## REFERENCES

- [1] National Highway Traffic Safety Administration, “Vehicle Crash Test Database” (<https://www-nrd.nhtsa.dot.gov/database/VSR/veh/QueryTest.aspx>). Accessed on FEB 13, 2019.
- [2] A. L. Schwab, “How to draw Euler Angles and Utilize Euler Parameters”. ASME 2006 IDETC/CIE, 2006.
- [3] TNO, MADYMO version 5 theory manual, 1999.
- [4] Chapra, S. C., Canale, R.P, Numerical Methods for Engineers, 6th ed., page 707~737, McGraw-Hill, New York, N.Y., 2010.
- [5] Jianping Wu et al, “Using Triaxial Angular Rate Sensor and Accelerometer to Determine Spatial Orientation and Position in Impact Tests”, SAE 2009-01-0055.

# ASSESSING INJURY RISK OF CAR OCCUPANTS ON REARWARD FACING SEATS IN A FULL FRONTAL IMPACT – SLED TESTS IN A GENERIC TEST ENVIRONMENT

**Harald Zellmer**

**Felix Manneck**

Autoliv B.V. & Co. KG

Germany

Paper Number 19-0201

## ABSTRACT

With the introduction of fully-automated vehicles, new seating configurations of the passenger compartment have been proposed. Rearward facing front seats are considered to provide so-called living room seating. At least as long as conventional and fully-automated vehicles share the same roads in mixed traffic, crashes may occur. Occupant protection on a rearward facing seat must therefore be on the same level as on a forward facing seat to comply with legal requirements. In order to assess dummy response on a rearward facing seat in a 56 km/h full frontal impact, sled tests were performed, analysed, and discussed.

A total of 23 sled tests in three series with a Hybrid III 50<sup>th</sup> percentile adult male dummy were performed to simulate a vehicle frontal impact against a rigid barrier at impact speeds up to 56 km/h. In the first test series, a serial vehicle seat was used, but it showed already considerable deformation at an impact speed of 40 km/h. Therefore, a generic concept seat was developed. In the second test series, the concept seat was tested and tuned to enable it to perform tests at the target impact speed of 56 km/h. In the third series, tests to investigate repeatability were performed. Dummy loadings at 56 km/h were compared with reference values from legislation and literature. Focus was set on thorax and lumbar spine loadings.

For a qualified interpretation of dummy loadings and the performance of the restraint system, the crash was divided into three phases: (1) impact phase until the maximum dummy rearward displacement, (2) dummy rebound before interaction with the seat belt, and (3) dummy in rebound and interaction with the seat belt. The impact phase (1) is characterized by the highest 3 ms chest acceleration, close to 60 g in 56 km/h tests. Notably, this was the loading closest to the injury assessment reference value (IARV). The lumbar spine was mainly loaded in compression with forces rising up to 5.8 kN. Chest deflection of about 8 mm was caused by inertia of the dummy rib cage. The rebound phase before interaction (2) did not show any substantial dummy loading. The rebound interaction phase (3) was influenced by the seat belt system, chest deflection ranged from 5 mm in the test with lap belts to 19 mm in the test with two crossed shoulder belts (crisscross belt). The viscous criterion was below 0.1 m/s in all tests. Overall, the tests showed good repeatability and the ability of the generic concept seat to control dummy kinematics.

A limitation of our study is, that only full frontal loading directions were studied, dummy kinematics of oblique impact direction, simulating e.g.  $\pm 30^\circ$  impacts to the barrier, were not included. The head rest was not in focus of our investigation and the head was fixed to the head rest without any gap in between.

## INTRODUCTION

The development of automated driving systems of SAE levels 4 and 5 [1] allows for new seating options in automobiles. Swivel front seats are desirable to provide so-called living room seating [2]. With this, the front row passengers would sit on a rearward facing seat. At least as long as conventional and fully-automated vehicles share the same roads, crashes may occur. Occupant protection on a rearward facing seat must therefore be at least on the same level as on a forward facing seat.

Although few car models are equipped with rearward facing seats, e.g. Volkswagen Caravelle, Mercedes Viano, or several models of ambulance cars and motorhomes, almost no accident analysis focusing on adult car occupants on rearward facing seats is published. An analysis of the German In-Depth Accident Study (GIDAS) identified only five cases with rearward facing adult occupants in ECE M1 vehicles. Only one occupant on a

rearward facing seat was injured (MAIS 2), but in all collisions the speed change  $\Delta v$  of the impacted vehicle was below 25 km/h [3].

Sled testing in this occupant loading direction is mainly to determine neck injury risk in low speed rear impacts. Further, some studies were performed to determine injury risk in so-called high speed rear impacts with a  $\Delta v$  of up to 40 km/h [4, 5]. Pulses for these studies are to represent loadings in a car to car rear impact and are much softer than pulses in a frontal car to car or car to barrier collision at the same  $\Delta v$ .

Recently simulations with the human FE model THUMS on rearward facing seats in full frontal impact conditions were performed. Kitagawa et al. [6] described occupant kinematics on rearward facing and conventional seats, Xin Jin et al. [7] compared injury risk in different loading directions and concluded that the rearward facing seating position has the lowest injury risk.

The scope of our work was to study occupant loading on rearward facing seats in sled tests. For this, we established a generic test environment. The initial requirements were as follows:

1. The test setup should be sufficiently stable to withstand a stiff crash pulse taken from a small vehicle in a full frontal crash according to FMVSS 208 [8] at 56 km/h.
2. The rearward displacement of the back rest during crash should be adjustable and limited to about 200 mm rearward displacement in order to avoid possible occupant head contact to the windscreen.
3. The environment should be simple in order to build up and validate a finite element model for further investigations.

The dummy used for the investigation was a Hybrid III 50<sup>th</sup> percentile adult male. For the rearward loading direction of this dummy, injury reference assessment values (IARV) only exist for low speed rear impact. These are however to protect from AIS 1 injuries and are thus not applicable for high speed impacts we are looking at. In a first assumption, we applied IARV for the frontal impact of this dummy. It must be pointed out, that this can only be a first approach as the dummy was not validated for this loading direction. In the first step, we were concentrating on injury assessment of chest and lumbar spine as loading to these body parts mainly dependent on the back rest performance. Head and neck loadings are mainly dependent on the head rest and should be investigated in a next step. As a guideline, IARV given in European or US legislation were taken into account first, the respective lower value was taken as our reference for this paper. For the chest the 3 ms chest acceleration clip of 60 g was taken from FMVSS 208 [8], for chest deflection and the viscous criterion the values were taken from ECE-R 137 (42 mm and 1 m/s) [9]. No reference values in automotive regulations exist for the lumbar spine forces. For helicopter emergency landing the European Aviation Safety Agency (EASA) specifies a limit in compression of 6674 N [10]. An internal specification of General Motors (GM) [11] specifies 12.2 kN in tension and 6.4 kN in compression. The compression value is well comparable to the EASA requirement and was used together with the value for tension as reference in this paper.

To have control of all loadings to the dummy we also used IARV for other body parts. A list of all used IARV and its source can be found in the Appendix.

## METHOD

All the tests were performed on a deceleration sled using either a hydraulic brake or a bending bar brake to generate the crash pulse. The seat was mounted to the sled and a Hybrid III 50<sup>th</sup> percentile male dummy placed on it.

In the first tests series, a serial production seat was used. The dummy was seated according to the definition in [12]. The speed was increased until a  $\Delta v$  of 40 km/h was reached. Already at  $\Delta v$  of 40 km/h a considerable deformation of the seat back occurred and it was decided to design and build a generic seat which could withstand a  $\Delta v$  of at least 60 km/h which compares to a barrier impact speed of 56 km/h.

Figure 1 shows the generic concept seat that was designed and built. It consists of a stiff seat pan which has a steel frame with a surface of acrylic glass and a back rest which has a frame of standard aluminium profiles. This was chosen in order to easily replace in case of damage in crash. The seat back frame has a polycarbonate shell surface to support the back of the dummy. All the surfaces which are in contact with the dummy have a padding of at least one layer of comfort foam. In the second test series, which was the first one with the generic seat, a standard head rest supported by an aluminium frame at its back was used. This design showed not to be

very reliable and in the third test series a stiff steel frame head rest was implemented. It has a wooden plate towards the dummy's head and three layers of comfort foam. The dummy head is taped to the head rest to avoid a gap between both. The back rest is fixed to the sled ground plate by ball bearings at both sides. The torso angle of the dummy is set to 25°. A controlled rearward displacement of the back rest during crash is provided by each two layers of seat belt webbing of 12% elongation at 10 kN and of a length of 1200 mm on both sides of the back rest. The other side of the webbing is fixed to a steel frame mounted to the sled. At the upper cross member of the back rest, seat belt systems can be mounted at each side.

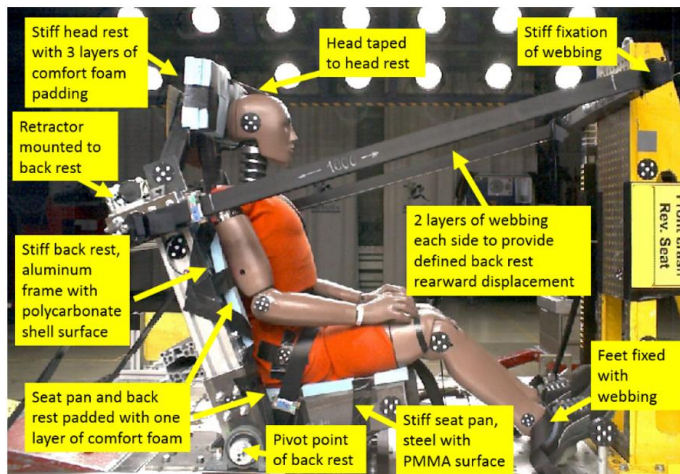


**Figure 1. Generic seat in its final version**

## TEST SETUP

In test series 1, the standard production seat was used. In the first four tests,  $\Delta v$  was increased from 17 km/h as given in FMVSS 202a [12] to 40 km/h. A standard three point belt system was used with the upper shoulder belt fixed to a stiff B-pillar mounted on the sled and the lower anchorages fixed to the seat. At a  $\Delta v$  of 40 km/h, the deformation of the seat back was so large that no further increase in speed was done. The dynamic rear displacement at the upper end of the back rest was with 250 mm above our target of 200 mm. In order to study influencing parameters, three more tests at  $\Delta v$  of 40 km/h were performed, this included the variation of the back rest angle and of seat belt parameters. To investigate the influence of the back rest angle, the back rest was set to its most upright position with otherwise identical parameters to the previous test. The influence of the belt restraint system was investigated in two further tests: One test was done with a lap belt only, the other with two crossed shoulder belts (crisscross belt without lap belt portion) attached directly to the top of the seat and to the anchor plate on the seat frame.

The second tests series was performed with the generic seat. In the first six tests, the speed was increased from a  $\Delta v$  of 40 km/h in 5 km/h increments to about 60 km/h and an occupant load criterion (OLC) [13] of about 36 g. A seat-integrated three-point belt system was used in the tests, mounted to the upper cross member of the back rest. The tests allowed further improvements to be made. There were among others the stiffening of the production head rest and the optimisation of the webbing parameters for the controlled back rest rearward displacement. After six tests, the target  $\Delta v$  of 60 km/h and OLC of 36 g was attained and two additional tests to study the influence of the restraint system were performed, cf. Table 2. The additional belt systems tested were a lap belt only system and a standard 3-point belt with additional shoulder belt at the other shoulder (crisscross belt).

The focus of test series 3 was to determine repeatability and to provide reliable data for the validation of a finite element model. In contrast to the first two series, in which the crash pulses were generated by a hydraulic brake system, the tests in series 3 were performed with a bending bar brake system. This provided a better repeatability of the crash pulses. The pulse chosen had an OLC of 31.5 g and thus was softer than the pulse used in series 3. The first two tests in this series were performed with a seat belt retractor pretensioner. The second two tests were without belt system and performed mainly for the FE model set-up. A pairwise comparison of the tests data already showed a good repeatability. Therefore, a series of four identical tests were performed with a standard three point belt system to better quantify repeatability.



## TEST RESULTS

The results of test series 1 are shown in Table 1. Tests 1.1 to 1.4 were performed to access the limit of the seat. It was decided not to exceed  $\Delta v$  of 40 km/h and a small parameter study was done at this speed. All injury assessment values (IAV) were well below its reference values. As can be seen in test 1.5, a more upright seating position slightly reduced chest acceleration. The lumbar spine was mainly loaded in tension, in test 1.6 the dummy was mainly restrained with a shoulder belt at each side. This decreased tension in the lumbar spine. However, the effect was not as big as expected, the main restraint of the dummy was provided by the seat itself. It is interesting to mention, that we measured not only chest deflection but also chest extension. This was possibly due to the back rest frame which pushed the dummy ribs forward. At higher  $\Delta v$  a part of the effect is compensated by the inertia of the ribs being pushed backwards in the crash.

**Table 1.**  
*Test series 1, test setups and injury assessment values*

Test	$\Delta V$	Backrest Angle (Torso Angle)	Belt System	Chest 3 ms / g	Chest defl. / mm	Chest ext. / mm	Lumbar spine tension / kN	Lumbar spine comp. / kN
1.1	17.3 km/h	22.1° (25°)	Normal Seat Belt	18	3	12	1.1	0.3
1.2	24 km/h	22.1° (25°)	Normal Seat Belt	27	4	14	1.4	0.8
1.3	33 km/h	22.1° (25°)	Normal Seat Belt	30	6	3	1.2	0.7
1.4	40 km/h	22.1° (25°)	Normal Seat Belt	31	0	4	1.9	0.2
1.5	40 km/h	15.6° (N/A)	Normal Seat Belt	27	1	3	1.9	0.3
1.6	40 km/h	22.1° (25°)	Lap Belt only	31	0	8	2.3	0
1.7	40 km/h	22.1° (25°)	CrissCross w/o Lap Belt	29	1	5	1.3	0.3

The test parameters of test series 2 are shown in Table 2. Injury assessment values are not given in the table, as several parameters of the seat were changed in the first six tests. In tests 6 to 8 the same belt parameters as in test series 1 were investigated.

**Table 2.**  
*Test series 2, test setups*

Test	$\Delta V$	OLC	Belt System
2.1	40 km/h	20.0 g	Seat integrated 3-point belt
2.2	45 km/h	24.7 g	Seat integrated 3-point belt
2.3	50 km/h	29.9 g	Seat integrated 3-point belt
2.4	55 km/h	28.0 g	Seat integrated 3-point belt
2.5	~ 60 km/h	33.5 g	Seat integrated 3-point belt
2.6	60 km/h	36.1 g	Lap Belt only
2.7	60 km/h	36.6 g	Seat integrated CrissCross Belt
2.8	60 km/h	35.2 g	Seat integrated 3-point belt

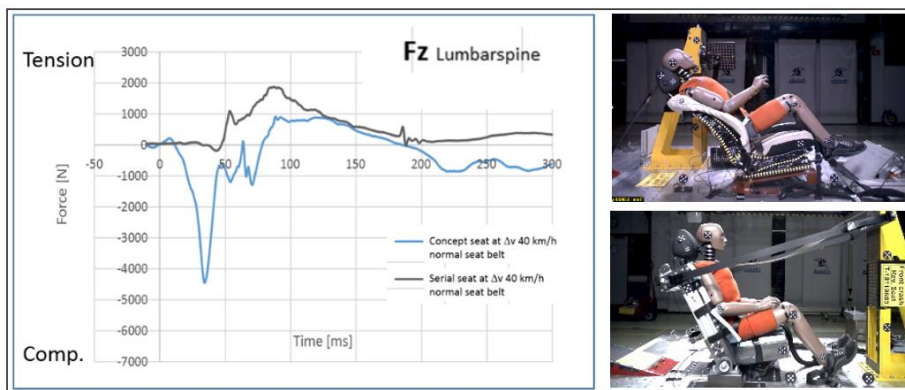


**Figure 2.** Comparison of lumbar spine forces of tests at  $\Delta v$  40 km/h with the serial and the generic seat. The upper right picture shows the serial seat at its maximum spine tension (90 ms), the lower right picture the concept seat at its maximum compression at 34 ms

First it has to be mentioned that the dummy kinematic in the generic seat differed from that in the serial seat (Figure 2). In the serial seat the spine was mainly loaded in tension, the dummy pelvis was restrained by the seat back and the upper part of the torso could move up. The generic seat back has a plain surface and the whole body could freely move up. The pelvis pushed the torso and caused compression in the spine.

In contrast to the serial seat, the concept seat showed a considerable rebound of the back rest which is due to elasticity in the webbing and the dummy fell in to the restraint system in rebound. Therefore, it is useful to divide the crash into three phases, similar as earlier done for the low speed rear impact [14]:

- Phase 1:** From the beginning (t = 0 ms) to the time when the maximum shoulder/arm-joint rearward displacement occurs, this is at about 60 ms in series 2 & 3 with  $\Delta v$  60 km/h.
- Phase 2:** From the end of Phase 1 until the shoulder/arm-joint passes its initial x-plane position (relative to the sled) or the dummy starts to be restraint by the seat belt (whatever occurs first), in series 2 & 3 the first happen at about 100 ms.
- Phase 3:** From end of Phase 2 until the end of the dummy loading at about 300 ms.

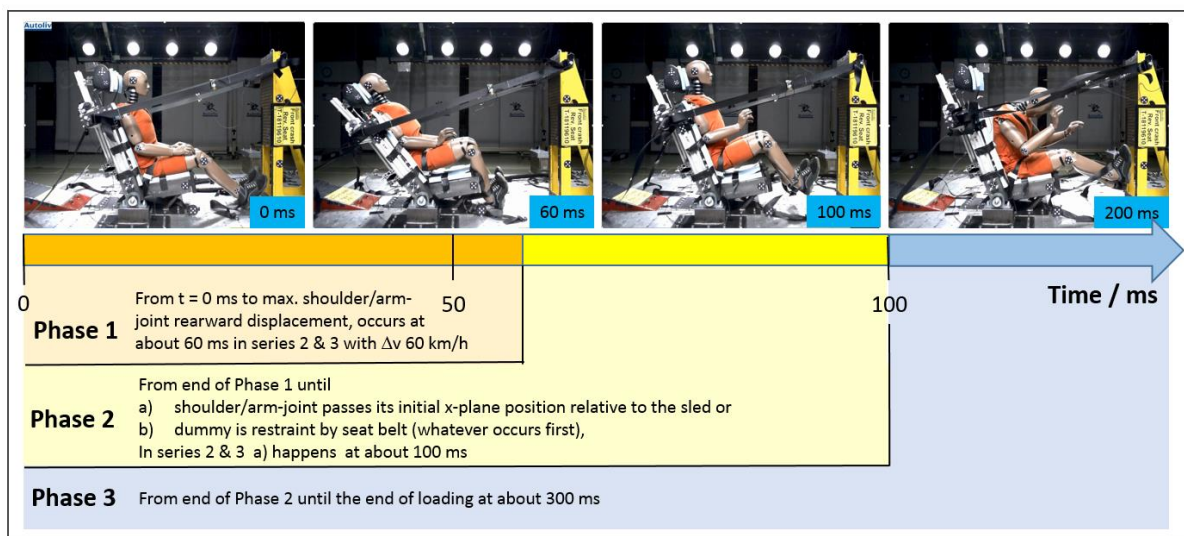


Figure 3. The three phases of the crash

In the further discussion we will focus on injury values for Phases 1 & 2 and will mention values of Phase 3 only when appropriate. Table 3 lists the tests with  $\Delta v$  60 km/h of test series 2. It is seen that chest acceleration was close to its legal limit in all three tests, lumbar spine compression came up to of 80% of its IARV of 6.4 kN. All other values were uncritical. The influence of the belt system to the injury assessment values was small. The maximum of chest deflection was reached in Phase 3. It was dependent on the seat belt and ranged from 5 mm for the lap belt and 19 mm for the crisscross belt.

Table 3.  
Test series 2, injury assessment values

0 < t ≤ 100 ms			Test-No.								
			Test 2.6 Lap Belt only			Seat integrated CrissCross Belt			Test 2.8 Seat integrated 3-point belt		
Region	Criterion	IARV	Value	% IARV	time / ms	Value	% IARV	time / ms	Value	% IARV	time / ms
Chest	3 ms clip [g]	60	62	103	42 - 45	58	97	43 - 46	60	100	42 - 45
	Deflection [mm]	42	6	15	37	12	28	64	7	16	39
	V*C [m/s]	1	0,06	6	37	0,08	8	61	0,07	7	41
Lumbar spine	Tension $F_{L,ZT}$ [kN]	12,2	2,6	21	82	1,1	9	95	1,7	14	83
	Compression $ F_{L,Zc} $ [kN]	6,4	4,8	76	26	5,1	79	26	5,3	83	27

The main focus of test series 3 was to investigate repeatability and to provide reliable data for the validation of a FE model. The setups of series 3 are listed in Table 4. A total of eight tests were performed with three different belt systems. As in test series 2, the differences between the belt systems in crash Phases 1 & 2 were not very pronounced and should not be discussed here further.

**Table 4.**  
*Test series 3, test setups*

Test	$\Delta V$	OLC	Belt System
3.1	60 km/h	32.0 g	Seat integrated 3-point belt with pretensioner fired at 0 ms
3.2	60 km/h	31.5 g	Seat integrated 3-point belt with pretensioner fired at 0 ms
3.3	60 km/h	31.4 g	no belt system
3.4	60 km/h	31.8 g	no belt system
3.5	60 km/h	31.6 g	Seat integrated 3-point belt
3.6	60 km/h	32.2 g	Seat integrated 3-point belt
3.7	60 km/h	31.6 g	Seat integrated 3-point belt
3.8	60 km/h	31.2 g	Seat integrated 3-point belt

The tests with the seat integrated 3 point belt were performed four times under the same condition. The time histories of chest acceleration and lumbar spine forces showed a good repeatability, cf. Figure 4. Deviations in lumbar spine forces were slightly bigger (especially close to the peaks at about 30 ms and 60 ms) and indicated a slight “complex” behavior, which is probably due to the friction between dummy and seat back. To further illustrate repeatability, in Figure 5 all IAV are listed. As long as the IAV were above 40% of its respective IARV, the relative standard deviations were below 5% except for the lumbar spine compression.

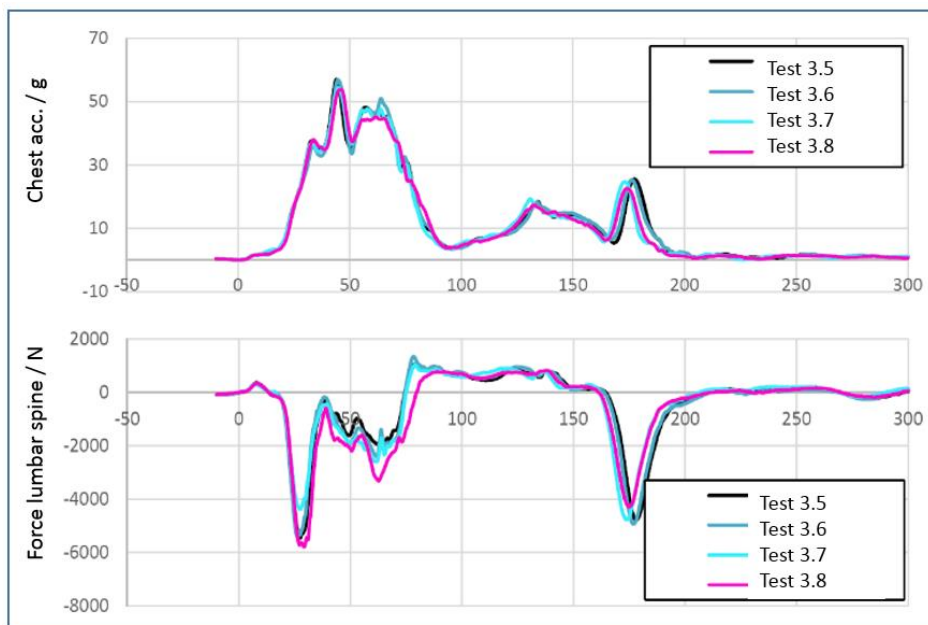


**Figure 4.** Time histories of chest acceleration and lumbar spine forces, 4 repeatability tests from series 3

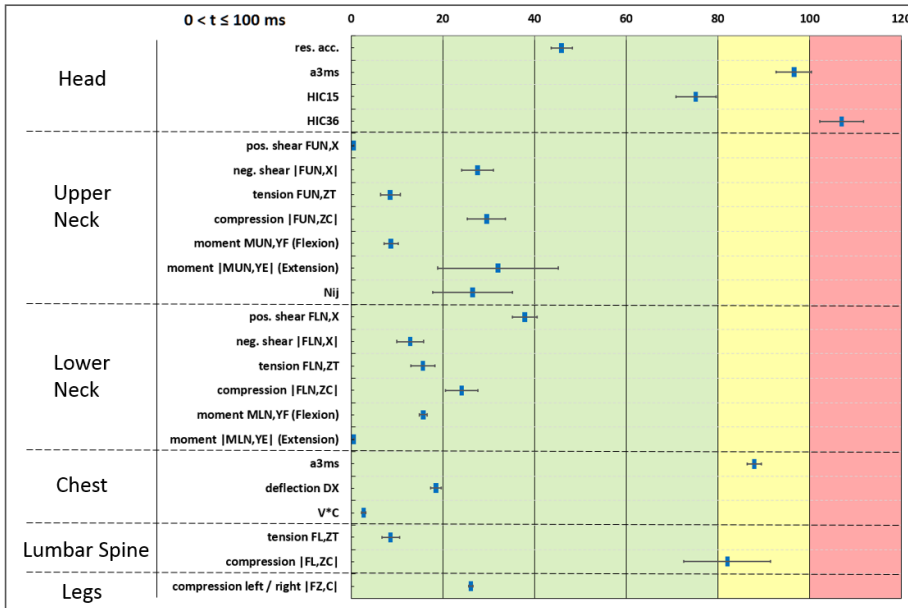


Figure 5. Test series 3, IAV in Phases 1 & 2, mean  $\pm$  one standard deviation in % of IARV, four repeatability tests, the respective reference values are listed in the Appendix

## DISCUSSION

One of our initial requirements to the generic test setup was, that the rearward displacement of the back rest was limited to avoid possible head contact of the occupant to the windscreen. This resulted in a relatively upright torso angle of the dummy during impact, even more upright than in the serial seat at  $\Delta v$  of 40 km/h, cf. Figure 6. Loading the occupant in this upright posture with such a stiff crash pulse requires further research and the dummy values can only be a rough indicator for possible injuries.

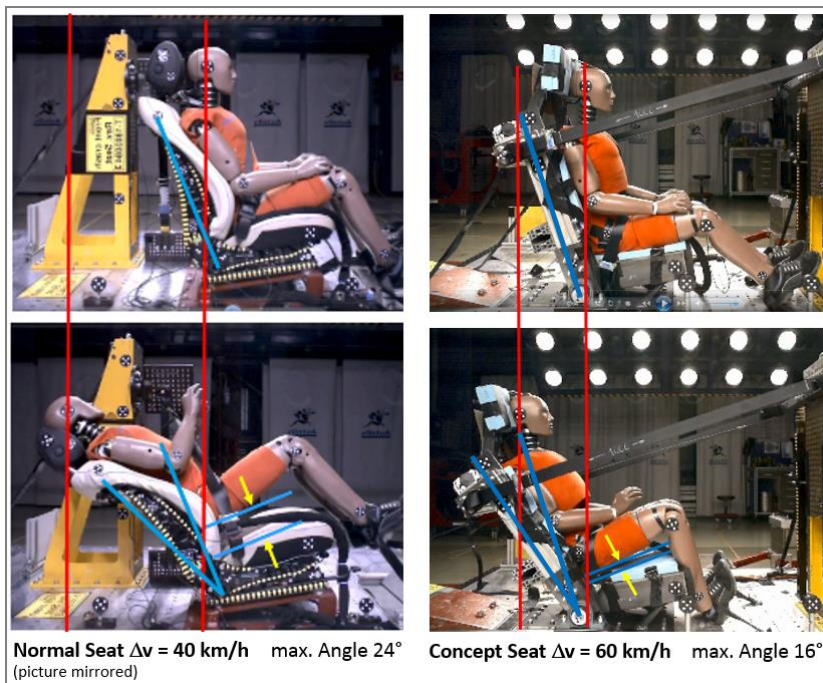
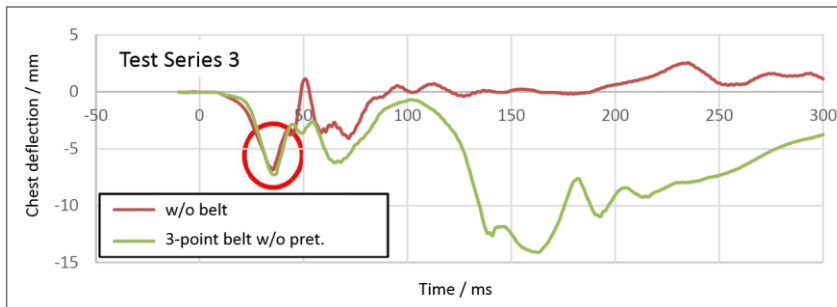
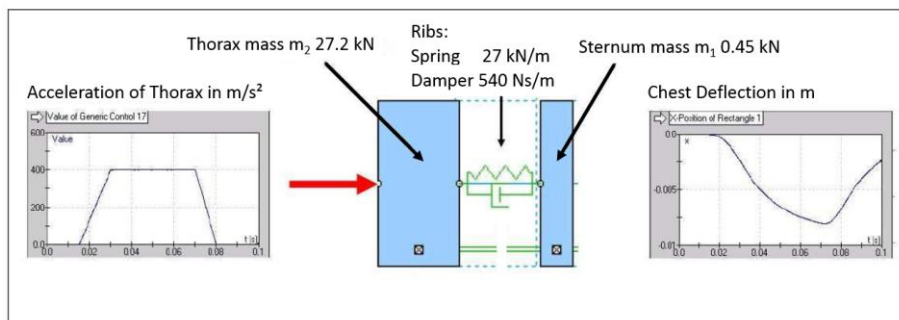


Figure 6. Comparison of the serial seat (left) and the generic (right) seat at maximum dummy rearward displacement

With the slightly stiffer crash pulse of test series 2, injury assessment values for chest acceleration and lumbar spine compression were close to its limits. With the slightly softer pulse of series 3, they reached about 80% to 90% of the limits, cf. Figure 5. It is also shown that injury values for the head were close to its respective reference values, but it again has to be mentioned that the dummy head is not validated for this impact direction. As we used an idealistic head rest without any initial gap between head and head rest, optimising the head rest for the rearward facing occupant may become a challenge. As shown in Figure 5, IAV for all other body regions were well below 40% of its limits. This is a good indicator that the generic test environment is suitable for testing, as test values are not masked by hard impacts of dummy parts to the seat. Chest deflection reached its maximum in Phase 3 and was dependent on the belt system. Values went up to 19 mm and were in good distance to its IARV. It is interesting to mention, that chest deflection in Phase 1 and 2 (0 ms to 100 ms) was mainly due to the inertia of the dummy ribcage, cf. Figure 6. The deflection went up to 7 mm and is the same for the tests with or without seat belt. A simple spring damper simulation with parameters for the thorax and ribcage from literature [15] yielded similar results.



**Figure 6. Test series 3, chest deflection with and without seat belt**



**Figure 7. Spring damper model of dummy chest, parameters taken from [15]**

As a next step in our investigation it is planned to build up and validate a finite element model of the generic test environment. In addition to the Hybrid III, response of a THOR 50<sup>th</sup> percentile male dummy and the THUMS human model should be investigated. Following steps using the FE models would include the study of the influence of back rest force to deflection characteristics both in impact as well in rebound. This should be optimised for dummy kinematics and loading. As described before, the influence of the seat belt system in Phases 1 & 2 is small. This is mainly due to a considerable amount of belt slack which is generated in the lap belt portion by initial dummy movement towards the seat back. A seat belt pretensioner at the anchor plate and buckle could eliminate this slack and the lap belt could properly restrain the dummy pelvis and prevent the whole dummy torso to move upwards during impact. This may also help to reduce lumbar spine compression. In the following step, the seat belt system restraint performance in Phase 3 may be optimised.

It has to be pointed out here that there is a need of reliable IARV for this loading direction and a common agreement on which dummy or human model to be used to evaluate the occupant protection.

As limitation of our study it should be mentioned that only full frontal loading directions were studied, dummy kinematics of oblique impact direction, simulating e.g.  $\pm 30^\circ$  angled impacts to the barrier, were not included. As the head rest was not in focus of our investigation, the head was fixed with tape to the head rest without any gap in between.



## CONCLUSION

A generic sled test and simulation environment for vehicle frontal impacts at a  $\Delta v$  of up to 60 km/h with occupants on rearward facing seats was developed and evaluated. The repeatability was investigated in four repeated tests, the relative standard deviations showed to be mostly below 5% of the respective injury assessment value and can be considered as good. The injury assessment value closest to its reference value showed to be chest acceleration, second was lumbar spine compression with about 80% of its limit. Peak chest deflection occurred in rebound and was below 20 mm.

## REFERENCES

- [1] SAE Standard J3016. 2016. "Taxonomy and Definitions for Terms Related to On-Road Motor Vehicle Automated Driving Systems;" SAE, 30.09.2016
- [2] Sofia Jorlöv, Katarina Bohman, Annika Larsson. 2017. "Seating Positions and Activities in Highly Automated Cars – A Qualitative Study of Future Automated Driving Scenarios;" Proceedings IRCOBI Conference, Antwerp, Belgium
- [3] Harald Zellmer, Nils Lubbe, Ulrich Sander. 2018. "Assessing the Injury Risk of Car Occupants on Rearward Facing Seats – An Analysis of GIDAS Cases;" 8th ESAR Conf. Hannover, Germany
- [4] James W. Saunders III, Louis N. Molino, Shashi Kuppa, Felicia L. McKoy. 2003. "Performance of Seating Systems in a FMVSS No. 301 Rear Impact Crash Test"; Proceedings 18<sup>th</sup> ESV-Conference, Nagoya, Japan
- [5] David C. Viano, Chantal S. Parenteau, Roger Burnett, Priya Prasad. 2017. "Occupant Responses in Conventional and ABTS Seats in High-Speed Rear Sled Tests;" Traffic Injury Prevention.
- [6] Yuichi Kitagawa, Shigeki Hayashi, Katsunori Yamada, Mitsuaki Gotoh. 2017. "Occupant Kinematics in Simulated Autonomous Driving Vehicle Collisions: Influence of Seating Position, Direction and Angle;" Stapp Car Crash Journal, Vol. 61
- [7] Xin Jin, Haibin Hou, Ming Shen, Hequan Wu, King H. Yang. 2018. "Occupant Kinematics and Biomechanics with Rotatable Seat in Autonomous Vehicle Collision: A Preliminary Concept and Strategy"; Proceedings IRCOBI Conference, Athens, Greece
- [8] National Highway Traffic Safety Administration. Federal Motor Vehicle Safety Standard No. 208. "Occupant Crash Protection"; 49 CFR 571.208, 2013
- [9] ECE-Regulation No. 137-01: "Uniform Provisions Concerning the Approval of Passenger Cars in the Event of a Frontal Collision with Focus on the Restraint System;" Amendment Level 01 Supplement 1, Feb. 2017
- [10] European Aviation Safety Agency (EASA): "Certification Specification and Acceptable Means of Compliance for Large Rotorcraft"; Certification Specification 29, Amendment 4, 2016
- [11] General Motors (GM): "Occupant Performance Evaluation Consideration Book (Blue book);" Document #SRC-1000G, USA. Version 3, Revision 0, May 1998
- [12] National Highway Traffic Safety Administration, Federal Motor Vehicle Safety Standard No. 202a: "Head Restraints"; 49 CFR 571.202a, 2009
- [13] L. Kübler, S. Gargallo, K. Elsäßer. 2009. "Frontal crash pulse assessment with application to occupant safety;" ATZ worldwide Volume 111, Issue 6
- [14] Markus H. Muser, Felix H. Walz, Harald Zellmer. 2000 "Biomechanical Significance of the Rebound Phase in Low Speed Rear End Impacts;" Proc. IRCOBI Conf., Montpellier, France
- [15] Jeff Crandall, Zhiqing Cheng, W. D. Pilkey. 2000. "Limiting performance of seat belt systems for the prevention of thoracic injuries;" Proceedings of the Institution of Mechanical Engineers Part D, Journal of Automobile Engineering 214(2):127-139
- [16] Harold J. Mertz, Annette L. Irwin, Priya Prasad. 2016. "Biomechanical and scaling basis for frontal and side impact injury assessment reference values;" Stapp Car Crash Journal, Vol. 60



APPENDIX

*Injury assessment reference values (IARV) used for the rating of repeatability*

	Injury Criterion	IARV	Source
Head	res. acc.	180 g	Mertz 2016 [16]
	a3ms	80 g	ECE-R 137 [9]
	HIC15	700	FMVSS 208 [8]
	HIC36	1000	ECE-R 137 [9]
Upper Neck	pos. shear FUN,X	3.1 kN	ECE-R 137 [9]
	neg. shear  FUN,X	3.1 kN	ECE-R 137 [9]
	tension FUN,ZT	4.17 kN	ECE-R 137 [9]
	compression  FUN,ZC	4.0 kN	FMVSS 208 [8]
	moment MUN,YF (Flexion)	190 Nm	Mertz 2016 [16]
	moment  MUN,YE  (Extension)	57 Nm	ECE-R 137 [9]
	Nij	1	FMVSS 208 [8]
Lower Neck	pos. shear FLN,X	3.1 kN	Mertz 2016 [16]
	neg. shear  FLN,X	3.1 kN	Mertz 2016 [16]
	tension FLN,ZT	4.17 kN	Mertz 2016 [16]
	compression  FLN,ZC	4.0 kN	Mertz 2016 [16]
	moment MLN,YF (Flexion)	380 Nm	Mertz 2016 [16]
	moment  MLN,YE  (Extension)	194 Nm	Mertz 2016 [16]
Chest	a3ms	60 g	FMVSS 208 [8]
	deflection DX	42 mm	ECE-R 137 [9]
	V*C	1 m/s	ECE-R 137 [9]
Lumbar Spine	tension FL,ZT	12.2 kN	GM Blue Book 1998 [11]
	compression  FL,ZC	6.4 kN	GM Blue Book 1998 [11]
Legs	compression left / right  FZ,C	9.07 kN	ECE-R 137 [9]

# **Evaluation of the Safety Performance and Weight Reduction Using CFRP Modified Automotive Structures in NHTSA's Frontal Oblique Impact Test**

**William Hollowell, Ph.D.**  
WTH Consulting LLC

**Rudolf Reichert**  
**Steve Kan, Ph.D.**  
**Chung-Kyu Park, Ph.D.**  
George Mason University

United States

**Paper Number** 19-0169

## **ABSTRACT**

In a project conducted for NHTSA during 2016-2017, finite element analysis simulations were conducted representing NHTSA's right and left oblique impact configurations being developed for possible use in the agency's New Car Assessment Program. For the study using this test procedure, simulations were conducted representing an offset moving deformable barrier impacting a stationary 2015 Toyota Camry with a 35 percent overlap and an angle of 15 degrees (from collinear) at a speed of 90 km/h. In the NHTSA project, the model was successfully used to develop structural countermeasures in order to reduce occupant compartment intrusion for the new oblique impact configuration. Higher strength steel materials and modification of component thicknesses allowed the reduction of occupant compartment intrusion by more than 50%. As part of this effort, George Mason University (GMU) calculated mass and relative material expense comparisons to traditional materials. As a result, three optimized models using traditional materials were created. The accomplished reduction of occupant compartment intrusion ranged from 52% to 69% and the associated added mass ranged from 7.3 kg to 17.3 kg. The significant reduction in intrusion was achieved without unintended consequences, i.e., no considerable increases in the vehicle pulse severity for oblique and co-linear crash configurations were observed.

Following these results, the American Chemistry Council (ACC) commissioned this subsequent study to determine if the vehicle could be lightweighted and provide a similar reduction of occupant compartment intrusion for NHTSA's right and left oblique impact configurations using carbon fiber reinforced plastic (CFRP) composite materials. Different thicknesses for relevant components were evaluated and associated reductions in intrusion, associated changes in mass, and associated critical areas with material failure were determined. As a result of using selected components made out of a composite material, a similar reduction in occupant compartment intrusion was achieved in NHTSA's right and left oblique impact configuration as realized for the best high strength steel model. In using the CFRP composite material, the associated change in mass was a reduction of 7 kg of the baseline vehicle as compared to an increase of 17 kg in the baseline vehicle mass when using more traditional countermeasures-- higher component thicknesses and use of high strength steel materials.

The developed and incorporated countermeasures using composite materials were also evaluated to determine if they produced unintended consequences in other impact configurations. The developed FE models, which showed reduced occupant compartment intrusion due to components made out of the CFRP composite material in NHTSA's oblique crash configuration, were also evaluated in NHTSA's NCAP full overlap and in the Insurance Institute for Highway Safety (IIHS) partial overlap crash configurations. No unintended consequences were observed when the results were analyzed with respect to vehicle pulse and intrusion when compared to the results using the baseline simulation model.

In addition to the above technical achievements, in partnership with Honda R&D Americas and LSTC; other efforts are underway. These include the development of a material constitutive model of the composite material for use in modeling and subsequent simulation in automotive crash applications. Also, validation efforts using CFRP components will be undertaken.

## INTRODUCTION

In fiscal year 2006, Congress directed the National Highway Traffic Safety Administration (NHTSA) of the U.S. Department of Transportation (DOT) to begin the development of a program to examine the possible safety benefits of lightweight Plastics- and Composite-Intensive Vehicles (PCIVs). NHTSA tasked the Volpe National Transportation Systems Center to conduct focused research in cooperation with industry partners from the American Plastics Council (APC), now the American Chemistry Council Plastics Division (ACC-PD).

NHTSA concentrated on the safety-related research issues affecting the deployment of PCIVs in 2020. In 2007, the Volpe Center developed a safety roadmap for future PCIVs and described the approach, activities, and results of an evaluation of potential safety benefits of PCIVs [1,2]. Barnes et al. identified outstanding safety issues and research needs for PCIVs to facilitate their safety deployment by 2020, and recommended three topics pertinent to crashworthiness of PCIVs: (1) material database, (2) crashworthiness test method development, and (3) crash modeling [3].

In 2001, the APC (now the ACC-PD) outlined a Vision and Technology Roadmap for the automotive and plastics industries [4]. In the technology integration workshop in 2005, the ACC-PD provided an expansive safety road mapping effort, examining PCIVs [5]. In 2009, the ACC-PD updated the vision and technology roadmap to outline the industry's action priorities for achieving the technology and manufacturing innovations required to realize PCIVs [6]. In addition, the ACC-PD recommended three research activities: (1) improvement of the understanding of composite component response in vehicle crashes, (2) development of a database of relevant parameters for composite materials, and (3) enhancement of predictive models to avoid costly overdesign [7].

There is an increasing need to investigate opportunities for weight reduction of the vehicle fleet to improve fuel economy and compatibility. However, this should be achieved without sacrificing the current self-protection. Innovative plastics and fiber-reinforced composite materials offer a means to lightweight vehicle structures. The main advantages of composites over the more conventional isotropic materials are the lower density, very high specific strength, and specific stiffness that can be achieved.

In 2014, the ACC-PD updated the Plastics and Polymer Composites Technology Roadmap for Automotive Markets [8] in response to the U.S. Corporate Average Fuel Economy (CAFE) standards in order to develop an effective industry-wide strategy that will extend to 2030 and beyond. The roadmap addresses current barriers and key initiatives to recognize plastics and polymer composites as preferred material solutions that meet automotive performance and sustainability requirements.

As part of implementing the ACC roadmap, the ACC partnered with the George Mason University's Center for Collision and Safety Analysis (GMU/CCSA) to conduct research to evaluate the application of plastics and composites using Computer-Aided Engineering (CAE) simulations. In a previous study, the GMU Team developed a lightweight vehicle by replacing existing steel components with plastics or composite components in a reverse-engineered computer model. To support realistic development, industry partners participated in the project by providing available plastics/composite materials and their application and design. The crashworthiness of the lightweighted components was investigated through impact simulations, both at a component level and at a full vehicle level. The results were documented in Reference [9].

A more specific research task was adopted in this current project. Using computer simulation, an evaluation was conducted to determine if countermeasures using CFRP modified automotive structures in NHTSA's newly developed frontal oblique impact test procedure could achieve a similar reduction in occupant compartment intrusion as countermeasures using high-strength steel materials.

Consumer information crash tests, such as NHTSA's New Car Assessment Program's (NCAP's) full overlap frontal impact and the Insurance Institute for Highway Safety's (IIHS's) small and moderate overlap frontal impacts, have contributed to advance vehicle safety and reduce injury risk in the past. Recent studies have indicated that oblique crashes represent common real-world accident patterns related to belted occupant fatalities [10]. When comparing the number of injuries by body region for oblique and co-linear frontal impacts, it was observed that drivers in left oblique impacts experienced more Maximum Abbreviated Injury Scale (MAIS) 3+ injuries in almost every body region than drivers in co-linear crashes [11].

The Center for Collision Safety and Analysis (CCSA) at George Mason University (GMU) has analyzed sixteen left oblique tests conducted by NHTSA regarding intrusion patterns and related injury risk [12]. Furthermore, 65 oblique and 265 NCAP full overlap tests were analyzed regarding vehicle pulse, intrusion, and injury metrics. While there was no clear trend linking higher intrusion to higher tibia loads, it was found that occupant compartment intrusion, pulse severity, and local effects could contribute to lower extremity injuries. It can be concluded that risk of injury can increase as the maximum intrusion from the occupant compartment increases.

IIHS compared the performance of 25 vehicles in NHTSA's frontal oblique condition and the IIHS small overlap configuration. The selected cars represented a wide range of vehicle sizes. With respect to lower extremity injuries, it was found that 36% (9 cars) of the vehicles exceeded preliminary Injury Assessment Reference Values (IARVs) in the oblique impact, while only 8% (2 cars) exceeded the IARVs for the small overlap configuration [13]. Differences in vehicle pulse and occupant compartment intrusion are considered possible reasons.

The oblique impact test captures the deformations of a significant number of real-world accidents that occur today, and the development of additional countermeasures for restraints and vehicle structure may have the potential to further improve vehicle safety and reduce injury risk in the future. Consequently, NHTSA is considering adopting a frontal oblique impact configuration into its NCAP rating protocol [11].

The developed laboratory test procedure is conducted in combination with a more biofidelic dummy, the Test device for Human Occupant Restraints (THOR) [11]. An Oblique Moving Deformable Barrier (OMDB) was developed to produce target vehicle crush patterns similar to real-world cases [14]. It has a weight of 2,500 kilograms (kg) and impacts a stationary vehicle at a speed of 90 kilometers per hour (km/h). The vehicle is placed at a 15-degree angle and a 35-percent overlap occurs between the OMDB and the front end of the struck vehicle, as shown in Figure 1.

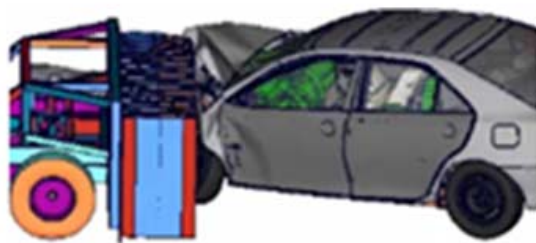


**Figure 1 - Frontal Oblique Test Configuration**

Crash test results have shown that vehicles may require structural modifications for good performance in NHTSA's frontal oblique test procedure. In a previous project that was funded by NHTSA, the GMU team determined incremental vehicle structural change requirements using steel materials and their associated mass to significantly reduce occupant compartment intrusion.

An available FE model of a 2012 Toyota Camry mid-size sedan was updated and validated using data to represent a 2015 Toyota Camry. The newly generated baseline model correlated well with the New Car Assessment Program (NCAP) full overlap test, NHTSA's left and right oblique impact tests, and with the IIHS small and moderate overlap crash configurations. An iterative process was used to develop countermeasures to significantly reduce occupant compartment intrusion for the left and right oblique impact configuration. No un-intended consequences (i.e., no considerable increase in the vehicle pulses for the oblique and co-linear crash configurations) were observed. The associated added mass was +17 kg using high-strength steel materials [15].

The aforementioned developed FE model and tools were used to determine if similar results (i.e., a similar reduction in occupant compartment intrusion, and no un-intended consequences, such as significantly more severe vehicle crash pulses) could be achieved using composite materials for select components.

## OBJECTIVE

The objective of this research was to develop changes using CFRP composite materials to modify a passenger vehicle's structure to provide equivalent performance as the vehicle modified with high strength steel modifications in order to reduce occupant compartment intrusion in NHTSA's oblique frontal crash test condition. Structural countermeasures for both the driver's and passenger's sides of the vehicle for left- and right-side oblique impacts were to be developed.

## VEHICLE SELECTION

The vehicle selected for this study was the baseline selected for the NHTSA study using the high strength steels for improving the crash performance in the frontal oblique offset test. Several criteria were used to determine an appropriate vehicle on which to conduct that research. This included evaluation of the number of vehicle sales as a measure of how well it represents mid-size sedans in the United States (US), performance in existing consumer information tests, and availability of an adequate FE simulation baseline model. The vehicle also was required to meet the structural intrusion requirements for a "GOOD" or "ACCEPTABLE" structural rating in the IIHS small overlap crash test, "GOOD" rating in the IIHS moderate overlap crash test, and a 5-Star rating in the NCAP full frontal crash test.

Satisfying the aforementioned criteria, a FE model of a 2012 Toyota Camry, which had been developed by the GMU Team, was used as a starting point. Toyota introduced structural design changes in January 2014. The MY 2012 mid-size sedan FE model was updated accordingly. Figure 2a illustrates the relevant structural differences between MY 2012 and MY 2015. Figure 2b shows (from right to left) a bottom view of the finite element model with an enlarged view of the added bumper reinforcement extension and "spacer" for the simulation model and the physical vehicle.

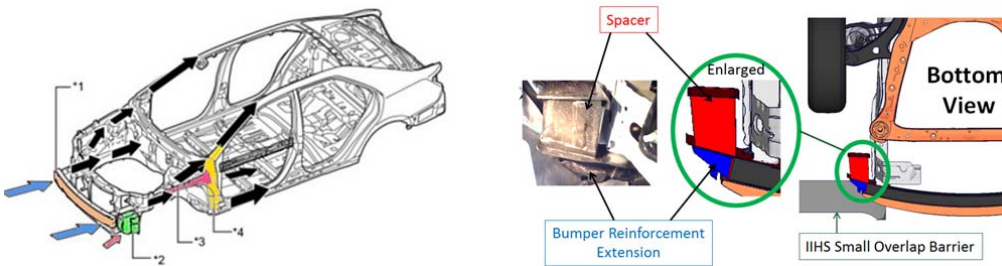


**Figure 2 – Design Changes (a) Schematic, (b) “Spacer”**

Advanced modeling techniques for the wheel connection were implemented into the FE model to better represent the failure mechanisms and wheel kinematics seen in the IIHS small overlap impact. The added bumper reinforcement extension and spacer interacts with the IIHS small overlap barrier and activates the frontal rail on the driver side. The deformation of the longitudinal rail contributes to the structural crash energy absorption. Full-scale test results showed that the design changes mainly affected performance in the IIHS small overlap impact, while other crash configurations, such as NCAP full overlap and NHTSA left oblique impact, showed similar results for the MY 2012 and MY 2015 vehicles.

All updates were implemented to the driver and passenger side of the FE model. The associated added vehicle mass was equivalent to 9.7 kg and is like the difference in vehicle mass from NHTSA's left oblique test of a MY 2015 vehicle (test #8790, 1450 kg as delivered, 1734 kg as tested) and a MY 2012 vehicle (test #9124, 1443 kg as delivered, 1759 kg as tested).

Test data from the MY 2015 vehicle was used to evaluate the updated FE model. Full-scale crash tests with vehicles that included these changes are called "2015 Toyota Camry" tests in the remainder of this paper. Even though complete information for all the detailed design changes from MY 2012 to MY 2015 was not available, it was determined that the updated FE model does a good job of simulating the performance of the MY 2015 mid-size sedan in the respective crash configurations.

Shown in Figures 3 and 4 are the vehicle’s longitudinal (X-axis) acceleration time histories for the left oblique and right oblique simulations versus the test results. Also shown in each figure is the CORA rating value. The CORA values of 0.94 and 0.93 respectively represent a good correlation between the test and simulation results.

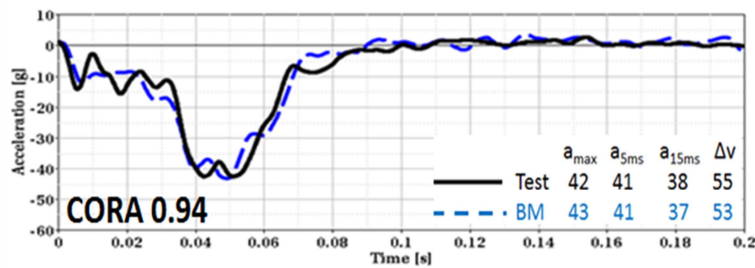


Figure 3 - 2015 Left Oblique Test vs Sim. - Vehicle Pulse

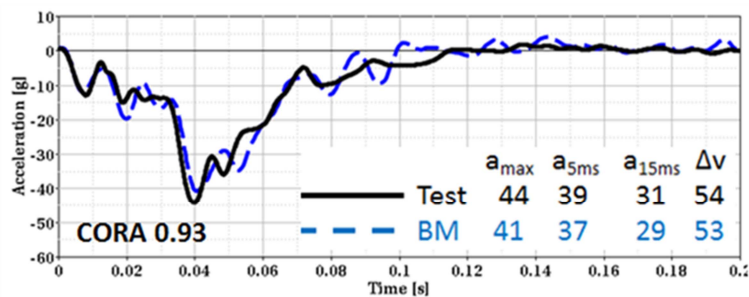


Figure 4 - Right Oblique Test vs Sim. - Vehicle Pulse

All baseline simulations were conducted using this model. It will be called the “2015 Toyota Camry Baseline Model (TCBM)” in the remainder of this paper. For this study looking at CFRP composite structural modifications, the developed structural countermeasures to significantly reduce occupant compartment intrusion were evaluated with respect to the TCBM and to the TCBM with the high strength steel modifications.

### CFRP COMPOSITE MATERIAL SELECTED FOR STUDY

In a previous study [16], a braided carbon-fiber thermoset composite material was selected as the steel substitute in the vehicle structures. Many material tests and numerical simulations were conducted to identify its material characteristics for a Carbon Fiber Reinforced Plastic (CFRP). Their results are described in the project report [16]. A brief summary of these is described in this section. The developed and validated material card was used for select components when developing structural countermeasures to reduce occupant compartment intrusion in NHTSA’s oblique impact configuration.

Tri-axial braided composites can offer an isotropic design by using axial and angled fiber bundles in a single plan. Braided composites also offer better damage resistance, torsional stability, and bending strength compared to unidirectional or weaved composites. Tri-axial braided composites have been used in the commercial aerospace and automotive industry for over 20 years. They are well suited for components that are of simple geometry and need to provide off-axis as well as unidirectional strength. In addition, various studies using braided composites have been conducted and published.

The selected braided CFRP composite used for the material tests is described as follows. The carbon fiber was Torayca T700S C 12000, manufactured by Toray Carbon Fibers America, Inc. The braid architecture is  $0^\circ/\pm 60^\circ$  2D triaxial (2D3A), as shown in Figure 5. The axial fiber tows contained 24K fibers. The bias tows contained 12K fibers. The resin was Epon 862 epoxy with an Epikure W curing agent, both manufactured by Momentive.



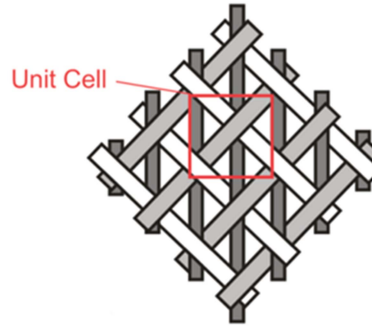
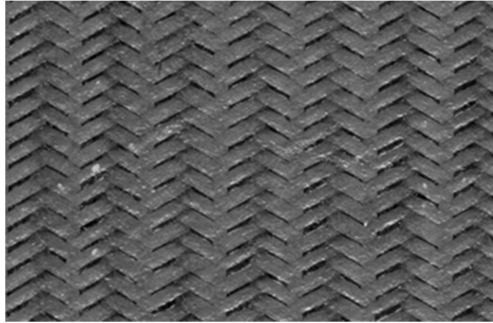


**Figure 5 - 2D3A braided composite: (a) panel, (b) unit cell.**

Tension, compression and shear coupon tests were performed in two different directions (axial and transverse) and at four different loading rates. The tension test used two different types of specimens; a standard specimen and a bowtie specimen. A total of 72 coupon tests were conducted. Tube compression tests were performed with three different loading rates. Reference 16 provides a summary of the test data and the material properties used for LSDYNA’s MAT58 material cards.

### **STRUCTURAL COUNTERMEASURES**

Three sets of countermeasures using high-strength steel materials were developed to meet the defined design goals in the previous project, funded by NHTSA. The countermeasure model (“CM-Steel”) that showed the highest amount of occupant compartment intrusion reduction is discussed in this paper. It serves as reference for the countermeasure model using composite material (“CM-Composite”). Occupant compartment intrusion was reduced by more than 60% compared to the baseline model (BM). Figure 6 presents an overview of the implemented modifications for CM-Steel.

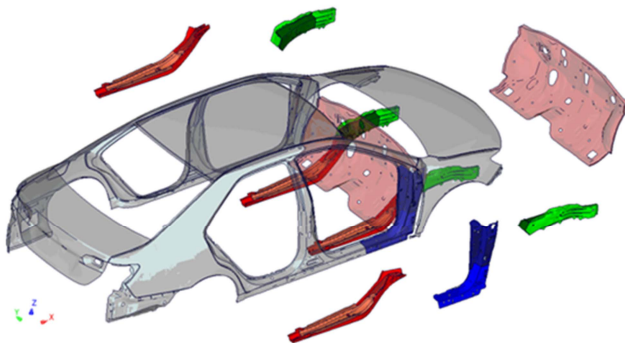


**Figure 6 – CM Steel - Structural Countermeasures**

The firewall, three components of the right hinge pillar, two parts of the left and right frontal rails, and three parts of the left and right mid-rails were modified.

In order to reduce maximum toe-pan intrusion and local buckling, the material thickness and material strength were increased for the firewall, shown in pink. Material thickness was also increased for three components of the right hinge pillar, shown in blue. For the inner hinge pillar (a) and the middle hinge pillar (b) material strength was also increased. The material strength for the outer hinge pillar (c) was not changed in order to allow the same manufacturing stamping process used for the BM. Changes to the right hinge pillar contributed to reduced intrusion and reduced local buckling, specifically in the right oblique impact. The parking brake on the driver side acts as a reinforcement of the hinge pillar area on the driver side. Therefore, the left hinge pillar components were not changed.

In order to reduce the load induced into the firewall, material thickness for two parts of the left and right frontal rails, shown in green, were marginally reduced. This contributed to reduction in maximum toe-pan intrusion and local buckling.

For this study, the use of CFRP composite material for the development of structural countermeasures to significantly reduce occupant compartment intrusion in NHTSA's oblique impact condition required having a thorough understanding of the crash mechanisms. The baseline vehicle model crash simulations were analyzed with respect to crash mechanisms that specifically contribute to the observed intrusion in left and right oblique impacts.

Local buckling of the firewall was found to be a major factor. Highest intrusion values were observed for toe-pan measurement points in row 1, which represent the most forward and upward locations. It was found that the load transferred through the longitudinal rail contributed to the maximum intrusion values. It can be noted that the load introduced through the frontal rails is being leveraged through the difference in height between the frontal rail and the bottom of the mid-rails. The load introduced through the frontal rail contributes to the maximum intrusion values and local buckling of the toe-pan.

Local buckling of the mid-rails also contributed to the observed occupant compartment intrusion. It was found that there was a significant amount of deformation occurring in the right mid-rail. The parking brake on the driver side is connected to the rocker pillar and the toe-pan area. It acts as a reinforcement of the rocker pillar area on the driver side. Since there is no equivalent component on the passenger side, a significant amount of deformation of the right rocker pillar components was observed in the right oblique impact configuration. Deformation of the rocker pillar components on the passenger side contributed to the maximum occupant compartment intrusion in the right oblique impact.

A firewall support component around the steering column exists on the driver side. The absence of an equivalent firewall support component on the passenger side contributed to the maximum occupant compartment intrusion in the right oblique impact.

As a result of the above analysis, an evaluation was undertaken to determine if a similar reduction of occupant compartment intrusion could be achieved by using the CFRP composite for the firewall component. Three different thicknesses, i.e., 1.2 mm (2 layers), 2.4 mm (4 layers), and 3.6 mm (6 layers) were evaluated. The associated change in vehicle mass for the CM-Composite vehicles compared to the TCBM was -15 kg, -11 kg, and -7 kg, respectively.

## **RESULTS**

### **Left Oblique Impact**

CM-Steel simulation results were compared against the respective BM simulation in NHTSA's left oblique impact configuration. The maximum toe-pan intrusion was reduced by more than 60%. Figure 7 shows a cross-section view of the left passenger compartment. The black line represents the un-deformed "pre-crash" vehicle. The red line represents the deformed shape of the baseline model with high occupant compartment intrusion. The green line shows the deformed shape of the CM-Steel vehicle with a significant reduction of intrusion compared to the BM. The associated change in mass when using countermeasures made out of steel, was +17 kg compared to the BM.

The dark red line represents the CM-Composite 1 vehicle, where a composite material made out of two layers was used for the firewall. Intrusion was as high as for the BM and the associated change in mass was -15 kg. The yellow line shows the CM-Composite 2 vehicle with 4 layers of composite and an associated change in mass of -11 kg. Intrusion was reduced compared to the BM but was still significantly higher than for the CM-Steel vehicle. The blue line represents the CM-Composite 3 vehicle with 6 layers of composite. The respective thickness was 3.6 mm and the associated reduction in mass compared to the BM was -7 kg. Similar reduction of occupant compartment intrusion was achieved with the CM-Composite 3 model compared to the CM-Steel vehicle. However, instead of adding 17 kg to the total vehicle mass when using steel countermeasures, a reduction of 7 kg was achieved when using composite countermeasures. The CM-Composite 3 vehicle will also be called "CM-Composite" in the remainder of this paper.

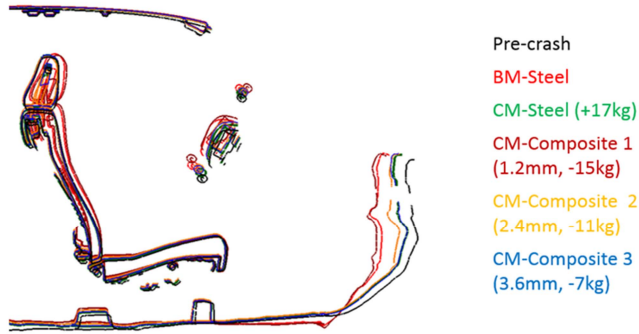


**Figure 7 – Left Oblique Intrusion- Baseline vs. CM-Steel and CM-Composite**

Figure 8 shows the vehicle pulse, measured at the rear of the vehicle and processed using a SAE 60 filter. An overall similar vehicle pulse was observed for the CM-Steel vehicle, shown in green, and the CM-Composite vehicle, shown in blue. The maximum peak of both vehicles was only marginally higher than measured for the BM, shown in red. No significant effect with respect to restraint system performance and occupant injury risk due to the introduced structural changes for CM-Steel and CM-Composite was therefore predicted.

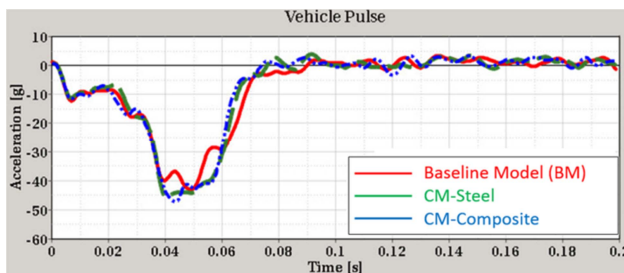


**Figure 8 – Left Oblique Vehicle Pulse - BM vs. CM-Steel and CM-Composite**

### Right Oblique Impact

CM-Steel simulation results were compared against the respective BM simulation in NHTSA’s right oblique impact configuration. The maximum toe-pan intrusion was reduced by more than 60%. Figure 9 shows a cross-section view of the left passenger compartment. The black line represents the un-deformed “pre-crash” vehicle. The red line represents the deformed shape of the baseline model with high occupant compartment intrusion. The green line shows the deformed shape of the CM-Steel vehicle with a significant reduction of intrusion compared to the BM. The associated change in mass when using countermeasures made out of steel, was +17 kg compared to the BM. The dark red line represents the CM-Composite 1 vehicle, where 2 layers of composite material were used for the firewall. Intrusion was as high as for the BM and the associated change in mass was -15 kg. The yellow line shows the CM-Composite 2 vehicle with 4 layers of composite and an associated change in mass of -11 kg. Intrusion was reduced compared to the BM but was still significantly higher than for the CM-Steel vehicle. The blue line represents the CM-Composite 3 vehicle with 3 layers of composite. The respective thickness was 3.6 mm and the associated reduction in mass compared to the BM was -7 kg. Similar reduction of occupant compartment intrusion was achieved with the CM-Composite 3 model compared to the CM-Steel vehicle. However, instead of adding 17 kg to the total vehicle mass when using steel countermeasures, a reduction of 7 kg was achieved when using composite countermeasures.



**Figure 9 – Right Oblique Intrusion- Baseline vs. CM-Steel and CM-Composite**

Figure 10 shows the vehicle pulse, measured at the rear of the vehicle and processed using a SAE 60 filter. An overall similar vehicle pulse was observed for the CM-Steel vehicle, shown in green, and the CM-Composite vehicle, shown in blue. The maximum peak of both vehicles was only marginally higher than measured for the BM, shown in red. No significant effect with respect to restraint system performance and occupant injury risk due to the introduced structural changes for CM-Steel and CM-Composite was therefore predicted.

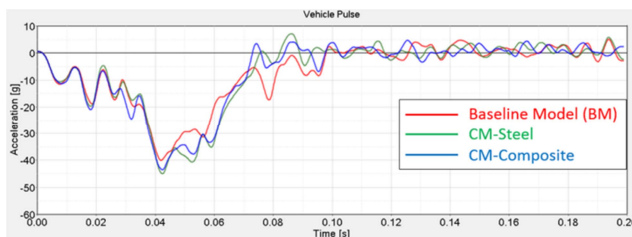


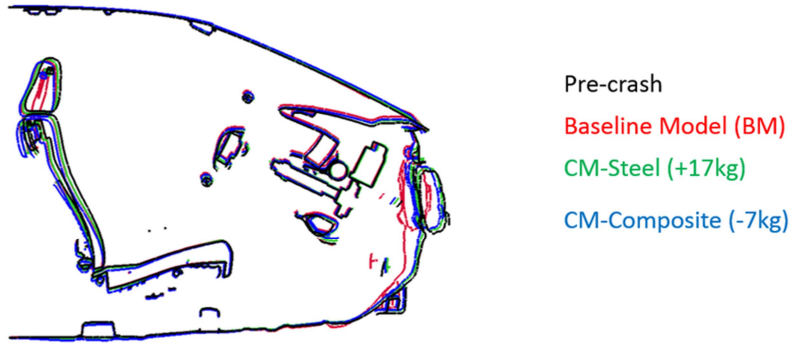
**Figure 10 – Right Oblique Vehicle Pulse - BM vs. CM-Steel and CM-Composite**

### **NHTSA NCAP Full Overlap**

In the NCAP full frontal configuration, the tested vehicle travels at a speed of 56 km/h with full overlap co-linear into a rigid wall. In the full-scale test, the vehicle is equipped with a 50th percentile male Hybrid III dummy in the driver seat and with a 5th percentile female Hybrid III dummy in the passenger seat. The current NCAP rating is based on injury risk assessment rather than occupant compartment intrusion.

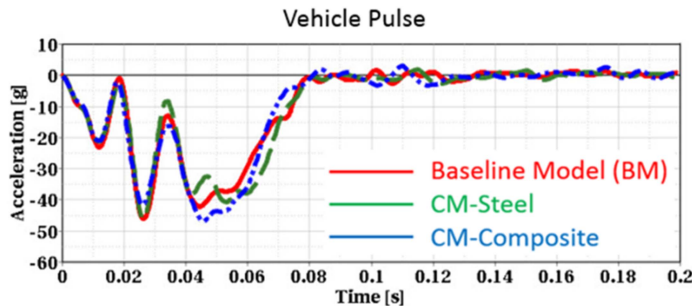
The effect of structural countermeasures developed for NHTSA’s oblique impact was evaluated for the NCAP full overlap load case. The CM-Steel vehicle with countermeasures using high-strength steel (+17 kg) and the CM-Composite vehicle with 6 layers (-7 kg) were evaluated with respect to the baseline model.

Figure 11 shows a cross-section view on the driver side. The geometrical shape of the vehicle “pre-crash” is shown in black. The deformed shape of the BM after the vehicle has impacted a rigid wall at 56 km/h is shown in red. The occupant compartment intrusion is smaller than for the oblique impact configurations. The vehicle with countermeasures out of high-strength steel (CM-Steel) is shown in green and the CM-Composite vehicle is depicted in blue. No significant occupant compartment intrusion was observed for either countermeasure models. CM-Steel and CM-Composite resulted in a reduction of occupant compartment intrusion compared to the BM in NHTSA’s NCAP full overlap load case.



**Figure 11 – NCAP Full Overlap – BM vs. CM-Steel and CM-Composite**

Figure 12 shows the vehicle pulse, measured at the rear of the vehicle and processed using a SAE 60 filter. An overall similar vehicle pulse was observed for the CM-Steel vehicle, shown in green, and the CM-Composite vehicle, shown in blue. The maximum peak of both vehicles was similar to the BM, shown in red. While the first peak, caused by initial contact of the rigid barrier with the engine, was the same for the BM and CM-Steel, the initial peak was marginally lower for the CM-Composite vehicle. The second peak at about 50ms showed the opposite trend. The CM-Composite vehicle showed a marginally higher peak compared to the BM and CM-Steel. No significant effect with respect to restraint system performance and occupant injury risk due to the introduced structural changes for CM-Steel and CM-Composite was therefore predicted.



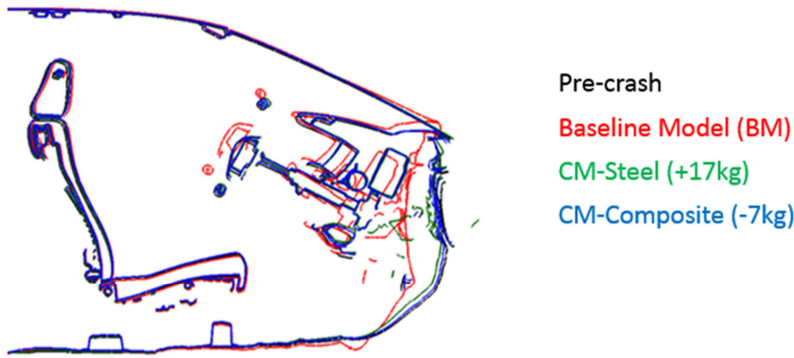
**Figure 12 – NCAP Vehicle Pulse – BM vs. CM-Steel and CM-Composite**

### IIHS Moderate Overlap (40%)

In the IIHS moderate overlap configuration, the tested vehicle travels at a speed of 64 km/h with a 40 percent overlap co-linear into a fixed deformable barrier. In the full-scale test, the vehicle is equipped with a 50th percentile male Hybrid III dummy in the driver seat. The structural rating is based on comparison of intrusion measurements with rating guidelines for the upper and lower occupant compartment.

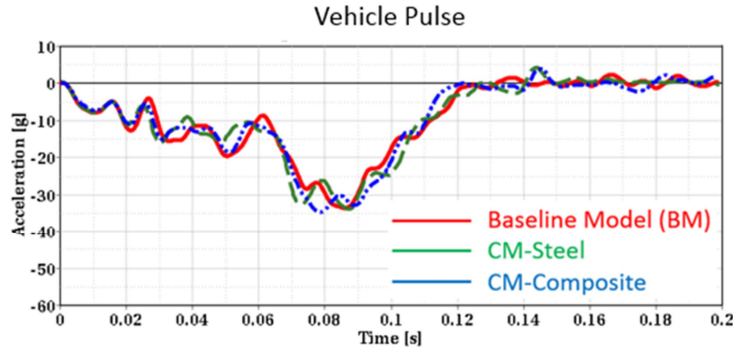
The effect of structural countermeasures developed for NHTSA’s oblique impact was evaluated for the IIHS moderate overlap load case. The CM-Steel vehicle with countermeasures using high-strength steel (+17 kg) and the CM-Composite vehicle with six layers (-7 kg) were evaluated with respect to the baseline model.

Figure 13 shows a cross-section view on the driver side. The geometrical shape of the vehicle “pre-crash” is shown in black. The deformed shape of the BM after the vehicle impact is shown in red. A significant amount of occupant compartment intrusion can be observed for the BM. The vehicle with countermeasures out of high-strength steel (CM-Steel) is shown in green and the CM-Composite vehicle is depicted in blue. No significant occupant compartment intrusion was observed for either countermeasure models. CM-Steel and CM-Composite resulted in a reduction of occupant compartment intrusion compared to the BM in the IIHS moderate overlap load case.



**Figure 13 – IIHS Moderate Overlap – BM vs. CM-Steel and CM-Composite**

Figure 14 shows the vehicle pulse, measured at the rear of the vehicle. An overall similar vehicle pulse was observed for the CM-Steel vehicle, shown in green, and the CM-Composite vehicle, shown in blue. The maximum peak of both vehicles was similar to the BM, shown in red. The maximum peak of the CM-Steel vehicle was slightly lower than the BM. The peak of the CM-Composite vehicle occurred marginally earlier than the BM. No significant effect with respect to restraint system performance and occupant injury risk due to the introduced structural changes for CM-Steel and CM-Composite was therefore predicted.



**Figure 14 – IIHS MO Vehicle Pulse – BM vs. CM-Steel and CM-Composite**

**IIHS Small Overlap (25%)**

In the IIHS small overlap configuration, the tested vehicle travels at a speed of 64 km/h with a 25 percent overlap co-linear into a fixed rigid barrier. In the full-scale test, the vehicle is equipped with a 50th percentile male Hybrid III dummy in the driver seat.

The effect of structural countermeasures developed for NHTSA’s oblique impact was evaluated for the IIHS small overlap load case. The CM-Steel vehicle with countermeasures using high-strength steel (+17 kg) and the CM-Composite vehicle with six layers (-7 kg) were evaluated with respect to the baseline model.

Figure 15 shows a cross-section view on the driver side in the IIHS small (25%) overlap configuration. The geometrical shape of the vehicle “pre-crash” is shown in black. The deformed shape of the BM after the vehicle impact is shown in red. A similar amount of occupant compartment intrusion can be observed for the BM, the vehicle with countermeasures out of high-strength steel (CM-Steel), shown in green, and the CM-Composite vehicle, depicted in blue.



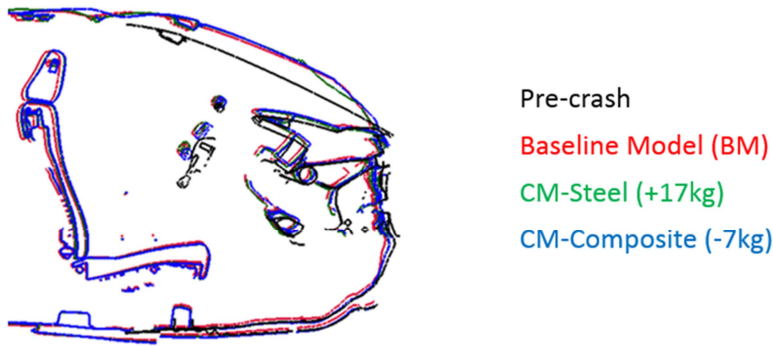


**Figure 15 – IIHS Small Overlap – BM vs. CM-Steel and CM-Composite**

Figure 16 shows the vehicle pulse, measured at the rear of the vehicle. An overall similar vehicle pulse was observed for the CM-Steel vehicle, shown in green, and the CM-Composite vehicle, shown in blue. The maximum peak of both vehicles was similar to the BM, shown in red. The maximum peak of the BM, CM-Steel vehicle, and CM-Composite vehicle was smaller than for other co-linear impact configurations. No significant effect with respect to restraint system performance and occupant injury risk due to the introduced structural changes for CM-Steel and CM-Composite was therefore predicted.

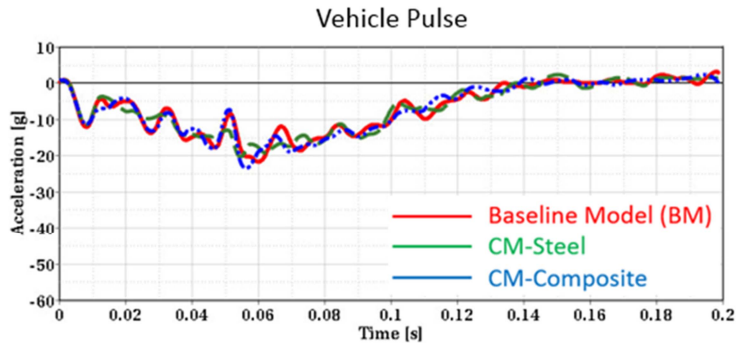


**Figure 16 – IIHS SO Vehicle Pulse – BM vs. CM-Steel and CM-Composite**

## MATERIAL MODEL DEVELOPMENT

In an ongoing effort in cooperation with Honda R&D, a shell element version of Material Model MAT\_213 in LS-DYNA for simulation of composites is being developed and validated. Between 2015 and 2018, the National Aeronautics and Space Administration (NASA), the Federal Aviation Administration (FAA), the Arizona State University (ASU), the George Mason University (GMU), and the Ohio State University's (OSU) composite material modeling consortium has sponsored the development of a material law (MAT\_213) in the commercial LS-DYNA code for the simulation of composite materials under ballistic loads.

The MAT\_213 has some features, such as (1) a deformation model involving elastic and plastic deformations, (2) dependency of strain-rate and temperature, (3) a damage model, (4) a failure model, and (5) a stochastic variation model. The model is driven by tabular data that is generated either using laboratory tests or via virtual testing. However, this material law was implemented for solid elements only.

In cooperation with Honda, GMU is implementing this material law for plane stress conditions so that it can be used by shell elements based on thin shell theory. This will allow for applying the material law to the simulation of thin panels undergoing loads occurring in automotive crash applications.

Current activities includes code development and verification, characterization of a material law for a composite material based on coupon testing, comparison of different discretization techniques when used in conjunction with MAT\_213 for solids and/or shells, and validation of the material model based on component testing.

Many coupon tests are required to develop the material parameters of the material model for a particular composite. The developed material model will be validated by component test simulations, such as head form impact test and static/dynamic crush tests.

The material development and validation efforts within the formed consortium is of significant relevance for the research conducted by GMU for ACC. Honda is planning to share this work with plastic and composite material suppliers to allow them to develop material models of their composite products. That way, OEMs can directly use the material models provided from suppliers to be used in crash simulations for component designs and other analyses.

It is anticipated that this new material model will allow for better simulating and predicting the crash performance of components made out of composites in the future. Plastic and composite material suppliers can use methods and tools developed by the GMU Team in previous projects to evaluate their components in relevant crash loading conditions.

## CONCLUSIONS

This research project helped to further understand the numerical polymer/composite material models and their CAE applications.

NHTSA found that oblique crashes represent common real-world accident patterns. The risk of injury in oblique impact configurations is often higher than in co-linear crashes. IIHS found that the risk of lower extremity injury was higher in the oblique impact tests compared to small overlap co-linear impact tests. The development of countermeasures for both restraints and vehicle structure for oblique configurations will therefore potentially improve vehicle safety and reduce injury risk in the future. Consequently, NHTSA is considering adopting a frontal oblique impact configuration into its NCAP rating protocol. NHTSA has contracted GMU in a previous project to evaluate structural countermeasures using high-strength steel materials, including associated mass, to reduce occupant compartment intrusion in the oblique impact condition.

A FE model of an appropriate mid-sized passenger vehicle was developed and validated to match the acceleration and intrusion measurements available from full-scale crash tests. Crash mechanisms that specifically contributed to high intrusion in the oblique impact condition were analyzed. Local deformation and buckling of the toe-pan, was found to be mainly responsible for producing high intrusions for both left-side and right-side oblique configurations.

A 60% reduction of the maximum intrusion was defined as the main design goal. Another design goal was to maintain moderate vehicle pulses in all impact configurations as a prerequisite for good restraint system performance and low injury risk in current and future rating tests. A model with a possible set of countermeasures using high-strength steel materials (CM-Steel) was developed. The associated increase in vehicle mass for the CM-Steel vehicle compared to the BM was +17 kg.

In the current project, countermeasures using composite material, i.e., Carbon Fiber Reinforced Plastic (CFRP), were developed to achieve a similar reduction in occupant compartment intrusion ("CM-Composite"). The associated reduction in mass for the CM-Composite was -7 kg compared to the BM and -24kg compared to the CM-Steel vehicle.

The change in vehicle pulse due to the developed countermeasures was not significant for oblique and co-linear impacts. Therefore, no unintended consequences were predicted.

In a parallel effort in cooperation with Honda R&D, a shell element version of Material Model MAT\_213 in LS-DYNA for simulation of composites is being developed and validated. This will allow for better simulating and predicting the crash performance of components made out of composites in the future.

## REFERENCES

- [1] Brecher, A., November 2007, "A Safety Roadmap for Future Plastics and Composites Intensive Vehicles, Report No. DOT HS 810 863, Washington, DC: National Highway Traffic Safety Administration.
- [2] Brecher, A., Brewer, J., Summers, S., & Patel S, 2009, "Characterizing and Enhancing the Safety of Future Plastic and Composite Intensive Vehicles," 21st International Conference on the Enhanced Safety of Vehicles, Stuttgart, Germany.
- [3] Barnes, G., Coles, I., Roberts, R., Adams, S. O., Garner, D. M., 2010, "Crash Safety Assurance Strategies for Future Plastic and Composite Intensive Vehicles (PCIVs)," Report No. DOT-VNTSC-NHTSA-10-01, Cambridge, MA: Volpe National Transportation Systems Center.
- [4] Fisher, M., & Cundiff, B., 2002, "APC Vision and Technology Roadmap for the Automotive Market - Defining Priority Research for Plastics in 21st Century Vehicles," SAE Technical Paper 2002-01-1890, Warrendale, PA: Society of Automotive Engineers.
- [5] Fisher, M., Kolb, J., & Cole, S., 2007, "Enhancing Future Automotive Safety with Plastics." Paper No. 07-0451, 20th International Conference on the Enhanced Safety of Vehicles, Lyon, France.
- [6] ACC Plastics Division, 2009, Retrieved from "Plastic in Automotive Markets Technology Roadmap – A New Vision for the Road Ahead," Available at [www.plasticscar.com/roadmap\\_fullversion](http://www.plasticscar.com/roadmap_fullversion).
- [7] ACC Plastics Division. 2009, Plastic and Composite Intensive Vehicles: An Innovation Platform for Achieving National Priorities," Available at [www.plastics-car.com/pcivs](http://www.plastics-car.com/pcivs).
- [8] ACC Plastics Division, 2014, "Plastics and Polymer Composites Technology Roadmap for Automotive Markets," Available at <http://www.plastics-car.com/Tomorrows-Automobiles/Plastics-and-Polymer-Composites-Technology-Roadmap>.
- [9] Park, C-K., Achstetter, T., Kan, C-D., Hollowell, W., 2017, "Understanding of Numerical Polymer/Composite Material Models and Their CAE applications," George Mason University Final Report.
- [10] Bean, J., Kahane, C., Mynatt, M., Rudd, R., Rush, C., Wiacek, C., 2009, National Highway Traffic Safety Administration, "Fatalities in Frontal Crashes Despite Seat Belts and Air Bags", Report No. DOT HS 811 202.
- [11] DOT / NHTSA, December 2015, "New Car Assessment Program (NCAP), Request for Comments," Federal Register Vol. 80 No. 241.
- [12] Zhang, R., Reichert, R., Kan, C.-D. and Cao, L., 2015, "Evaluation of driver lower extremity injuries in 16 oblique crashes with THOR", International Journal of Crashworthiness, doi: 10.1080/13588265.2015.1120983.
- [13] Mueller, R., 2017, "Comparison of Frontal Crash Modes: IIHS Small Overlap and NHTSA Oblique", Insurance Institute for Highway Safety, SAE Government/Industry Meeting, Washington, DC.
- [14] Saunders, J., Craig, M.J., Suway, J., 2011, "NHTSA's Test Procedure Evaluations for Small Overlap/Oblique Crashes," The 22nd International Technical Conference for the Enhanced Safety of Vehicles, Paper No. 11-0343.
- [15] Reichert, Rudolf and Kan, Steve, TBD, "Structural Countermeasure Research Program," NHTSA Contract DTNH2215D00005/0001, Final Report to be published.
- [16] Park, C-K., Kan, C-D., Hollowell, W., & Hill, S.I. December 2012, Investigation of Opportunities for Lightweight Vehicles Using Advanced Plastics and Composites, Report No. DOT HS 811 692, Washington,

DC: National Highway Traffic Safety Administration. Available at [www.nhtsa.gov/DOT/NHTSA/NVS/Crashworthiness/Plastics/811692.pdf](http://www.nhtsa.gov/DOT/NHTSA/NVS/Crashworthiness/Plastics/811692.pdf)

# FRONT SEATBACK STRENGTH IMPROVEMENTS STUDY IN REAR CRASH EVENTS

Velayudham, Ganesan  
Paraneshkumar, Jayakumar  
James, Davies  
Wade, Bridges  
EDAG Inc.,  
USA

Paper Number 19-0134

## ABSTRACT

National Highway Safety Administration (NHTSA)'s seat back standard FMVSS No. 207 [1] establishes a minimum strength requirement to reduce occurrence of seat back collapse in rear crash events. NHTSA also has a separate standard for head restraints. FMVSS No. 202a, that is intended to mitigate whiplash injuries in rear end crashes. In general, seat backs in current production vehicles will not significantly deform or collapse when subjected to the FMVSS No. 202a test pulse. Thus, a more severe test impulse would be needed to demonstrate a change in seat back performance in a rear impact. Recently rear crash events had fatal injuries to rear seat occupants that was attributed to the collapse of a front seat back. This study was to study seat back design changes that could reduce seat back motion in high speed rear impact [2]. The Bio-RID II dummy was used for testing and simulation in this study. This paper provides details of seat back strength changes from a baseline 2014 Honda Accord.

## INTRODUCTION

In this study, detailed Finite Element (FE) models were developed for manual and power operated seats of 2014 Honda Accord vehicle. The FE models were then validated by comparing them to test results of low speed quasi-static seat back pull test reaffirming similarity between FE seats and test seats. In addition, FMVSS 301 high speed rear impact test [3] and simulations were carried out with rear seat occupant models to investigate front seat back dynamic rotation, post-test deformation and injury measures of rear seat occupant. Structural countermeasures were developed to reduce dynamic seat back rotation beyond 20°. Further countermeasures were verified to ensure no impact on whiplash requirement by comparing results from low speed front seat head restraint test and simulation. The mass and cost changes due to structural updates going from current seat design to improved seat design was also reported. This paper provides brief description of FE seat model developed and countermeasure implementation.

## FINITE ELEMENT SEAT MODEL DEVELOPMENT

The vehicle selected for this study was 2014 Honda Accord. Both manual and power seats were considered for investigation. A manual seat with 4-way seat adjustment mechanism and a power seat with 6-way seat adjustment mechanism were used for measurement and testing. In order to develop FE models, the physical seats were scanned and exported to stereolithographic (STL) digital format readable in computer aided design (CAD) tools. The scanned data was processed in CAD tool and meshed in an FE tool accordingly. The thicknesses of the parts were recorded, and the material grades were estimated based on a hardness tests performed on the required seat parts. The scanned CAD data and the FE models of the manual seat and power seat are shown in Figure 1. *Scanned seat and FEA model of Manual and Power seat*. The FE models are also shown in different material grades (provided in the table insert).



**Figure 1. Scanned seat and FEA model of Manual and Power seat**

Separate LS-DYNA FE models were developed for manual and power seats by appropriate FE connections and assembling techniques. This included the detailed modeling of kinematic joints of seat mechanism and seat back recliner mechanism; assembling seat cushion foam and recliner mechanism. The seat cushion foam was pre-deformed to accommodate the occupant shape which was used in the later section of FMVSS No. 301 simulations.

### SEAT BACK PULL TEST

Seat back strength was chosen as the validation criteria to compare FE seat model with physical test. This test was conducted on the manual seat and power seat without cushions and plastic trim in a quasi-static loading condition. The necessary seat fixtures were fabricated to mount the seat at four seat bolts at the four corners of the seat base. A similar loading method stated in FMVSS No. 207 Rearward Moment (49 CFR 571.207 S4.2d, dated 10/1/2016), was used, but it was applied until the seat collapsed. Load was applied at -9 degree about y axis as shown in Figure 2.

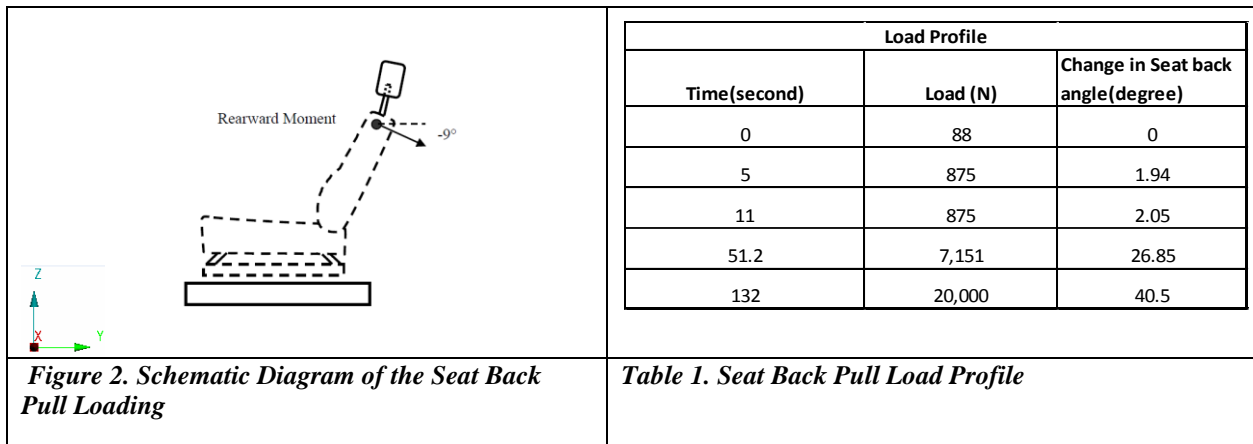


**Figure 2. Schematic Diagram of the Seat Back Pull Loading**

**Table 1. Seat Back Pull Load Profile**

For understanding purpose, seat back pull test setup of the manual seat is briefly described. Seat back pull test setup is shown in Figure 3. The seat was positioned in full down, full rear track position. Load was applied at mounting plate on top of the seat back frame in rearward direction. The load profile shown in Table 1 was used to pull the seat back. The pull load was applied in the rearward direction from 88 N (at 0 seconds) to 875 N (at 5 seconds), and then the load was maintained for the next 6 seconds (per the FMVSS 207 quasi static seat back strength test).



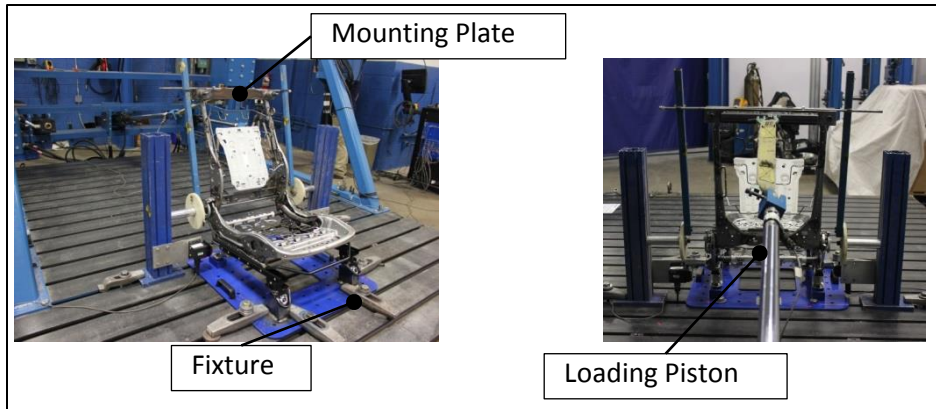
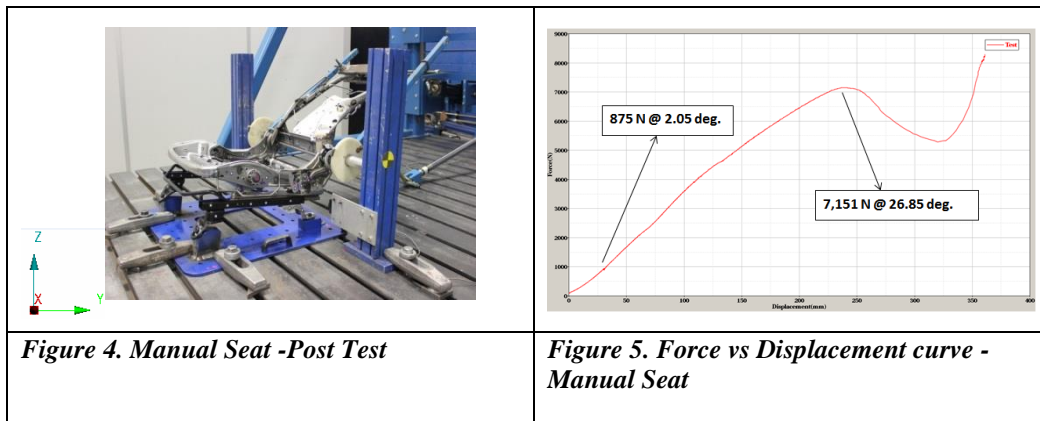


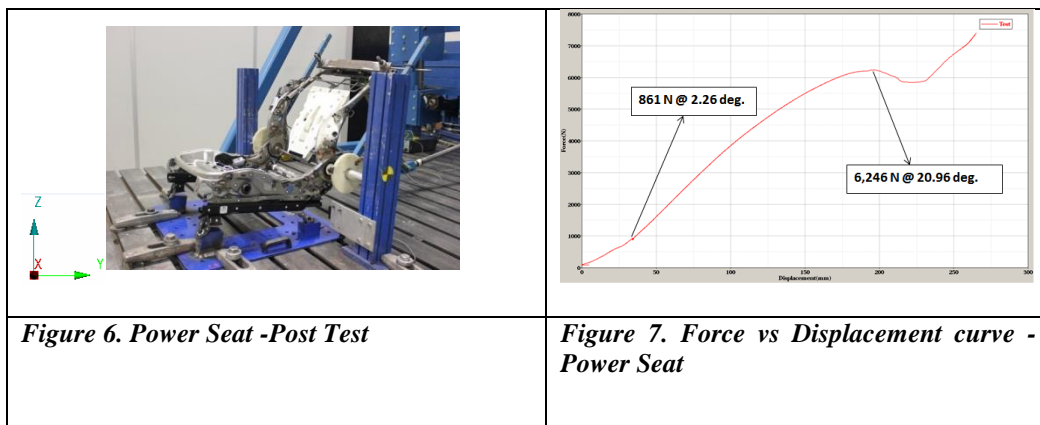
**Figure 3. Seat Back Pull Test Seat Setup – Manual Seat**

Manual seat post-test and Force-Displacement curve from the test are shown in Figure 4 and Figure 5 respectively.



The seat back pull test results of manual seat showed that until 11 seconds there is no deformation or failure. The deformation is observed on the seat bottom frame at the connecting flanges. Significant deformation occurred symmetrically at the seat back frame at the weld joint location. There were no failures or deformation observed on the recliner mechanism. The collapse of the seat started when the seat back angle reached 50.1 degrees from the normal. It was found that the manual seat collapsed at 7,151N.

Similar to the manual seat, the seat back pull test was conducted for power seat in the same full down, full rear track position. Power seat post-test and Force-Displacement curve from the test are shown in Figure 6 and Figure 7 respectively.



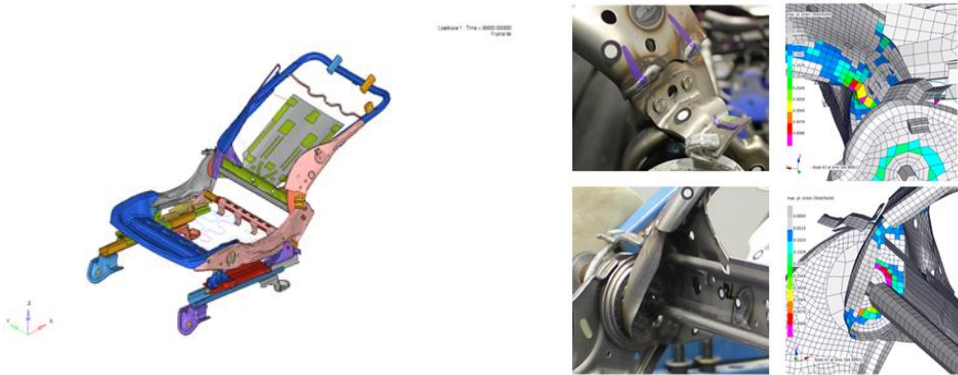
The test results showed that there was no deformation or failures observed in the power seat until 11 seconds. Unlike the manual seat, the power seat frame deformed non-symmetrically due to motor and mechanism in the seatback frame. It was found that the power seat collapsed at 6,246N. The left-hand side (LHS) seat frame deformed more than the right-hand side (RHS) seat frame. (LHS) frame collapsed first at 37.1 degrees and (RHS) collapsed later at 20 degrees respectively.

The detailed test reports for both manual seat and power seat has been provided [4].

### SEAT BACK PULL TEST SIMULATION

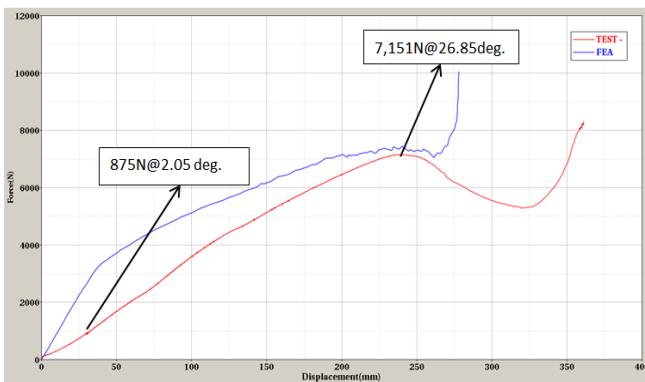
FE simulation of seat back pull test is a quasi-static simulation as per the loading condition. The FE simulation was carried out in quasi-static boundary condition for both manual and power seats. The FE seat models were setup to represent the physical tests accordingly. LS-DYNA simulations were run in implicit mode for 60 seconds. FE simulation results of the manual seat and power seat back were compared with the corresponding physical tests.

Figure 8 shows the global deformation of the collapsed seat frames and the comparison of test and FE simulation at the failed area for manual seat.



**Figure 8. Global deformation of the Seat Frame and Similar Deformation of Test vs FEA – Manual Seat**

The gussets folded inward and failed symmetrically in both test and FEA. In addition to the frame deformation, the seat back strength was compared in terms of stiffness or Force-Displacement (FD) plots. The comparison of FD curves of FE simulation and physical test is shown in Figure 9. The FD curve shows a “CORA” [5] correlation rating of about 78%.



**Figure 9. Force vs. Displacement Curves – Manual Seat**

Similarly, the power seat FE model was also set up to full down, full rear position by adjusting the seat position mechanism. Same method was followed from the manual seat modeling to set up and run power seat pull test simulation. FE simulation results of the power seat back pull test were compared with the physical test. The gussets folded non-symmetrically due to the motor that is located on the right-side gusset, the (LHS) frame collapsed first at 37.1 degrees and (RHS) collapsed later at 20 degrees respectively. The comparison of FD curves of FE simulation and physical test is shown in Figure 10. The FD curve shows a “CORA” [5] correlation rating of about 78%. Thus, both the manual and power FE seat were modeled with acceptable detail and accuracy.

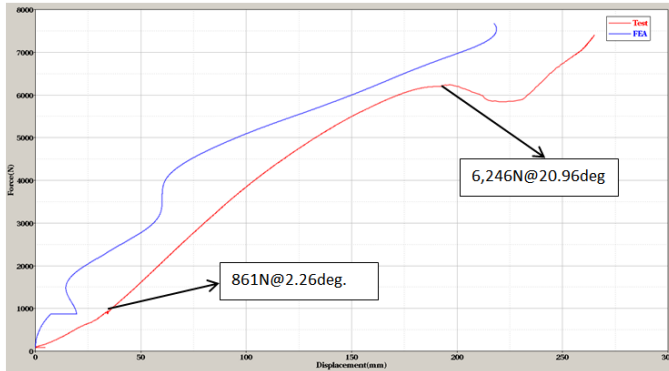


**Figure 10: Force vs. Displacement Curves – Power Seat**

## REAR IMPACT FINITE ELEMENT MODEL DEVELOPMENT

This study was intended to investigate seat design changes to reduce front seat back rotation in rear crash events. It was decided to carry out FE simulations with rear seat passenger using an FMVSS No. 301 crash pulse. Rear impact FE models were developed using a manual seat and a power seat. Each seat model was positioned into an existing 2014 Honda Accord full vehicle model and validated against the sled test results. The rear impact vehicle pulse from 2014 Honda Accord rear impact simulation was used as sled pulse in the test. The sled tests were conducted for both manual and power seats on the physical sleds using this pulse. For example, the rear impact vehicle pulse and the sled test (before and after test) are shown in Figure 11 for manual seat.

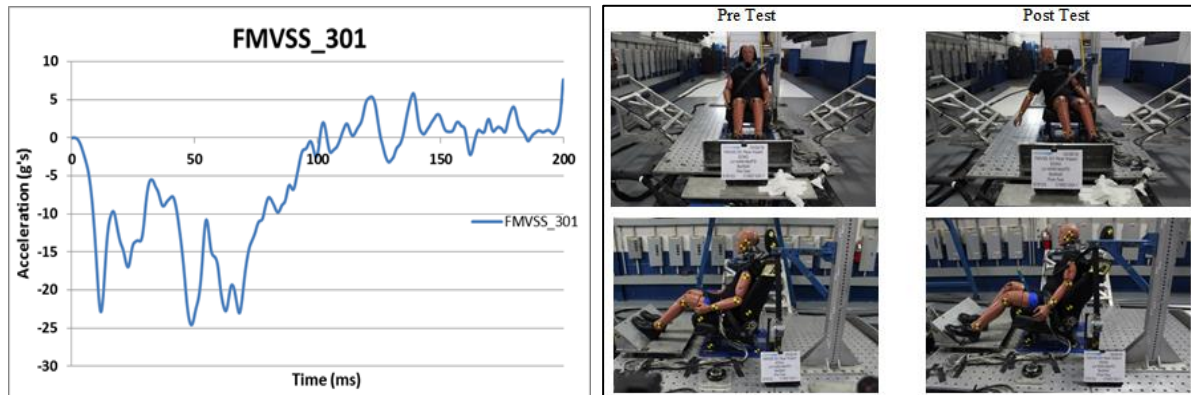


**Figure 11. FMVSS No. 301 Rear Impact Vehicle Pulse and Sled Setup**

The manual seat was tested in mid track and full down seat position with seat back initial position of 18 degrees. The power seat was tested in full rear track and full down seat position with seat back initial position of 18 degrees. The reason for conducting the sled tests for two different seat positions is to understand the seat back strength requirements for nominal and extreme conditions of occupant seating. Occupant characteristics including head acceleration, neck injury parameters and seat back measurements were recorded appropriately. Measured from the

seat back normal, manual seat recorded a dynamic seat back deflection of 38.4° and post-test static permanent deflection of 9.4°. The test conducted on the power seat recorded a dynamic seat back rotation of 38.5° and post-test static permanent deflection of 9°. The FE animations and physical test video showed similar kinematics. The comparisons of HIC, Nij are listed in Table 2. Similar tests were conducted for the power seat, and the summary of the test and FEA results are also included in the table.

**Table 2. FMVSS 301 Sled Test FE Simulations and Test Comparison – Manual Seat and Power Seat**

No.	Injury measures	Manual Seat		Power Seat	
		FEA	Test	FEA	Test
1	HIC 15	80	77	55	76
2	NIJ	0.18	0.28	0.42	0.08

### SEATBACK STRENGTH REQUIREMENT

The next step of the research study was to understand the required front seat back strength to avoid interaction with the rear seat occupant and potential injuries in high speed rear crash. For this purpose, first FMVSS No. 301 high speed rear impact simulations were carried out with rear seat occupants using the validated seat models. The BioRID II FE dummy model was used as rear seat passenger and positioned on the rear seat behind the driver seat. The necessary rear seat head restraint was modeled and integrated in the full vehicle representation of FE model. Unbelted rear seat occupant condition was chosen to be a worst-case scenario. LS-Dyna simulations were run for both manual and power seat. The front seat back rotation and the interaction of rear seat occupant with the front seat were observed. The FE simulations of both manual and power seat clearly showed that the front seat back impacted on the unbelted rear seat passenger behind the driver seat. The severity of front seat with rear seat occupant interaction is shown in Figure 12. The front seat impact on the rear seat occupant knee showed significant contact and femur force which was above 3.5 kN with the seat back angle of 39 degrees with respect to vertical and knee clearance of only 8.06 mm. Cantor, A. (2000) Seatback Strength and Performance study suggests that safe seat back rotation after crash is 15 degrees from initial position [6]. For this study, 20 degrees of seat back rotation is considered as safe criteria. It can be observed that the seat rotation after impact is greater than 35 degrees which is greater than 20 degrees from initial position. The seat back mechanism will be redesigned to limit front seat rotation.

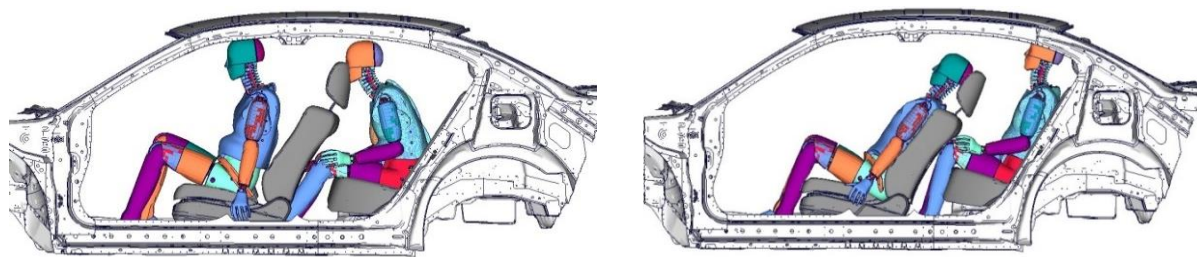


**Figure 12. Front Seat Back and Rear Seat Occupant Interaction**

### SEATBACK STRENGTH IMPROVEMENTS

Having observed that the seat back rotation could contact rear seat passengers in a high speed crash, it was decided to develop necessary structural countermeasures. These countermeasures were implemented on manual and power seat, and FE simulations were run to predict the improvements. Investigation of FE simulation showed that the seat bottom upward movement by the 4-way or 6-way seat mechanism influenced the seat back frame rotation more than the deformation of the seat frame alone. Therefore, Gauge and Grade (2G) optimization was undertaken on the seat bottom frame and bracket members. This approach showed good improvements in reducing the seat back dynamic rotation. The seat bottom frame and mechanism support parts were optimized, and FE simulations were compared with the baseline seats. The gauge and grade changes of the seat bottom frame are shown in Figure 13.

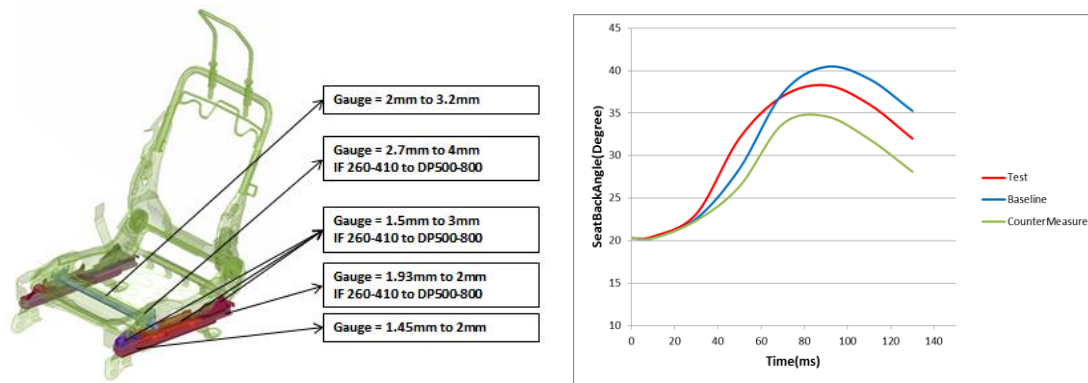


**Figure 13. Seat Bottom Countermeasure and Seat Back Angle (Manual Seat)**

Finally, the countermeasures were validated by means of FE simulations. The 2G optimized seat models were integrated into the FMVSS No. 301 FE model, and simulations were carried out. The outcome of the FE prediction revealed that the seat back angle, knee clearance and knee impact force of the rear seat occupant were reduced due to the effectiveness of the countermeasure. Table 3 shows a comparative summary of the baseline seats and countermeasure seats. In addition to the seat back rotation angle, seat frame-to-knee clearance and femur forces were also included as target performance criteria. When compared to the respective baseline seats, countermeasure seats showed significant improvements. The manual seat countermeasure showed good knee clearance. The femur force is found to be slightly higher, but 3.1 kN is within acceptable limit as per the knee injury criteria. In case of power seat countermeasure, the improvements are seen in all three criteria.

**Table 3. Countermeasure improvements for Manual Seat and Power Seat**

No	Criteria	Target	Manual Seat		Power Seat	
			Baseline	Counter-measure	Baseline	Counter-measure
1	Seat back angle	< 35 deg.	39 deg.	35.2 deg.	38 deg.	35 deg.
2	Seat frame to Knee clearance	> 10 mm	8.06 mm	27.68 mm	3.76 mm	17.23 mm
3	Femur force	< 1.5 kN	5 kN	3.1 kN	3.5 kN	1 kN

The countermeasures were similar on the seat bottom frame parts for both manual and power seats. While structural countermeasures were carried out, it was desired to estimate the cost impact of changing the current design. The cost estimation was done for the baseline and countermeasure seats using standard MIT cost model template. The gauge and grade change influenced an increase in the mass of 2.13 kg and corresponding cost increase of \$1.94 for the manual seat, and an increase of 1.69 kg and \$4.62 for power seat. Cost Impact of the countermeasure seats are shown in Table 4.



**Table 4. Cost Impact of Countermeasure Seats**

<b>No.</b>	<b>Description</b>	<b>Manual Seat</b>	<b>Power Seat</b>
1	Baseline seat weight (kg)	18.81	23.41
2	Countermeasure seat weight (kg)	20.94	25.10
3	Baseline weight of parts affected (kg)	3.87	4.13
4	Countermeasure weight of parts affected (kg)	6.00	5.82
<b>5</b>	<b>Δ weight (kg) / seat</b>	<b>2.13</b>	<b>1.69</b>
6	Baseline cost of parts affected	\$2.24	\$ 9.39
7	Countermeasure cost of parts affected	\$4.17	\$ 14.01
<b>8</b>	<b>Δ cost / seat</b>	<b>\$1.94</b>	<b>\$ 4.62</b>
9	Cost / kg increase	\$0.91	\$ 2.73

It is worth mentioning that FMVSS No. 202a low speed requirement was also carried out to confirm that the developed countermeasures do not affect the whiplash requirement without much deviation from baseline or test.

## CONCLUSIONS AND RECOMMENDATIONS

The seat back strength improvement study for the driver seat was carried out for manual and power operated seats of 2014 Honda Accord vehicle by utilizing CAE techniques in a systematic approach. The dynamic seat back rotation of the front seat against the rear seat occupant was investigated. It was found from FE simulations that the rear seat occupant exhibited significant injury potentials when the front seat back was rotated more than 20 degrees from initial position. Therefore, the seat back strength was improved by implementing necessary countermeasures on the seat bottom frame parts. Further, these countermeasure changes to manual and power seat show minimal cost impact.

It can be noted that the study was limited to one type of occupant which was 50th percentile male. Front seat strength observation in rear impact scenario and front seat back rotation onto rear seat occupant involved using only Bio-RID II 50th percentile male dummy model. The observation of front seat back dynamic rotation causing potential injuries to rear seat occupant and the countermeasures are based on the occupant injuries of 50th percentile male. However, the severity of the injury can vary depending on different occupant (toddlers, children, adult, etc.) and different riding condition such as belted, unbelted, add-on restraint systems.

## REFERENCES

- [1] Department of Transportation, National Highway Traffic Safety Administration, “Federal Motor Vehicle Safety Standards; 571.207 Standard No. 207; Seating Systems,” 49 CFR 571.207
- [2] Saunders JW, Molino LN, McKoy FL, “Performance of seating systems in a FMVSS No. 301 rear impact crash test.” 18th Enhanced Safety of Vehicles (ESV) Conference; 2003.
- [3] Department of Transportation, National Highway Traffic Safety Administration, “Federal Motor Vehicle Safety Standards; 571.301 Standard No. 301; Fuel System Integrity,” 49 CFR 571.301
- [4] Ganesan V, J. P. (2018), Front Seat Modeling in Rear Impact Crashes, Troy, EDAG.
- [5] Partnership for Dummy Technology and Biomechanics, <http://www.pdb-org.com>
- [6] Cantor, A. (2000), Seatback Strength and Performance, Department of Transportation.



## **HEARING LOSS ANALYSIS IN FULL SCALE ACCIDENT RECONSTRUCTION**

Johannes Holtz, Technische Universität Berlin, johannes.holtz@tu-berlin.de, Chair of Naturalistic Driving Observation for Energetic Optimisation and Accident Avoidance, Gustav-Meyer-Allee 25, 13355 Berlin

Gerd Müller, Technische Universität Berlin, gerd.mueller@tu-berlin.de, Chair of Automotive Engineering, Gustav-Meyer-Allee 25, 13355 Berlin

Heiko Johannsen, Johannsen.Heiko@mh-hannover.de, Medizinische Hochschule Hannover, Accident Research Unit, Carl-Neuberg-Str. 1, 30625 Hannover

Andreas Büchner, Buechner.Andreas@mh-hannover.de, Medizinische Hochschule Hannover, German Hearing Centre Hanover, Karl-Wiechert-Allee 3, 30625 Hannover

Marcus Wisch, wisch@bast.de, Federal Highway Research Institute (BASt), Referat F2, Brüderstraße 53, 51427 Bergisch Gladbach

Daniel Huster, huster@bast.de, Federal Highway Research Institute (BASt), Referat F2, Brüderstraße 53, 51427 Bergisch Gladbach

Paper Number 19-0028

### **ABSTRACT**

Airbags are, together with the three-point belt, the most effective passive safety equipment of vehicles. However, literature shows that sound pressure levels of up to 170 dB can occur during airbag deployment. A literature review revealed no systematic experimental data on possible hearing loss by airbag deployment, that also takes any other crash accompanied noise into account, such as deformation and impact noise. Also the rising number of airbags per vehicle resulting in a higher number of deployed airbags in an accident was not addressed with respect to hearing loss. Thus, an extensive test matrix of noise measurements during airbag deployments was conducted including onboard measuring during crashes and static measurements. Dynamic and static experiments with single and multiple airbag deployments were conducted. The results of this study show, that in the analyzed crash constellations the acoustic emission of the collision as well as the car deformation can trigger the stapedius reflex before the airbag deployment. The stapedius reflex protects the inner ear at least partially in case of dangerous sound levels. However, it seems that multiple airbag deployments in a short sequence pose a considerable risk for hearing impairments despite the fully contracted stapedius muscle. Further and in line with Price et al. (2013) it was found that the risk of hearing loss is lower with closed windows. The analysis of patient and accident data showed no link between airbag deployment and hearing loss. This might be caused by low case numbers of reported hearing loss problems up to now.

In conclusion the results show that a singular analysis of the sound pressure of airbag deployments without crash accompanied noises is not sufficient as the protective effect of the stapedius reflex is neglected. Still, successive airbag deployments in a short timeframe raise the risk of hearing loss. Further investigation on hearing impairment due to airbag deployment and triggering of the stapedius reflex is needed and the data acquisition of accidents and patients should consider hearing loss aspects.

## **KEY WORDS**

Airbag, hearing loss, accident reconstruction, stapedius reflex

## **INTRODUCTION**

Casualties show that hearing loss due to airbag deployment in passenger vehicles can be found in medical records of patients (Saunders et al., 1998). Allen et al. (1971) reported sound pressure levels of airbags of up to 170 dB, which is comparable to a gunshot, these sound pressure levels were verified for example by Price et al (1996) for further airbag generations. An exposure to such high sound pressure levels can induce steady hearing loss, which can lead to social isolation. Yaremchuk et al. (2001) analysed 71 patients with otologic symptoms after airbag deployment and showed that the hearing loss that occurred may have affected one or more frequencies. Based on the pure sound pressure level of airbag deployments, Saunders et al. (1998) estimated a 7000 to 28 000 hearing loss injuries due to airbag deployment between 1988 and 1998, but these number of cases were not reflected in clinical data bases or literature (Saunders et al., 1998).

Therefore, we screened accident and patient data to analyze how many cases can be identified based on actual data acquisition and to see if the problem of linking hearing loss statistically to airbag deployment in accidents can be addressed. Despite the low number of hearing loss due to airbag deployment reported by literature, experiments were conducted to address the high sound pressure levels reported in the literature. Previous studies have often neglected the link between the measured sound pressure levels caused by the airbag and noises accompanying a crash such as structural vehicle deformation and impact noises. For example in Rouhana et al. (1994), Price et al. (1996), Rouhana et al. (1998) and Banglmaier et al. (2003) experiments with deploying airbags were conducted with standing vehicle. Therefore, this study aimed to calculate the risk of hearing loss due to airbag deployment in combination with crash accompanied noise. Several aspects were addressed in these experiments. The influence of single or multiple airbag deployments concerning hearing loss was analyzed to address the increasing number of airbags per vehicle resulting in a higher number of airbag deployments in accidents. A comparison between risk of hearing loss caused by airbag deployment in vehicles with opened and closed windows was conducted, because it is not proven yet if a closed compartment lower the load on the inner ear.

## **METHODS**

### **Patient and accident data**

Within this study in-depth accident data from the German In-Depth Accident Study (GIDAS) (Johannsen et al., 2017) were analyzed using accident data with passenger vehicles with production start in 2001 or later. 2053 driver and 533 passengers were considered for frontal collisions with another passenger vehicle, heavy goods vehicle or an object. 1454 near-side occupants and 1392 far-side occupants were considered for side collisions. These cases were analyzed with respect to hearing related injuries based on the Abbreviated Injury Scale (AIS 2005 Update 2008) wherein a tinnitus is the only codable hearing injury in GIDAS. Patient data was analysed based on expert reports of the German Hearing Centre Hanover that address hearing loss linked to accidents with airbag deployment. Another approach to gain patient data was a direct query of all patients of the German Hearing Centre Hanover between May 2016 and April 2017, if their hearing problem is linked to an airbag deployment.

## Accident reconstructions and static airbag deployment experiments

In this study several experiments were conducted to address sound pressure emission of airbags. Two experimental accident reconstructions were conducted twice with different airbag triggering strategies. The first case was a frontal pole impact of a 2008 Seat Leon with 50 km/h colliding speed against a tree with 400 mm diameter and with 95 mm offset. Only the driver airbag was triggered in the experiment by the control unit of the vehicle at 43 ms (the passenger airbag was disconnected). In a variant of this accident reconstruction, the trigger time was set to 20 ms to address the poor chest deflection, all other parameters were set stable. Sound pressure was recorded with two different devices. The NTI Audio Analyzer XL2 with the microphone M4216 was used as an onboard device. This microphone was aligned to the steering wheel centre and attached to the camera stand replacing the passenger seat. The distance between steering wheel centre and microphone was 600 mm. The second sound pressure recorder was a Brüel & Kjaer 2250 with microphone 4189. This external recorder was aligned rectangular to the  $t_0$ -position of the steering wheel centre at the left side of the vehicle with distance 3500 mm and height of 1130 mm, serving as a backup device and for verification purposes. The SAE J247 was not used, because this standard includes only static measurement of acoustic impulses and no acoustical measurements during crash tests.

The second accident reconstruction was a full width rear end collision without offset, where a Fiat 500 (2008) collided with 35 km/h with a standing (hand brake activated) Skoda Fabia (2009) in an under ride situation. The under ride situation was addressed by suspension manipulation so that the lower side of the rear end crossbeam of the Skoda had a ground clearance of 525 mm. The suspension of the Fiat was not manipulated due to minimal ground clearance required by the crash facility of the Technical University of Berlin. The impact speed of 35 km/h was overestimated to ensure an airbag deployment triggered by the control unit of the vehicle. The impact speed of the accident was calculated between 15 and 30 km/h. In a variant of this accident reconstruction the airbag deployment was suppressed, because only marginal airbag interaction was seen for the driver and no airbag interaction was seen for the passenger. The same sound pressure recorders were used similar to the first accident reconstruction. The NTI Audio Analyzer XL2 with microphone M4216 was used as an onboard device. Due to the presence of two dummies in the vehicle the audio analyzer was attached to a mount, that was welded to the outer side of the driver door. The microphone was aligned to the steering wheel centre with a distance of 440 mm. The second sound pressure recorder was a Brüel & Kjaer 2250 with microphone 4189 and positioned similar to the previous accident reconstruction. The two accident cases were chosen based on an analysis of dummy readings addressing suboptimal trigger time in cases with poor structural interaction and unnecessary airbag deployment in accidents with low accident severity to address other work packages of the underlying project. The additional sound pressure measurements were performed parallel.

In order to validate the sound pressure recordings of the accident reconstructions, static analyses of airbag deployments were performed using the same vehicles with the same sound pressure recordings. Additionally, another Brüel & Kjaer sound pressure recorder with five high pressure microphones was used to double the previous microphone positions as a reference and to add other interesting positions inside the vehicle such as headrest of the driver and rear centre seat with direct view to the driver airbag. All microphone positions are shown in Figure 1. The test matrix of the static sound pressure analysis of deploying airbags included experiments to compare the static experiments with the measurements from the accident reconstructions (Seat Leon: driver airbag, Fiat 500: driver airbag, passenger airbag and driver's knee airbag) in order to assess the

influence of the crash accompanied noises such as deformation and impact noises. The driver, passenger, side and curtain airbag of the Seat Leon and the side and curtain airbag of the Fiat 500 were additionally analyzed to address their sound pressure separately and to investigate, if the risk of a hearing impairment is higher for a vehicle with closed or open windows.

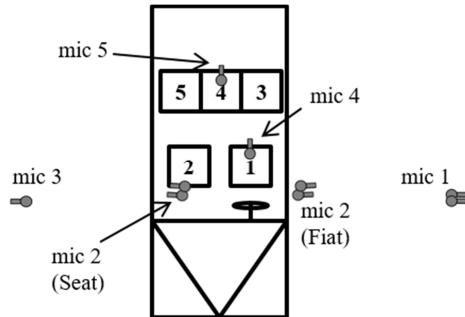


Figure 1: Microphone positions for all experiments, doubled microphones only used for the accident reconstructions

The recorded data were analyzed using the Auditory Hazard Assessment Algorithm for Humans (AHA AH) model that indicates the risk of a Compound Threshold Shift (CTS). A CTS is a reduction in hearing sensitivity due to the combined influence of temporary threshold shift (TTS) and permanent threshold shift (PTS). While a temporary shift recovers over time, the PTS remains as a chronic hearing loss. The AHA AH model was developed in the 80s by Price et al. (1986) and the recordings were analyzed using the version 2.1 from 2013 (Price et al., 2013). The model calculates the risk of a CTS due to blast events such as gunshots or airbag deployments. The AHA AH algorithm models the propagation of sound and blast waves in a free field situation and the transmission in the middle and inner ear. The high nonlinear behavior of the middle ear at high sound pressure levels is implemented in the model. In the analysis of sound pressure levels above 130 dB this nonlinear behavior needs to be considered to avoid overestimation (Price et al., 2013). The AHA AH model also includes the frequency dependent behavior of the 23 segments of the basilar membrane resulting in a calculated segmental deflection of the basilar membrane named Auditory Risk Unit (ARU). A higher deflection leads to a higher risk of damaging the basilar membrane. Experiments with cats, chinchillas and data from voluntary test persons from the 60s and 70s showed a correlation of 0.94 between the CTS and the ARU value following the empiric equation 1 (Price et al., 2013).

$$CTS = 26.6 * \ln(ARU) - 140.1 \quad (\text{Eq. 1})$$

Price et al. (1986) determined a threshold value of 25 dB CTS measured directly after the blast event to expect PTS in humans. This careful assumption corresponds to clinical observations, but due to lack of sufficient data and highly individual behavior the relationship between CTS and PTS could not yet be statistically captured. For example, Liberman et al. (1982) showed in animal studies that a CTS of up to a maximum of 40 dB can fully recover in selected cases, demonstrating the absolute upper limit for a full recovery of hearing thresholds. Regarding the 25 dB CTS by Price et al. (1986) an ARU value of 500 and for the 40 dB CTS by Liberman et al. (1982), an ARU value of 868 is calculated as a limit for obtaining a PTS. In essence, it can be assumed that an ARU value higher than 500 indicates a possible PTS and an ARU value of 868 indicates a definite occurrence of a PTS. A complete risk curve for PTS in dependency of CTS would be highly desirable, but due to the lack of sufficient data and highly individual behavior this is not possible at the current stage. For the analysis of potential hearing loss in our experiments, we will use an ARU value of 500 as the threshold.

The AHAAH model considers two conditions of a test person: warned and unwarned ear condition. Price et al. (2013) elaborated that the risk of hearing loss due to a blast might be affected by the awareness of this upcoming blast event. This effect can be caused by the conditional triggering of the stapedius reflex. While the triggering of the stapedius reflex at sound pressure levels of 90 dB (pure tones) and 80 dB (broadband noise) is non-controversial, the conditional triggering of the stapedius reflex has not yet been proven conclusively. Nevertheless, both conditions are provided by the AHAAH model and will be both applied on our recorded data.

## **RESULTS**

### **Patient and accident data**

The analysis of GIDAS showed that in eight cases with frontal impact and in seven cases with side impact a tinnitus was coded. In a database query on all patients of the German Hearing Centre Hanover between May 2016 and April 2017, two patients linked their hearing problem to an airbag deployment. The analysis of 103 medical reports of the German Hearing Centre at MHH that investigated a potential causality between a hearing loss and an accident with airbag deployment did only reveal a single case where a link between airbag deployment and hearing loss could be demonstrated. These low occurrences correspond to other studies that also found a low number of clinical cases with airbag indicated hearing loss, e.g. Saunders et al. (1998), Traynor (2012) and McFeely et al. (1999).

### **Accident reconstructions and static airbag deployment experiments**

In the first accident reconstruction sound pressure levels up to 134 dB of deformation noise at 18 ms after  $t_0$  were measured which made triggering of the stapedius reflex possible. At 43 ms the airbag deployed and the sound pressure level reaches 160 dB, this maximum value happens in the rising phase of the stapedius muscle, which needs approximately 35 ms to take effect. Nevertheless an ARU value of 276.0 was calculated with the AHAAH in the unwarned condition. In warned condition an ARU value of 256.9 was calculated. In the same accident reconstruction with earlier airbag trigger time (20 ms) an ARU value in the unwarned condition of 452.6 and in the warned condition of 364.0 were calculated. Based on this recording the crash accompanied noises before the airbag deployment were eliminated in the sound file to address a trigger time of 3 ms of the airbag. An ARU value of 615.0 was calculated for this manipulated recording. This shows that the earlier the airbag deploys in the rising phase of the stapedius reflex the higher is the calculated ARU value. As the ARU values with crash accompanied noises were below 500 and therefore of low risk for PTS, the isolated airbag deployment noise indicates a possibility of a PTS. In the second accident reconstruction three airbags deployed: Driver, passenger and driver's knee airbag. The deformation noises lead to sound pressure levels up to 134 dB at 12 ms after  $t_0$  so that the stapedius reflex could be triggered. The first airbag deploys at 67 ms, so that the stapedius reflex is fully developed, however in both conditions an ARU value of 714.4 were calculated for this accident reconstruction. For comparable results the passenger and knee airbag were removed from the audio file and an ARU value of 366.1 was calculated. This shows that the short sequence of airbag deployments (three airbags within 10 ms) can cause a PTS despite the triggered stapedius reflex. In the variant of this accident reconstruction without any airbag deployments an ARU value of 5.3 was calculated, so that the risk of a PTS is very low. With the results of this accident reconstruction with the Fiat, a telephone interview with the driver of the accident vehicle was conducted. The driver confirmed that a tinnitus occurred for one month after the accident, but the tinnitus was not reported to GIDAS and therefore not coded in the GIDAS data. An ear screening to proof if a PTS occurred

was not performed, but it could be assumed that a C5-dip appeared, which does not affect the subjective hearing of the patient, but speeds up presbycusia.

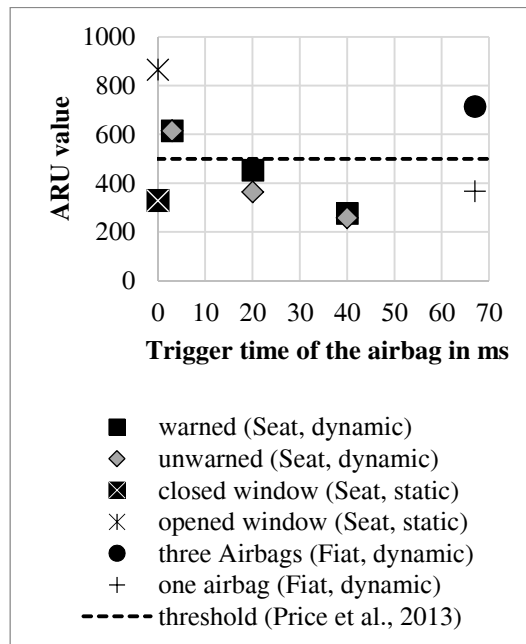


Figure 2: ARU values of the analyzed accident reconstructions (dynamic) and static experiments (airbag deployment in standing vehicle) with respect to the recommended threshold by Price et al. (2013) of 500 ARU

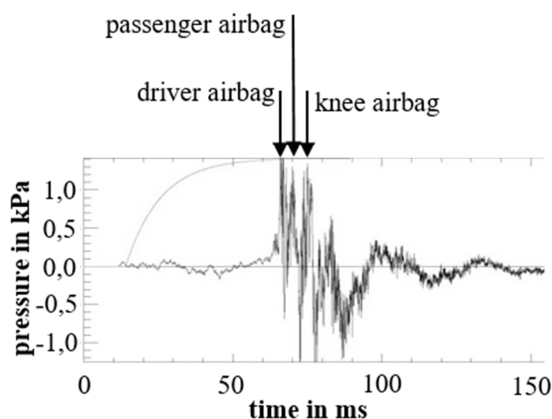


Figure 3: sound pressure graph for the accident reconstruction with Fiat 500, the three airbag deployment events are highlighted resulting in an ARU value of 714.4

The results of the static experiments are based on the recordings of the NTI XL2. The other recordings confirmed the measurements relative to the driver's ear. For example for the deployment of the driver airbag of the Seat Leon a sound pressure of 160 dB was calculated for the driver's ear based on the NTI XL2. The microphone 5 (Figure 1) measured 148 dB in a distance of 1 660 mm, so that both values can be calculated into each other with a failure of 0.36 dB based on the distance law, which describes a drop of 6 dB of sound pressure level per doubling distance. These measurements show that the use of the distance law inside the vehicle is applicable, but direct view between sender and receiver is required. For the driver airbag of the Seat Leon an ARU value of 865.2 was calculated showing a high risk of a PTS, while in the corresponding accident reconstruction an ARU value of 452.6 was calculated in the worst case with a low risk of a PTS. This shows that the stapedius reflex with its protective effect to prevent hearing loss can be triggered by crash accompanied



noises such as deformation noises. A singular analysis of the sound pressure of an airbag addressing the risk of a PTS is not recommended and the crash accompanied noises should be considered.

Comparing the sound pressure from the driver airbag of the Seat Leon with open and closed window, the ARU values for the opened window of 865.2 and 328.8 for the closed window were calculated. The lower value for the closed window is probably based on the static air pressure increase in the vehicle compartment. This forced the eardrum in a position of strong tension and the sound transmission to the inner ear is restricted, comparable to the function of the stapedius reflex.

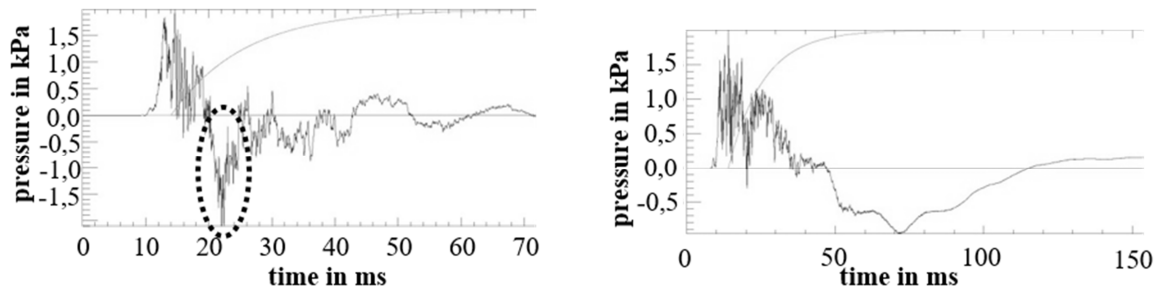


Figure 4: sound pressure graphs for experiment with open (left) and closed (right) window. The negative excursion is highlighted and occur only for open windows

## DISCUSSION

The analysis of patient and accident data showed only a low number of cases. It needs to be investigated whether this is actually based on a low number of cases or if hearing loss is not sufficiently covered by data collections. Several aspects affect the data collection of hearing loss. For example, the patient does not notice a hearing loss immediately because only higher frequencies are affected, that can only be seen in a frequency band. Secondly a hearing loss injury steps in the background of the patient, because other injuries are more obvious or relevant to the patient or thirdly a patient recognizes a hearing loss but did not link it to an airbag deployment. The third point can be addressed by awareness, but the first two points needs to be addressed with audiometry. With more extensive data collections the link between airbag deployment and hearing loss can be assessed statistically.

The accident reconstructions and static experiments were conducted with a limited number of experiments, vehicles and airbags. Continuitive accident reconstructions of other constellations needs to be conducted to support the findings of this study for example full width impact or side collisions. Especially side impacts seem to be interesting, because of the short period of deformation noise before the airbag deployment interferes with the rising phase of the stapedius reflex. Also the selection of vehicles needs to be extended to suspend that the measurements are artefacts of the analyzed vehicles and their acoustical behavior. A continuous on-board recording of sound pressure should be applied to crash tests to collect data for different vehicles and impact conditions. The findings of the comparison of closed and opened windows neglect the accompanied crash noises. Considering the crash noise the ARU value decreases from 865.2 (static experiment with open window) to 452.6 for the case with open window and airbag deployment 20 ms after  $t_0$  (dynamic experiment).

A limitation of this study is that hearing is an individual sense organ that reacts different in every human. So that a complete risk curve for PTS in dependency of CTS is not available at the current stage. For example, there exist so called vulnerable ears that are more sensitive to noise exposure. Ernst et al. (1997) report that 5 to 10 % of the population could be affected by such sensitive hearing. This corresponds to findings by Pfander (1975).

Also the stapedius reflex cannot be triggered in every human. Due to neurologic or anatomical abnormality the stapedius reflex cannot be triggered and the inner ear is unprotected against high levels of sound pressure.

Main limitation of this study is the use of the AHAH model, which is well-established in analysis of gunshots and also in use for automotive analysis since 2003 (Price et al. 2013), but the interpretation of the ARU values and their correlation to PTS and CTS is limited. Only for two values (500 by Price et al. (1986) and 868 by Liberman et al. (1982)) the indication of a PTS is classified, so that the assessment of results close to the two values and in between both values is limited. An approach using injury risk curves for PTS should be a part for future scientific research.

## **CONCLUSION**

In conclusion it was shown that cases with hearing loss after airbag deployment occur in a few cases of patient and accident data. In order to link airbag deployment and hearing loss statistically an extensive data acquisition concerning hearing loss in accidents is needed. The conducted accident reconstructions and the analysis of the sound pressure levels with an on-board microphone showed that sound pressure levels up to 160 dB can occur calculated for the driver's ear. Due to the protective effect of the stapedius reflex, which can be triggered by deformation and impact noise, the risk of a PTS is low for a single airbag deployment. In multiple airbag deployments it was shown that the risk of a PTS is higher due to short sequence of blast events. Due to the increase of the number of airbags per vehicle and higher number of airbag deployments in accidents the number of hearing loss needs to be monitored carefully. Further it was shown, that the risk of a PTS is lower if the windows of the vehicle are closed, due to the air pressure increase inside the vehicle.

For further investigations it should be noticed that measuring the sound pressure of airbags with respect to a risk of a PTS the crash accompanied noises should be considered in the analysis to address the influence of the stapedius reflex. In case of direct view between sender and receiver the distance law is applicable. As recommendation, the sound pressure of airbags should be lowered and unnecessary airbag deployment needs to be avoided. Additionally, the collection of injury data of accidents should address hearing loss to link such injuries to airbag deployment events.

## **ACKNOWLEDGEMENTS**

All data were collected in the project "Accident injuries in vehicles equipped with airbags" (FE 82 0576 2012) funded by the Federal Highway Research Institute (BAST) and conducted by Technical University of Berlin and Hanover Medical School.

## **REFERENCES**

Allen, C.H., Bruce, R.D., Dietrich, C.W., Pearsons, K.S., (1971): „Noise and inflatable restraint systems: final report", Cambridge, Massachusetts: Bolt, Beranek, and Newman

Banglmaier, R.F., Rouhana, S.W. (2003): "Investigation into the noise associated with air bag deployment: Part III – Sound pressure level and auditory risk as function of inflatable device", 47<sup>th</sup> annual proceedings of association for the advancement of automotive medicine

Ernst, A., Lenarz, T., (1997): "Otoacoustic emissions in predicting noise induced hearing loss in vulnerable inner ears", European commission concerted action – protection against noise. University College London

Johannsen, H., Krettek, C., Hannawald, L., Schaser, K.D. (2017): "Consideration of Accident Avoidance Technology within GIDAS". 25th ESV Conference, Detroit, 2017

Lieberman, M.C., Mulroy, M.J., (1982). "Acute and chronic effects of acoustic trauma: Cochlear pathology and auditory nerve patho-physiology." In: *New Perspectives on Noise-Induced Hearing Loss*, pp. 105-135. New York.

McFeely, W.J. Jr, Bojrab, D.I., Davis, K.G., Hegyi, D.F., (1999): „Otologic injuries caused by airbag deployment”, *Otolaryngology – Head and Neck Surgery*, 121(4): 367-73

Pfander, F., (1975): „Das Knalltrauma“, Heidelberg, Springer Verlag, 1975

Price, G.R., Kalb, J.T., (1986): „Mathematical model of the effect of limited stapes displacement on hazard from intense sounds”, *J. Acoustical Society of America*, Supplement 1, Vol. 80

Price, G.R., Rouhana, S.W., Kalb, J.T., (1996): "Hearing hazard from the noise of air bag deployment" *The Journal of the Acoustical Society of America* 99, 2464 (1996)

Price, G.R., Kalb, J.T., (2013): „Using the Auditory Hazard Assessment Algorithm (AHAHAH)", <http://www.arl.army.mil/ARL-Directorates/HRED/AHAHAH>

Rouhana, S.W., Webb, S.R., Wooley R.G., McCleary, J.D., Wood, F.D., Salva, D.B. (1994): "Investigation into the noise associated with air bag deployment: Part I – Measurement technique and parameter study" *SAE Transactions*, Vol. 103, Section 6: *JOURNAL OF PASSENGER CARS* (1994), pp. 1752-1773

Rouhana, S.W., Webb, S.R., Dunn, V.C. (1998): "Investigation into the noise associated with air bag deployment: Part II – Injury risk study using a mathematical model of the human ear" *42nd Stapp Car Crash Conference Proceedings*, Tempe, Arizona, November 2-4, 1998

Saunders J.E., Slattery, W.H., Lux-Ford, W.M., (1998): "Automobile airbag impulse noise: otologic symptoms in six patients", *Otolaryngology – Head and Neck Surgery*, 118(2):228-34

Traynor, R., (2012): "The Effect of Automobile Air Bag Deployment on Hearing", <http://hearinghealthmatters.org/hearinginternational/2012/the-international-threat-of-air-bags/>, accessed September 28, 2018

Yaremchuk, K., Dobie, R.A. (2001): "Otologic Injuries from Airbag Deployment" *Otolaryngology – Head and Neck Surgery*, 125(3):130-34

## INFLUENCE OF SEATING POSITION ON OCCUPANT'S INJURY CRITERIA

Tatsuya Asai, Shinsuke Odai, Hiroyuki Ito, Osamu Kanno

Honda R&D Co., Ltd. Automobile R&D Center

Japan

Paper Number 19-0249

### ABSTRACT

The number of fatalities in traffic accidents has been reduced continuously. One of the factors for such reduction may be improvement of safety devices. However, though total number of deaths has been reduced, many lives are still lost in traffic accidents. Nearly half of the deaths while driving automobile is in frontal crash. On the other hand, driver seating position is variable and the distance between the occupant and occupant restraint system becomes longer in rearmost position (RM) than mid position (MP) of seat slide, resulting in a delay of occupant restraint onset. Because of the delay of occupant restraint, pelvis restraint is also delayed and pelvis displacement increases. At that time, the motion of pelvis increases the tension of lap belt and it is transferred to the inboard shoulder belt through the thorough tongue. Tension in inboard shoulder belt increases the loading to the lower rib cage and may increase the risk of chest injury. This research examined the influence of seating in RM position to the occupant's lower thorax injury and the influence on lower thorax injury by controlling pelvis behaviors in RM position. In this study, finite element (FE) simulations of the sled test in flat56km/h were conducted in MP and RM seat positions. Firstly, it was confirmed that the tension of the lap belt caused by pelvis motion transferred to the inboard shoulder belt and it compressed lower rib cage. Especially it seemed to occur in RM. Secondly, simulation was conducted by changing constraint conditions on pelvis translation and lateral axis rotation to confirm the effect on injury criteria in RM. Since the distance between the instrument panel and the occupant became longer in RM, knees were not constrained by instrument panel(IN-PNE), therefore chest deflection increased. It is confirmed that the lap belt tension was increased with the pelvis forward motion caused by reduction of restraint force, and the tension transferred to the shoulder belt, and consequently the deflection of the lower rib cage was increased. By constraining pelvis translation or rotation, or both of them, the constraint of the pelvis was improved and the chest deflection decreased in each condition. In case of fixing translation and rotation, there was an increase in acceleration of the pelvis and acceleration of T12 also increased through the lumbar spine. Therefore, chest deflection was reduced. In terms of the effect to the tension of seat-belt, there was not transferring of the tension to the shoulder belt from the lap belt. Since the tension of the shoulder belt decreased after 80ms, it was seen that loading to the chest from shoulder belt decreased. It was found that in order to reduce chest deflection in lower right side, it is effective not only reducing the load from inboard shoulder belt but also increasing a degree of constraint on the lumbar spine. Loading to the chest from the inboard shoulder belt was able to be reduced by suppressing pelvis rotation and it was effective to reduce chest deflection further.

## INTRODUCTION

Regulation or assessment for vehicle safety has been revised in each country or region and evaluation standard has become strict. OEMs or suppliers have continuously improved the safety performance of their products to adapt to such standards or to obtain good ratings in assessment, which has been resulting in a certain decrease of fatal accidents. National Police Agency [1] published the total number of deaths in traffic accident in 2018 was the least as far as the statistics in Japan, while they addressed further effort should be necessary to save more lives from significant accident. Traffic Statistics [2] showed nearly half of the deaths in car drivers is in frontal crash.

On the other hand, in many cases, the seats in the first row of automobile have a mechanism of seat-slide for adjusting the seat position from front-most (FM) to rearmost (RM). Since this mechanism allows occupants a wide range of seating position, car driver's seating position becomes variable. When the driver sits on the seat at the RM position, a driver airbag (DAB) and an instrument panel (IN-PNE) becomes farther than the mid-point (MP) of the seat-slide. According to the sled tests conducted by Yaguchi et al. [3] in FMVSS208 and UMTRI seating position, the femoral forces in the case of UMTRI position that was 49mm rearward from MP arose later. Moreover, since it affects the restraint to the pelvis to increase its forward displacement, it could be considered that the tension of the lap belt increases. Then the tension is transferred to the inboard shoulder belt and it compresses the lower rib cage. It was considered that this tendency appeared strongly in the case of RM. Kemper et al. [4] performed dynamic belt loading on PMHS thoraces and confirmed fractures occurred on the inboard side of lower rib cage where the shoulder belt passed first. Shimamura et al. [5] analyzed the detailed data on traffic accidents and reported that the locations of rib fracture were observed more in the lower parts of the thorax. Kent et al. [6] reported that the presence of rib fractures was associated with a significant increase fatality risk, and chest injury was a serious issue. This research examined the influence of seating in RM position to the occupant's lower thorax injury and the influence on lower thorax injury by controlling pelvis behaviors in RM seating position.

## METHODS

In this study, finite element (FE) simulations of sled test were conducted in order to confirm that the tension of the lap belt caused by the increase of pelvis displacement was transferred to the inboard shoulder belt and compressed the lower rib cage. Moreover, how the occupant changed by this effect was also investigated. THOR-Metric finite element (FE) Mode v1.4 developed by Humanetics Innovative Solutions, Inc were used on LS-DYNA R6.1.2 FE code. A collision pulse of a middle size sedan in flat barrier 56km/h test was used for a sled pulse. DAB, seat-belt, IN-PNE and other interior parts were also the same as that vehicle. Firstly, the dummy model was settled on MP or RM of the seat slide range and each calculated result was compared. The seat back angle was set to 22 deg. and the seat height was set to the lower-most position of the adjustable range. Figure 1. shows the seating postures of the dummy models in MP and RM. Accelerometers at the thoracic spine and pelvis, an angular velocity sensor was used to see occupant behaviors. These measurement locations in the dummy structure are shown in Figure 2. For polarity of pelvis angle, the posterior inclination side was defined as positive and the anterior inclination side was defined as negative as shown in Figure 3. Moreover, IR-TRACC

in the lower right side thorax installed in THOR dummy was used for evaluating injury criteria of lower rib cage in case of MP and RM. In order to see the interaction between the lap and shoulder belts due to the pelvis behavior, the tensions of the lap and inboard shoulder belts were used.

Secondly, simulation was conducted by changing pelvis constraint conditions of translation and rotation around the lateral axis to see the tendency of injury criteria reduction due to pelvis constraint in RM seating position. Table.1 shows the simulation matrix. Three constraint conditions of the pelvis were defined. First the translational motion of the hip point (H.P) relative to the center of the seat back recliner was fixed, defined as 'slide fixed' (SF), and second, the rotation around the lateral axis at H.P. was fixed, defined as 'rotation fixed' (RF). Final, both of them were fixed, defined as 'slide and rotation fixed' (SRF).

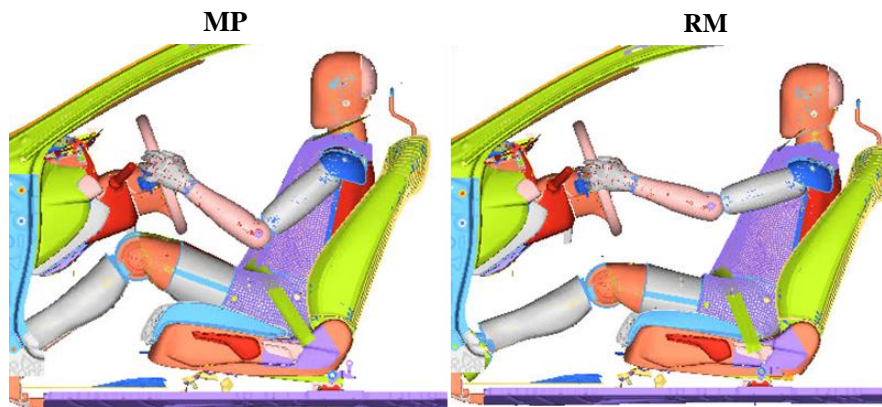


Figure 1. Setups of sled simulation in MP and RM seat positions

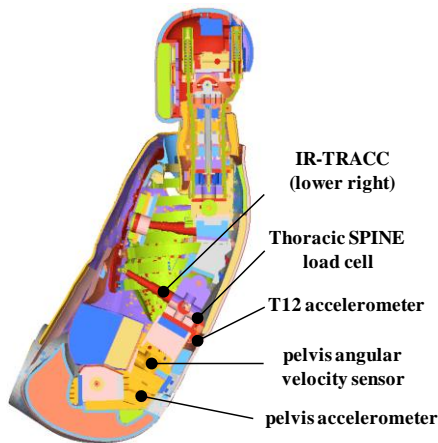


Figure 2. Measurement location in THOR dummy structure

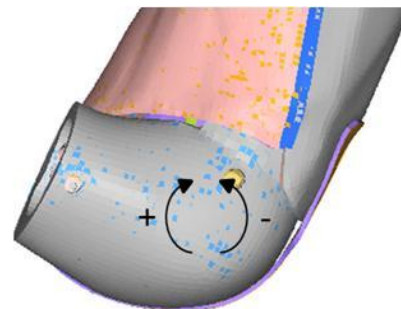


Figure 3. Polarity of pelvis angle

Table 1. Sled simulation condition

	Slide fixed	Rotation fixed
Base CAE (RM)	-	-
CAE No.1 slide fixed (SF)	○	-
CAE No.2 rotation fixed (RF)	-	○
CAE No.3 slide & rotation fixed SRF)	○	○

## RESULT

### Comparing of MP and RM

The restraint conditions at the time when the dummy was restrained by the DAB in MP and RM conditions are shown in Figure 4. Time histories of the acceleration of spine and pelvis, and pelvis angle, chest deflection, shoulder belt tension, and lap belt tension are shown in Figures 5–10. By increasing the distance between the IN-PNE and the occupant in RM seating position, the results show that knees were not constrained by the IN-PNE (Figure 4). In RM seating position, the tension of the lap belt rapidly increased from 60 ms (Figure 9), slightly later than the lap belt, the tension of shoulder belt also increased (Figure 10), the pelvis rotates to the posterior inclination from 40 ms (Figure 8) and acceleration of the pelvis increased greatly from 60 ms (Figure 6). With T12 as well, acceleration of T12 increased greatly from 60 ms (Figure 5), and chest deflection also increased (Figure 7).

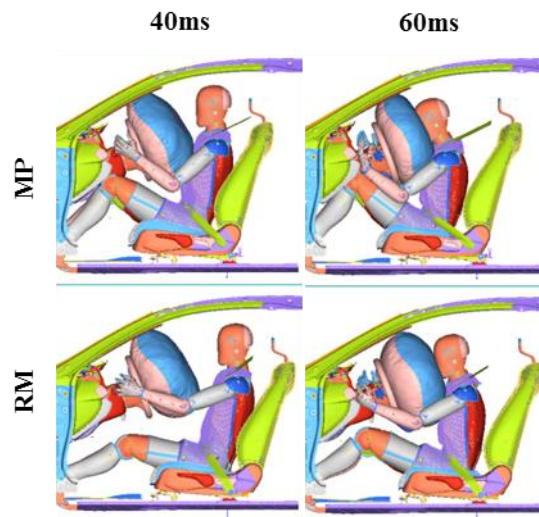


Figure 4. Restraint condition at the time when the dummy was restrained by the DAB in MP and RM

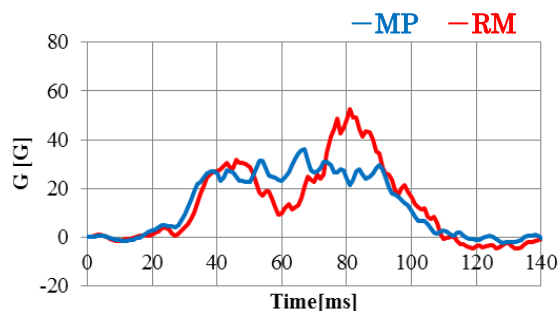


Figure 5. Time histories of T12 accelerometer (X direction) in MP and RM

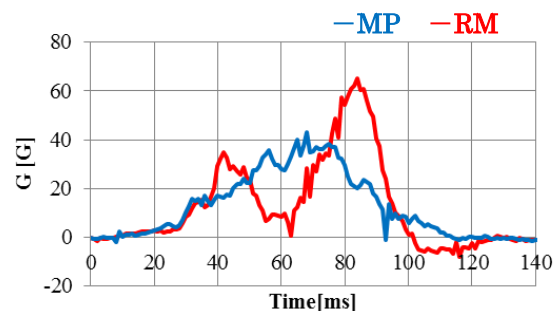
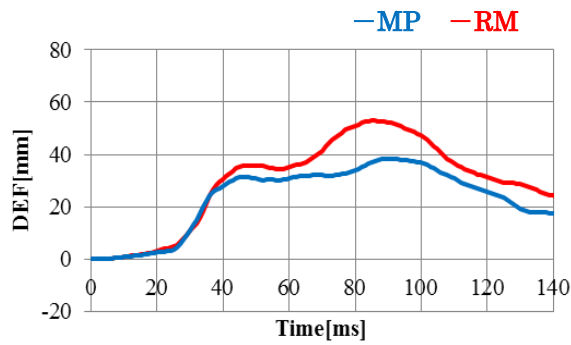
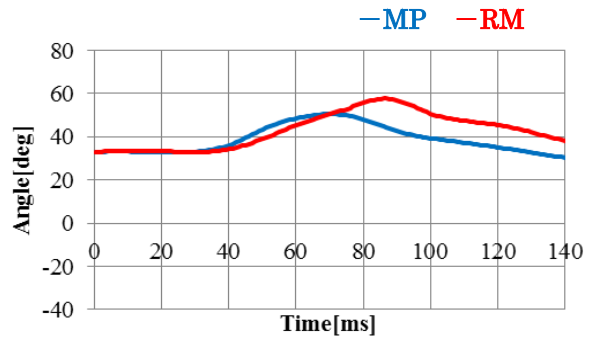


Figure 6. Time histories of pelvis accelerometer (X direction) in MP and RM





**Figure 7. Time histories of chest deflection (lower right) in MP and RM**



**Figure 8. Time histories of pelvis angle in MP and RM**

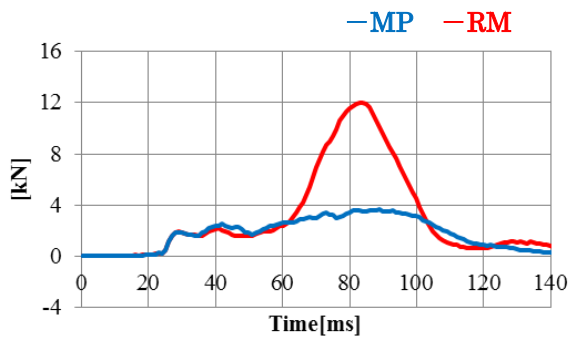


**Figure 9. Time histories of the lap belt forces in MP and RM**

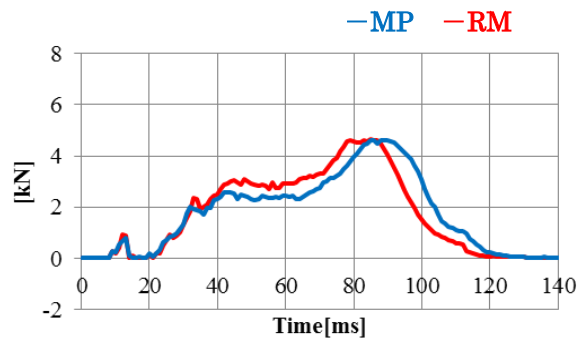


**Figure 10. Time histories of the inboard shoulder belt forces in MP and RM**

### **Investigation of the reduction effect on injury criteria by restraining the pelvis.**

The effect on chest deflection by changing constraint conditions of the pelvis in RM seating position was investigated.

**CAE No.1 slide fixed (SF):** Figure 11 shows the restraint conditions at the time when the Pelvis started to rotate and at the time of maximum chest deflection value in RM and SF. Figures 12–15 show the time histories of the acceleration of spine and pelvis, the pelvis angle and chest deflection. Because the translation motion of the pelvis was fixed in SF, acceleration of pelvis increased at 10–30 ms and decreased at 80 ms compared to RM (Figure 13). In SF condition, the pelvis started to rotate to the anterior inclination from about 30 ms together with the seat deformation and got larger from 60 ms (Figure 15), it was confirmed that acceleration of T12 increased at 10–30 ms (Figure 12). Chest deflection greatly decreased at 40–60 ms and the peak value also decreased (Figure 14).

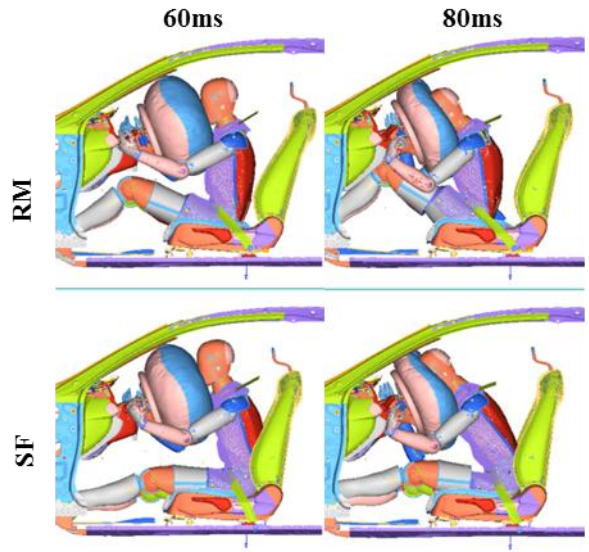


Figure 11. Restraint conditions at the time when the pelvis started to rotate and at the time of maximum chest deflection value in RM and SF.

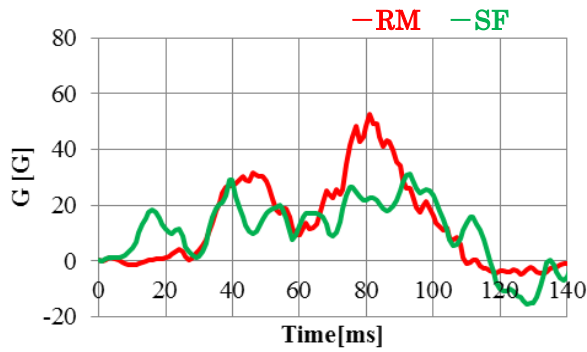


Figure 12. Time histories of T12 accelerometer (X direction) in RM and SF

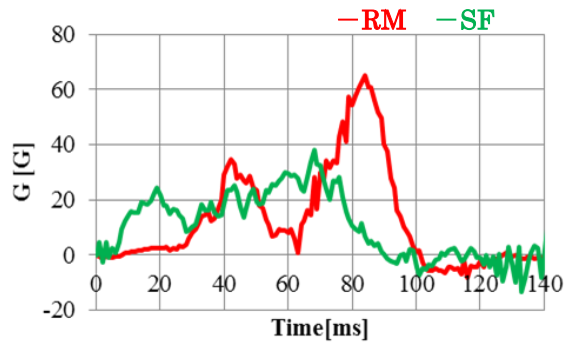


Figure 13. Time histories of pelvis accelerometer (X direction) in RM and SF

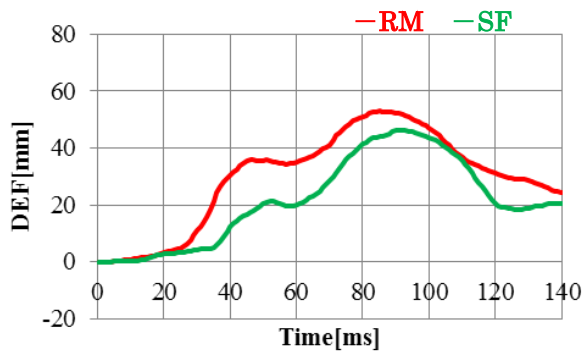


Figure 14. Time histories of chest deflection (lower right) in RM and SF

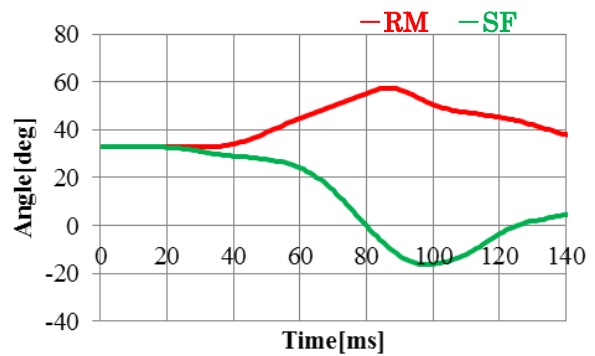
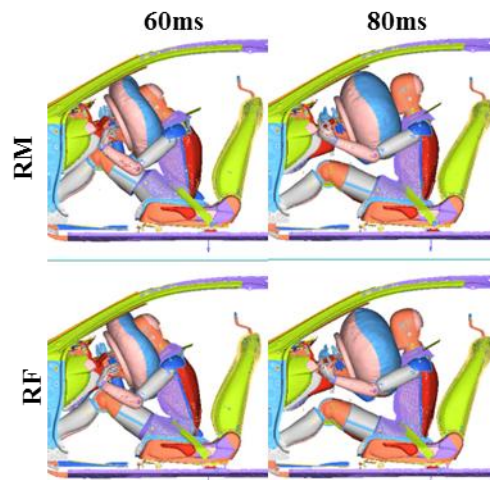
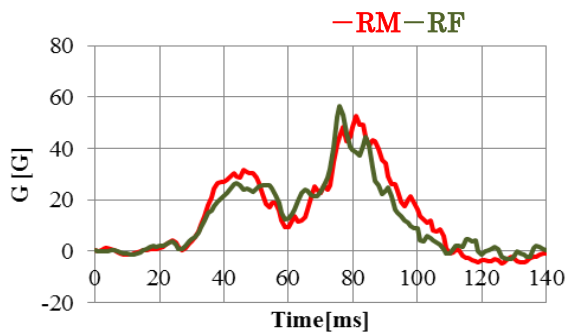


Figure 15. Time histories of pelvis angle in RM and SF

**CAE No.2 rotation fixed(RF):** Figure 16 shows the restraint conditions at the time when the pelvis started to rotate and at the time of maximum chest deflection in RM and RF. Figures 17-20 show time histories of spine and pelvis acceleration, the pelvis angle and chest deflection. Because the rotation motion of the pelvis was fixed in RF, acceleration of pelvis increased at 50ms (Figure 18). The pelvis rotated to the anterior side in RF relative to RM (Figure 20). In RF condition, acceleration of T12 decreased at around 40ms (Figure 17) and chest deflection slightly increased at around 40ms (Figure 19) compared to RM.



**Figure 16. Restraint conditions at the time when the pelvis started to rotate and at the time of maximum chest deflection value in RM and RF.**



**Figure 17. Time histories of T12 accelerometer (X direction) in RM and RF**

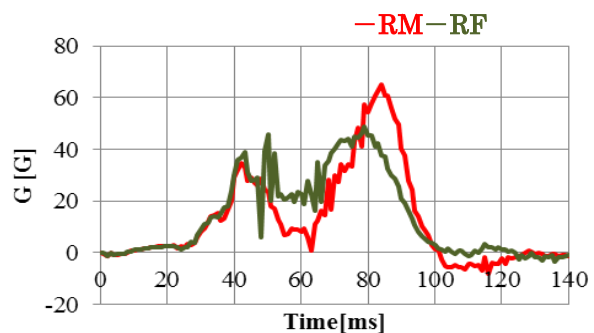


**Figure 18. Time histories of pelvis accelerometer (X direction) in RM and RF**

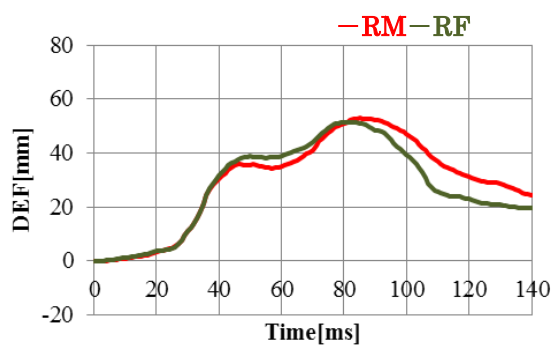


**Figure 19. Time histories of chest deflection (lower right) in RM and RF**

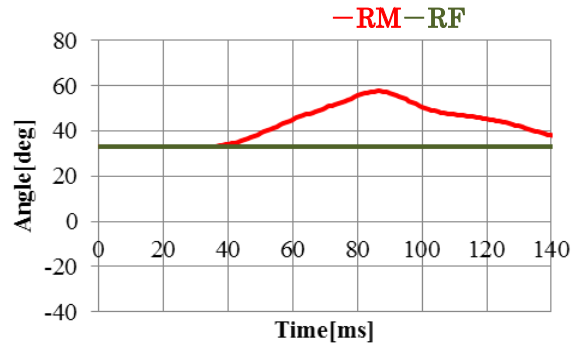


**Figure 20. Time histories of pelvis angle in RM and RF**

**CAE No.3 slide and rotation fixed (SRF):** Figure 21 shows the restraint conditions at the time when pelvis started to rotate and at the time of maximum chest deflection in RM and SRF. Figures 22- 25 show time histories of spine and pelvis acceleration, the pelvis angle and chest deflection. Because the translation and rotation motion of pelvis were fixed in SRF, acceleration of pelvis increased at 10-30ms and decreased at 80ms compared to RM (Figure 23). In SRF condition, the pelvis started to rotate to the anterior inclination from about 20 ms together with the seat deformation (Figure 25), acceleration of T12 increased at 10–30 ms (Figure 22). Increase of chest deflection from 60ms did not appear in RSF while it appeared in RM (Figure 24).

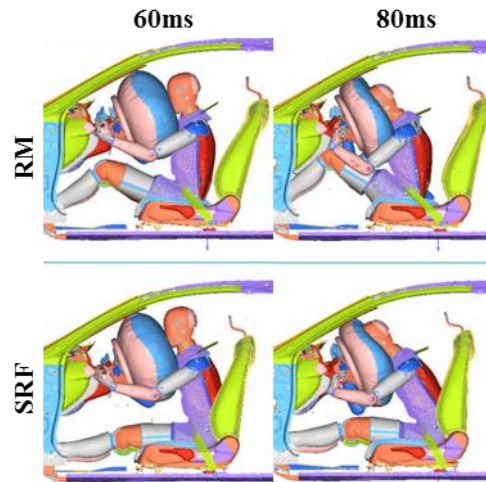


**Figure 21. Restraint conditions at the time when pelvis started to rotate and at the time of maximum chest deflection in RM and SRF**

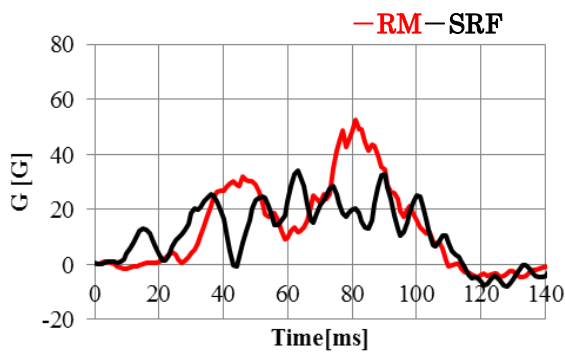


**Figure 22. Time histories of T12 accelerometer(X direction) in RM and SRF**

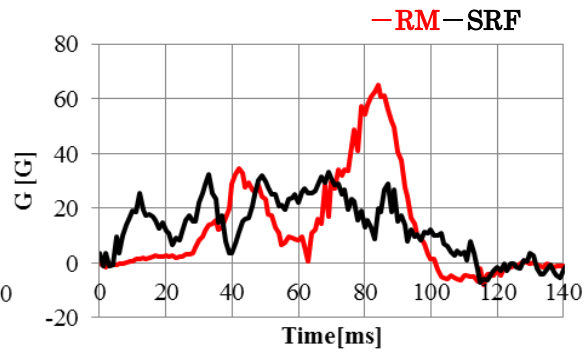


**Figure 23. Time histories of pelvis accelerometer(X direction) in RM and SRF**

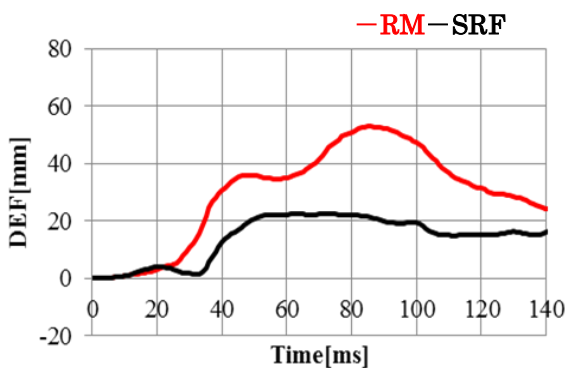


**Figure 24. Time histories of chest deflection (lower right) in RM and SRF**

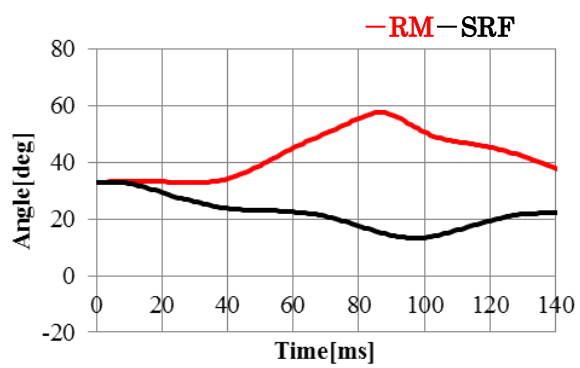


**Figure 25. Time histories of pelvis angle in RM and SRF**

## DISCUSSION

It was discussed that how the difference of seating position and pelvis constrained condition effected to upper body. Comparing MP and RM, because the knees were not restrained by IN-PNE, the lap belt restrained the pelvis in RM (Figure 4, 9). As the RM results showed, it was confirmed that because the pelvis was not restrained and it started forward displacement at initial timing, the lap belt tension increased. Then the tension was transferred to the shoulder belt through the through tongue (Figure 9, 10), and as a result, chest deflection was increased. On the other hand, the increase in chest deflection before 60 ms was caused by decreasing acceleration of T12, which was result from the delay in restraining of the pelvis (Figure 5, 6). To check the effect of the pelvis rotation on the upper body, thoracic load cell shown in Figure 2 was used. The polarity is shown in Fig.26. Although the pelvis rotated to the posterior inclination, the force toward the back of the spine worked together with the rotation of the pelvis as shown in Figure 27, there appeared to be an effect of suppressing the displacement of the upper body. Particularly in RM, the knees were not restrained by the IN-PNE, so the pelvis rotated more to the posterior inclination than in the case of MP, and the effect of suppressing displacement of the upper body was also greater (Figure 8, 27). This made it clear that the delay in pelvis restraint and the behavior resulting from pelvis rotation had an effect on T12 and chest deflection through the lumbar spine.

Therefore the effect of controlling pelvis behavior to T12 and chest deflection thorough lumbar spine was focused on.

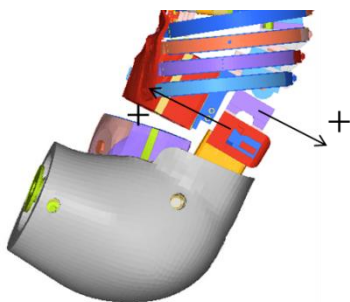


**Figure 26. Polarity of spine Load Cell**

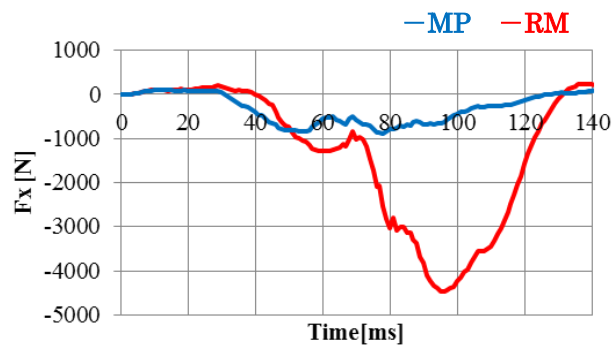


**Figure 27. Time histories of spine load cell (X direction) in MP and RM**

Comparing RM and SF, the effect by fixing the translation motion of the pelvis was confirmed. Because the translation motion of the pelvis was fixed, there was acceleration of the pelvis before 30 ms (Figure 13), and acceleration of T12 also increased through the lumbar spine (Figure 12), and chest deflection was reduced at 40-60ms by its effect (Figure 14). The pelvis started to rotate greatly to the anterior inclination from 60ms, and along with that, the effect of suppressing displacement of the upper body was decreased (Figure 28). The anterior inclination of the pelvis caused the decrease of T12 acceleration and it increased chest deflection, but early restraint of the pelvis was very effective and maximum chest deflection was reduced finally.

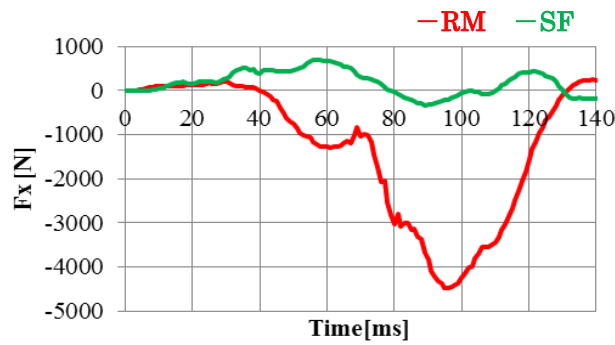


**Figure 28. Time histories of spine load cell (X direction) in RM and SF**

Comparing RM and RF, the effect by fixing the rotation motion of the pelvis was confirmed. Fixing the rotation of the pelvis means there was no rotational behavior of the pelvis, but in RF, the pelvis inclination was more anterior side relative to in RM (Figure 20). The difference in pelvis rotation started to occur from 40ms and the effect of suppressing displacement of the upper body before 60ms was decreased in RM (Figure 29). As a result, there was a decrease in T12 acceleration at 40–60 ms (Figure 17), therefore chest deflection increased (Figure 19). On the other hand, acceleration of the pelvis increased at close to 60–80 ms and it caused a slight increase in T12 acceleration through the lumbar spine (Figures 17, 18). Initially, the relatively anterior inclination of the pelvis causes T12 acceleration to reduce and chest deflection to increase, however, after that, acceleration of the pelvis increased, thus the effect of increasing acceleration of T12 and suppressing upper body displacement was about the same as with RM, and maximum chest deflection was also about the same.

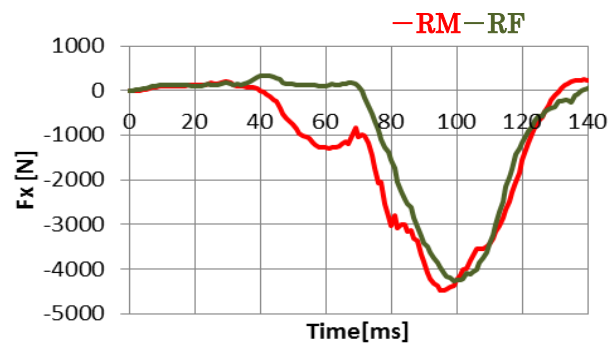


**Figure 29. Time histories of spine load cell (X direction) in RM and RF**

In preceding part, the influence in case of fixing either translation or rotation of pelvis individually was confirmed. The effect of fixing both translation and rotation of pelvis was confirmed. Because the translation of the pelvis was fixed, there was an increase in acceleration of the pelvis before 30 ms (Figure 23), the same as with SF, and acceleration of T12 also increased through the lumbar spine (Figure 22). This effect could be seen up to about 70ms compared to in RM.

As previously mentioned, the effect of pelvis behavior control on chest deflection was confirmed. Next, this section confirmed the effect on shoulder belt tension when both the translation and rotation of pelvis were fixed. The time histories of the shoulder belt and lap belt tensions in SRF are shown in Figure 30, 31. Fixing the translation and rotation of the pelvis increased pelvis acceleration, and for that reason, the lap belt tension did

not increase (Figure 30). Therefore, there was not transferring of the tension to the shoulder belt from the lap belt, and the shoulder belt tension also could be reduced after 80 ms, (Figure 31), thus it was seen that the loading from the shoulder belt to chest was reduced.

This research confirmed that with sled test in flat 56 km/h, reducing the pelvis translation and rotation motion were effective for reducing chest injury criteria. Moreover, lateral behavior of the vehicle affects the occupant in case of angled collision, the extent of these benefits also needs to be determined for these cases to see if controlling pelvis behavior is effective in reducing chest injury criteria in these situations as well.

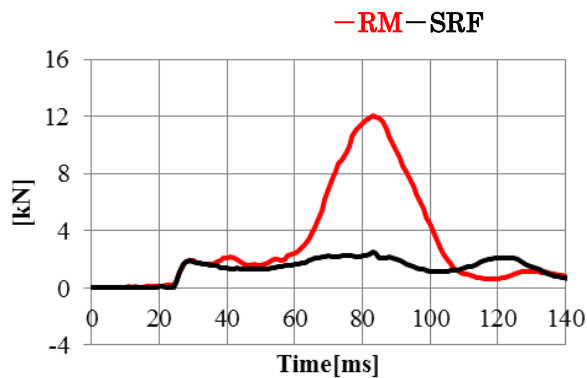


**Figure 30. Time histories of the lap belt forces in RM and SRF**

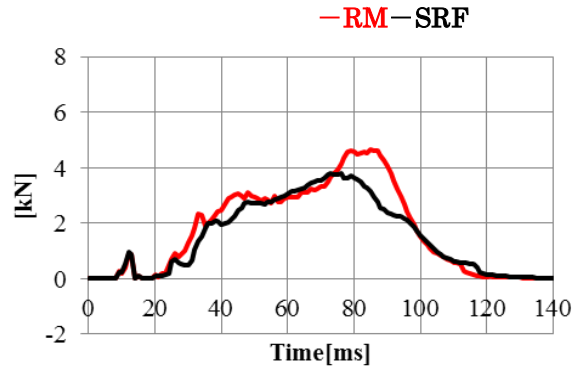


**Figure 31. Time histories of the inboard shoulder belt forces in RM and SRF**

## CONCLUSION

Sled simulation for MP and RM occupant seating positions by using THOR FE model was conducted in this study. In addition, a parametric study which changed the pelvis constrained condition in RM seating position was conducted. As a result, the following were found

- In order to reduce chest deflection in lower right side, it is effective not only reducing the load from inboard shoulder belt but also increasing a degree of constraint on the lumbar spine.
- To improve the constraint on the spine, it is important to constrain the pelvis in early timing to reduce the translation of the pelvis.
- Loading to the chest from the inboard shoulder belt was able to be reduced by suppressing pelvis rotation and it was effective to reduce chest deflection further.



## REFERENCES

- [1] National Police Agency, 2018; Occurrence situation of traffic accident in 2018 [ Published in Japanese]
- [2] ITARDA, 2017; Statistical data.
- [3] Yaguchi, M., Ono, K., Masuda, M., Fukushima, T., SENSITIVITY TO DIFFERENT SEATING POSITIONS OF THOR-NT AND HYBEID III IN SLED TESTING. ESV 13-0333
- [4] Kemper ,A. R., Kennedy ,E.A., Mcnally ,C., Manoogian, S.J., Stitzel , J.D., Duma, S.M., Reducing Chest Injuries in Automobile Collisions:Rib Fracture Timing and Implications for Thoracic Injury Criteria. Annuals of Biomedical Engineering. 2011; 39: 2141-2151
- [5] Shimamura M.,Ohhashi H.,Yamazaki M., The effects of occupant age on patterns of rib fractures to belt-restrained drivers and front passengers in crashes in Japan. Stapp Car Crash J. 2003; 47:349-65
- [6] Kent R., Woods W., Bostrom O., Fatality Risk and the Presence of RIB Fractures. Ann Adv Automot Med. 2008; 52: 73-84

## **INJURY MECHANISM AND EVALUATING METHODS FOR SMALL OVERLAP AND OBLIQUE FRONTAL CRASHES**

**Akihiro Ishida, Satoshi, Takizawa**

Honda R&D Co.,Ltd. Automobile R&D Center  
Japan

Paper Number 19-0232

### **ABSTRACT**

According to a National Highway Traffic Safety Administration (NHTSA) study, small overlap and oblique frontal crashes account for 25% of fatal accidents in the United States. This is a large proportion, and comprises the accident mode with the highest fatality rate. The fact that occupants collide with the cabin is a factor in this. The purpose of the present research is to recreate the injuries that occur to occupants in actual accidents involving small overlap and oblique frontal crashes, and to formulate a method for evaluating them. By enhancing vehicle body performance and occupant restraint performance, the goal is to reduce fatalities and injuries. In order to verify the circumstances of injury during small overlap and oblique frontal crashes, crash simulations were performed by numerical computation. A human body model was also placed in the driver's seat to verify the occupant movement and extent of injury. The oblique mode that the NHTSA is slated to adopt was first verified using numerical simulation, but collision on the occupant's chest could not be confirmed. For the present research, therefore, verification of the angle and speed parameters was carried out so that occupant movement could be recreated in a way that conformed to actual accident circumstances. The result of simulation was that occupant movement with respect to the vehicle together with vehicle body deformation showed the occurrence of collision with the occupant's chest when the evaluation vehicle (a passenger car) was impacted by an OMDB with an overlap (LAP) of 25%, at an angle of 30°, and at a speed of 110 km/h. The collision occurred in the same place, with injury to the same areas, and with the same degree of injury as shown under actual accident circumstances in a small overlap and oblique frontal crash. In light of these results, it was confirmed that injuries would be reduced by increasing the body strength of the evaluation vehicle to reduce deformation and by installing air bags on doors where oblique loading affected occupant movement. Numerical simulation of the above modes was performed using a passenger car that received the highest evaluation from the Insurance Institute for Highway Safety (IIHS). While vehicle body deformation was evaluated at the GOOD level even in oblique mode (in-house data), vehicle body deformation increased and occupant chest collision occurred that resulted in AIS4+ level injuries. This method of evaluation was confirmed to offer possibilities for evaluation of small overlap and oblique frontal crashes that conforms to actual accidents, and for evaluation that may further reduce fatalities and injuries. The effectiveness with respect to these injuries of measures taken through restraint devices and the vehicle body by means of numerical simulation using a human body model was verified. The results confirmed that combining vehicle body and restraint device measures had the effect of reducing injuries.

## INTRODUCTION

Attention in the United States is being focused on small overlap and oblique frontal crashes because these types of crashes often result in fatal accidents even though the vehicle has the most up-to-date body technology and safety equipment. According to an NHTSA study, small overlap and oblique frontal crashes account for 25% of fatal accidents in the United States, which is a large proportion, making this the accident mode with the highest fatality rate [1]. According to Rudd et al. [2] it has been reported that in small overlap and oblique frontal crashes, 45% of AIS3+ injuries to occupants in the driver's seat are to the chest and 38% to the head. It is clear that causal factors in those injuries to the head are collision with the A-pillar, and to the chest, collision with the door, resulting in the large proportions of these injuries. One distinctive feature in the case of the chest, in particular, is that the ribs on the non-belted side collide with the door, causing fracture injuries. It is reported more chest injuries with the door as a factor in small overlap crashes than in co-linear crashes, and they consider these to be the result of the occupant's lateral motion and deformation of the vehicle body. Iraeus et al. [3] defined the crash mode accompanied with lateral movement as an oblique mode. They studied the mechanism of chest injury during oblique crashes using a human body model, and indicated that fractures occurred when the load input from the seatbelt caused the body to bend in a longitudinal direction so that the rib cage bulged outward on the side, and the lateral motion of the body caused that side to crash into the door trim, resulting in fracture. There are also the findings in Lindquist et al. [4] and Brumbelow et al. [5] that the sites of fractures that occur in small overlap crashes in real-world accidents extend throughout the entire left side (ribs 1 to 12), with a particularly large number in ribs 1 to 10, which attach to the sternum.

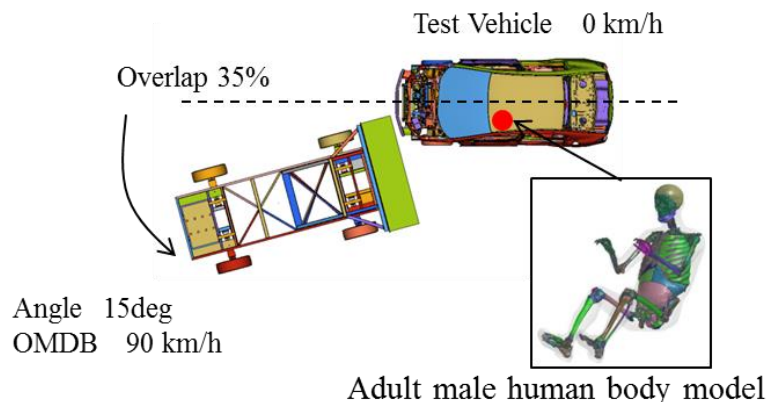
In order to achieve further advances in vehicle body safety performance with regard to small overlap and oblique frontal crash accident patterns, and to reduce the distinctive injuries in such types of accidents, the Insurance Institute for Highway safety (IIHS) initiated a new evaluation in 2012 for the purpose of reducing injuries from small overlap and oblique frontal crashes. The SOT (Small Overlap Test) evaluation tests of the IIHS involve crashing a vehicle into a rigid barrier with 150-mm curvature on the corners at a speed of 64 km/h and the front end offset 25%. The NHTSA is considering revision of the New Car Assessment Program (NCAP) with a test method (Oblique test) using an Oblique Moving Deformable Barrier (OMDB) with attached aluminum honeycomb that collides with the test vehicle at a speed of 90 km/h and at an angle of 15° with a 35% offset in a small overlap crash for evaluation.

The present research sought a reduction in fatalities and injuries by focusing attention on the chest, in particular, as the location of injuries in small overlap and oblique frontal crashes, and devised an evaluation method that could enable reduction of those injuries. A numerical simulation was first implemented using a passenger car in the oblique test that is currently scheduled to be adopted for the NCAP. This approach used an adult male human body finite element (FE) model to verify the occurrence of the occupant's chest collision with interior car body, and it sought test configurations that would recreate the injuries sustained in actual small overlap and oblique frontal crash accidents. It also used an OMDB FE model to verify configurations that make it possible to evaluate the vehicle. Directions to be taken in measures addressing this issue of injuries to the chest were examined in terms of both vehicle body and restraint device measures necessary for reducing future fatalities and injuries.

## METHODS AND RESULTS

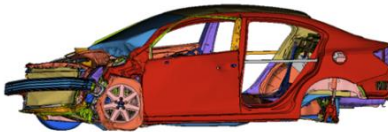


### Reproducibility of chest injury by Oblique test

Crash simulations were conducted by numerical simulation using an explicit FE code. LS-DYNA(v971 6.1.2) to verify the actual injuries sustained in small overlap and oblique frontal crashes. A human body model was set on the driver's seat (DR) to verify the occupant movement and extent of injury. The human body model used for this was an adult male model developed by Ito et al.[6]. Current human body models only allow for whole body movement and fracture prediction, and cannot be used for direct evaluation of more serious (life-threatening) injuries to internal organs. Evaluation was therefore performed according to the number of fractured ribs predicted by the numerical simulation from the relationship between the rib fractures throughout the chest of the L side which is characteristic of the chest injury indicated by the above-mentioned past study. The simulation was first conducted through a configuration of the oblique test protocol scheduled to be adopted by the NHTSA[7]. The vehicle used for verification was a 2011 model year small passenger car. The vehicle model had a driver air bag and a 3-point seat belt as a restraint device. Figure1 shows the configuration



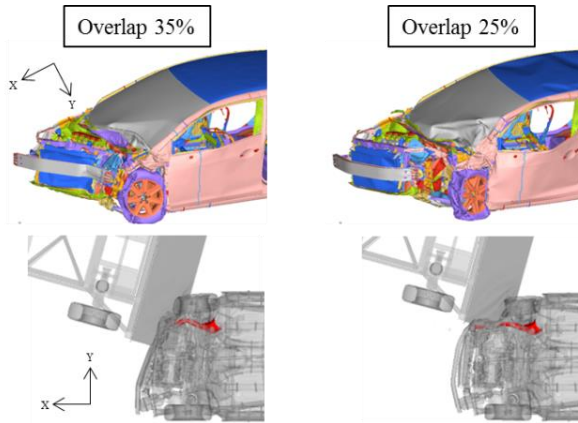
**Figure1. Test configuration of Oblique**

Figure 2 shows the results from confirmation of the vehicle body deformation, the movement of the human body model, and the number of bones fractured. A distinctive feature of chest injuries in actual small overlap and oblique frontal crash accidents was fractures on the non-belted side (left side) caused by collision with the door trim. However, collision with the door trim did not occur in the vehicle used for verification. The result showed three fractures concentrated in the lower part of the ribcage at #10, #11, and #12 ribs on the left side. The injuries sustained here differed from the chest injuries that occurred in actual small overlap and oblique frontal crash accidents, where fractures occurred a particularly large number in ribs 1 to 10.

Vehicle body	Passenger	
Vehicle deformation at maximum displacement	Maximum excursion	Fractures site
		

**Figure2. CAE Result of vehicle deformation and passenger injury**

In the results obtained by Saunders et al.[8] confirming the reproducibility of Vehicle to Vehicle(VtV) and OMDBtV, configurations that provide high reproducibility of the toe pan were selected for the configuration of the oblique mode that is currently scheduled to be adopted. These are configurations that place an emphasis on evaluation of tibia injuries, which are numerous in small overlap and oblique frontal crashes. According to Saunders et al. [8], the interaction of longitudinal members of own vehicle and opponent vehicle also influences the A-pillar displacement and accompanying chest injuries. In the case of modes in which there is no engagement of longitudinal members with the opponent vehicle, they indicate a high degree of reproducibility in the A-pillar. In order to reproduce actual accidents resulting in chest injury, deformation of the vehicle body (particularly the A-pillar) needs to be made to more closely resemble what happens in actual accidents. With a view to reproduction of chest injury, therefore, which is the purpose of this verification, the overlap was changed from 35% to 25% so that this would not be a mode that is no engagement between longitudinal members. Other elements of the configuration are the same as shown above. Figure 3 shows the appearance of the vehicle body during the crash.



**Figure 3. Comparison of vehicle body deformation between overlap 35% and 25%**

The result of numerical simulation with the overlap changed to 25% resulted in a mode in which engagement with the outer side of the longitudinal members did not occur, and there was increased deformation of the upper portion of the A-pillar. Although the increased deformation of the A-pillar also tended to increase the deformation of the door, this did not occur to the extent that the occupant would collide with the door trim. Occupant collision with the door trim did not occur, and no change was seen in the number of fractures or fracture sites. Figure 4 shows the occupant movement and fracture sites.

Passenger movement		Fractures site	
Overlap 35%	Overlap 25%	Overlap 35%	Overlap 25%
		 3 Fractures	 3 Fractures

**Figure 4. Comparison of passenger movement and fracture sites between overlap 35% and 25%**

### Reproduction of accident situation

Among the causal factors in the collision of occupant and door trim are the amount of intrusion by the vehicle body and the occupant movement that accompanies vehicle body movement (lateral slide). These are considered to be important parameters. The capability of this mode to reproduce actual accidents was verified by taking three points as tuning parameters. These three points were that overlap was such that it would not depend on longitudinal members, that the angle was such that occupant movement that becomes an impact with the door trim was reproduced, and that the level of kinetic energy (speed) was such as to result in a collision. In order to calculate the configuration for an OMDB, VtV computer simulation was first used to verify that this mode would reproduce the injuries sustained in actual accidents. A 2 ton class SUV was used as a vehicle with a weight ratio to the passenger car of 1:1.6. Figure 5 shows a graph of the estimated number of accidents according to the own vehicle/opponent vehicle weight ratio, as obtained from NASS-CDS accident data (1320 cases from 2000 to 2013). Based on this graph, the ratio of 1:1.6 is positioned to include more or less the entire range of accidents that occur(99%). Next, for the purpose of configuring the speed, Fig. 6 shows the barrier equivalent velocity (BEV) on the horizontal axis and the estimated number of actual accidents on the vertical axis on the left. The average AIS value in the speed range of those accidents is shown on the vertical axis on the right. It is apparent from Fig. 6 that the average extent of injury increases abruptly in the 60-70 km/h speed range, rising to around 4 or less on the Maximum Abbreviated Injury Scale (MAIS). Since an injury rated as AIS4+ is severe, efforts were directed to this region in order to reduce fatalities and injuries. When a BEV of 60-70 km/h is expressed as  $\Delta V$ , it is the equivalent of approximately 80 km/h.

According to the NHTSA accident study results, this covers 80% of the range of speeds that involve fatal accidents.[1].

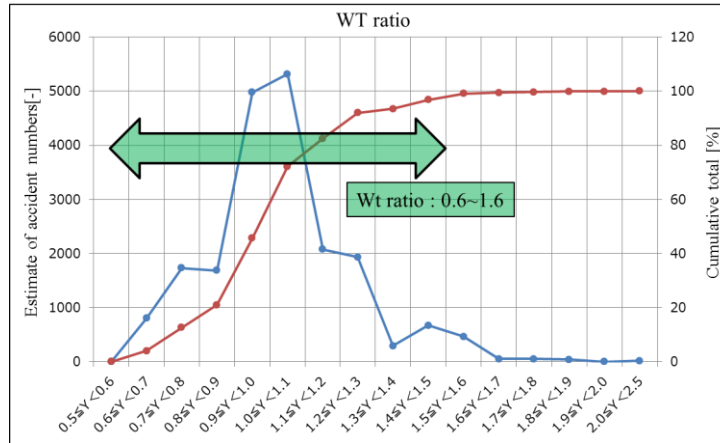


Figure5. The number of accidents by Wt ratio (Opponent vehicle/Own vehicle) in US

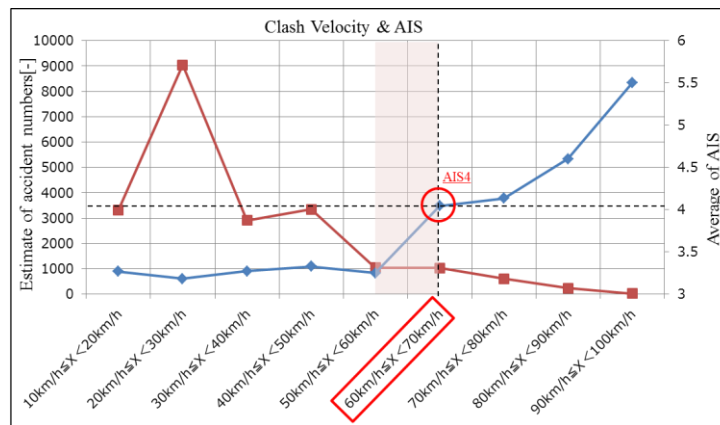


Figure6. The number of accidents and AIS average by BEV

Since the angle results in occupant movement in the direction of the door, the angle was changed from the 15° chosen for the oblique test to 30° with the aim of having the occupant move into a region where the occupant cannot be protected by the driver (DR) air bag that is intended for a conventional frontal crash. The overlap was set to 25% so as to avoid interference by longitudinal members. Figure 7 shows the configuration.

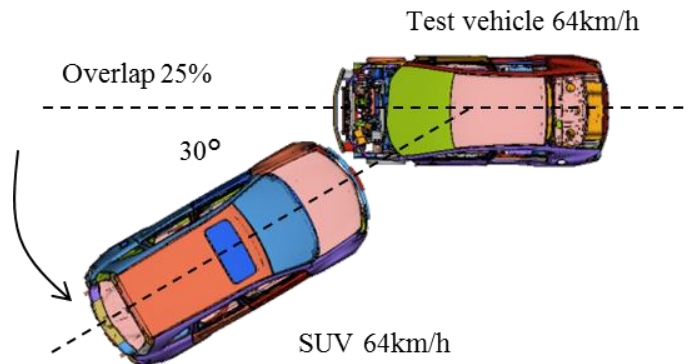
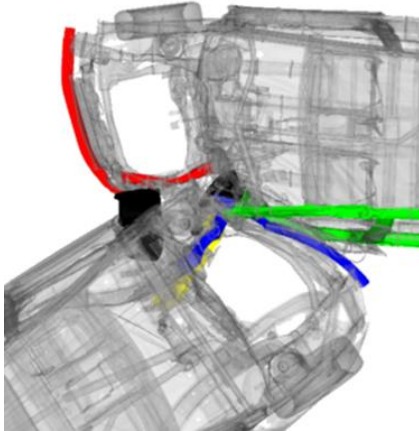
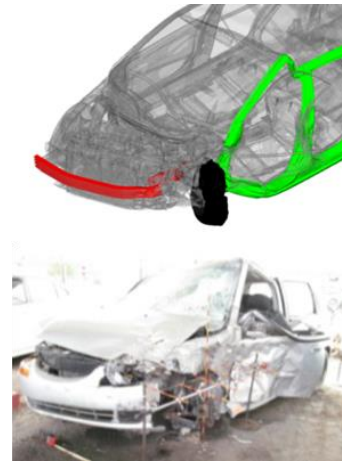


Figure7. Test configuration of VtV

Figure 8 shows the appearance of vehicle body deformation obtained through computer simulation. No engagement between longitudinal members occurred, and the bumper beam of the large vehicle (SUV) therefore collided directly with the A-pillar portion of the test vehicle. Increasing deformation of the A-pillar was accompanied with increasing deformation of the door, so that the door intruded into the occupant compartment space. Figure 9 shows the similar category of vehicle body deformation obtained from NASS-CDS as an example of a small overlap and oblique frontal crash compared with CAE result. Energy could not be absorbed by longitudinal members, and the progressive interference of the opponent vehicle with the A-pillar portion increased the load on the occupant compartment so that the upper portion of the A-pillar became deformed. It is apparent that the deformation mode obtained by computer simulation closely resembles the mode of deformation that occurs in actual accidents.



*Figure 8. No engagement of the longitudinal structure*



*Figure 9. Comparison of CAE result and example of small overlap actual accident*

Next, in the interest of evaluating chest injury in small overlap and oblique frontal crashes, the deformation shown in VtV was reproduced using OMDB and the capability of reproducing the injury sustained by the occupant's chest in actual accidents was confirmed. In order to have the same vehicle body deformation mode, the overlap and angle were fixed and the speed parameter was tuned to conduct verification. Displacement equal to VtV was defined as the target, and X-Y deformation was confirmed using "toepan\_center," "toepan\_L," and "A-pillar" as judgment criteria. In order to confirm whether the injuries sustained in small overlap and oblique frontal crashes were successfully reproduced, the occupant contact location and number of fractures were confirmed. The speed of the vehicle crashed into was fixed at 0 km/h and confirmation was conducted in three levels with the OMDB crashed into the vehicle at 10-km/h increments from 90 km/h to 110 km/h. The point at which the computer simulation results were equal to or better than VtV for the OMDBtV at every deformation measurement point was when the OMDB was crashed at a speed of 110 km/h. Figure 10 shows the deformation and occupant movement that the OMDB was crashed at a speed of 110 km/h. Unlike VtV, the mode of large vehicle bumper beam directly impacting the A-pillar could not be reproduced with the OMDB. In the course of proceeding until A-pillar deformation was equal, therefore, the displacement in other regions tended to be greater than in VtV. Occupant movement was the aim of the 30° angle, and the direction was into an area not protected by the front air bag and in the direction of the door, where it coincided with the direction of intrusion by the door so that the chest came in contact with the door trim. This collision resulted in fractures of the ribs, and the result was that the contact sites and number of fractures were the same as the results given for actual accidents. This successfully indicated the possibility that evaluation of chest injury in small overlap and oblique frontal crashes using OMDB could yield the same phenomena as injuries sustained in actual accidents when the OMDB was crashed into the test vehicle at a speed of 110 km/h, an overlap of 25%, and an angle of 30° in the Small Overlap & Oblique (SOO) configuration.



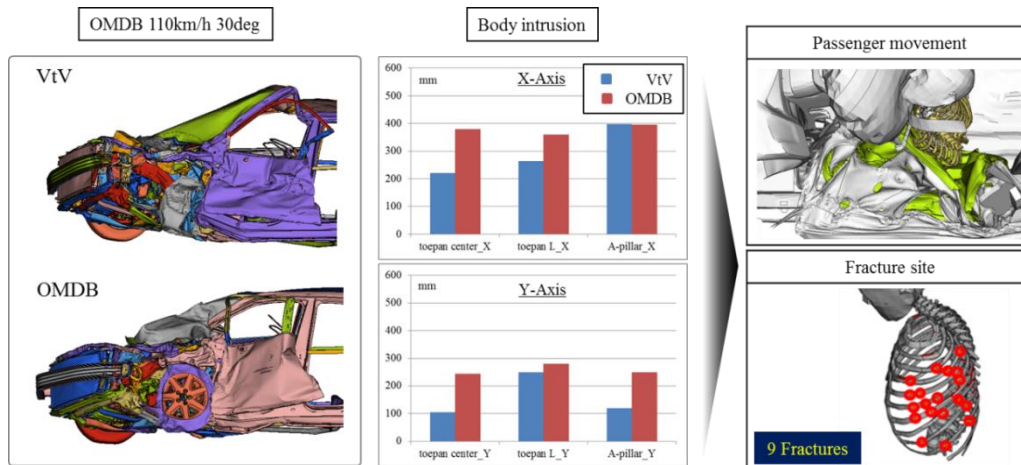


**Figure10. VtV and OMDBtV Comparison**

**Comparison of Oblique test and SOO mode**

A comparison of SOO mode and oblique mode was made using the vehicle that was tested for the present research. Figure 11 shows the various mode configurations.

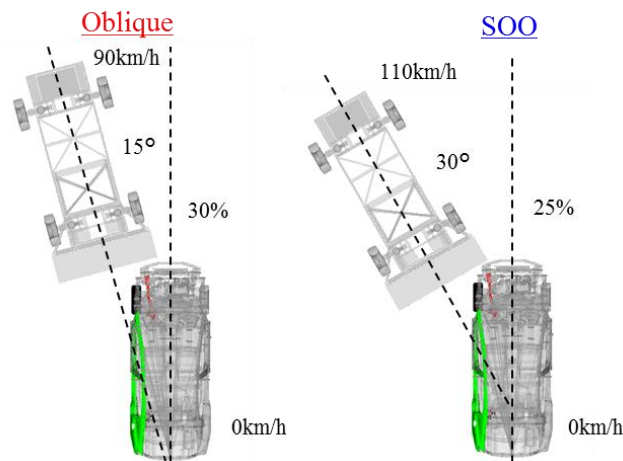


**Figure11. Test configurations of Oblique test and NEW vehicle test**

The comparison was made in terms of the evaluation vehicle  $\Delta V$ , which indicates the severity to the occupant. Figure 12 shows  $\Delta V$  of SOO mode and oblique mode. In oblique mode, the evaluation vehicle  $\Delta V$  was 64 km/h, while in the SOO mode indicated in the present research, the  $\Delta V$  was 78 km/h, which places the occupant in a severe situation. However, it was confirmed that  $\Delta V$  corresponding to 80 km/h was achieved, which was the target, given that the purpose of the present research was to reduce fatalities and injuries. Comparison was then made of deformation in each area of the vehicle body. The comparison was made using the STRUCTURE index defined by IIHS as a reference index for the purpose of the comparison. Figure 13 shows the results of deformation at the measurement points where IIHS evaluation is performed[9].

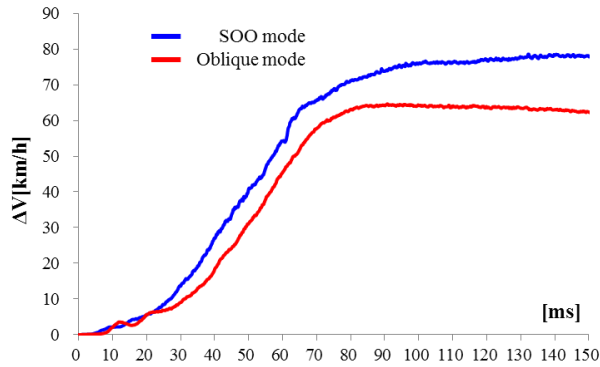


Figure12. ΔV of SOO mode and oblique mode

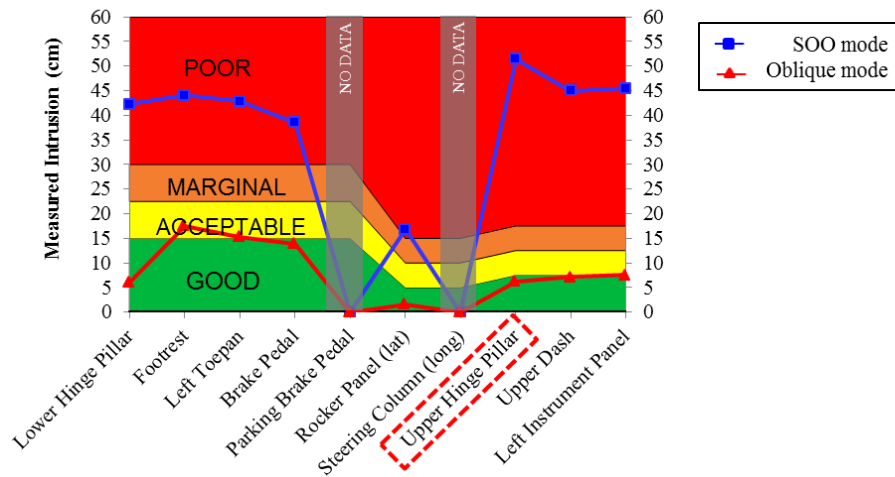


Figure13. Occupant compartment intrusion (IIHS evaluation)

Deformation tended to increase significantly in SOO mode in all regions. Deformation of the A-pillar was particularly conspicuous, and there was an increase of 45 cm in the upper portion of the A-pillar relative to the oblique mode. The contribution of the angle, speed, and overlap parameters was confirmed assuming that the deformation of 45cm was 100%. It was found that changing the angle from 15° to 30° produced 24% of the total increase, changing the speed from 90 km/h to 110 km/h produced 57% of it, and changing the overlap from 35% to 25% produced 19% of the increase in deformation. The increase in deformation due to speed was the result of the increase in input energy. In the case of overlap, energy absorption by longitudinal members did not take place, and the resulting increase in load on the occupant compartment caused the increase in deformation. The causal factors in the increased deformation due to the angle were examined in terms of the appearance of intrusion shown in Fig. 14.

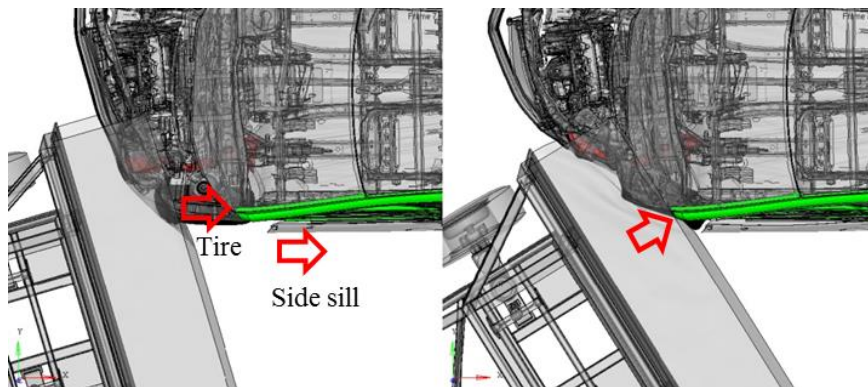
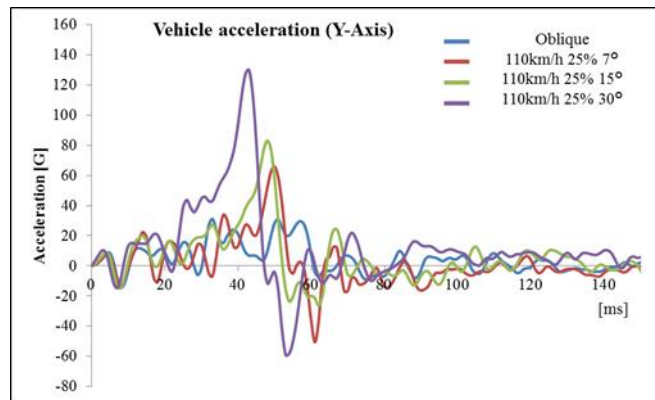


Figure14. Comparison of Oblique test(left) and SOO test(right)

In oblique mode, the angle is shallower than in SOO mode so that the load is distributed through the tire to the side sill. It is apparent that in the NEW mode, however, the tire is turned over on its side so that the load is not transmitted to the side sill, and instead the honeycomb portion of the OMDB impacts directly against an A-pillar portion. When the angle is deeper, the distribution of load toward the rear of the vehicle body is reduced, and the extent to which a load path is not formed is the extent of increase in deformation. Figure 15 shows vehicle body acceleration in the Y direction when numerical simulation of the oblique mode is performed with the speed fixed at 110 km/h and the angle set variously to 7°, 15°, and 30°. In light of the timing of the OMDB honeycomb contact with the A-pillar portion, there is an increase of acceleration in the Y-axis direction and the vehicle body movement shifts in the Y direction. This increase in acceleration is accompanied by occupant movement in the direction of the door, which is a movement counter to the vehicle. These results show that setting the angle at 30° causes acceleration in the Y direction to increase suddenly. This is further indication of the need for a crash angle that can cause the tire to turn over on its side and induce direct impact against the A-pillar. Since collision by the occupant with the door trim occurs at this angle, 30° appears to be appropriate.



*Figure15.Comparison of vehicle acceleration(Y) according to crash angle*

### Evaluation of SOO mode for SOT GOOD model

Up to this point, verification has been conducted using an 11M small passenger car. Research was continued using a midsize passenger car, which received a GOOD evaluation in the SOT implemented by IIHS in 2018, to confirm how the small overlap and oblique frontal crash is positioned with regard to chest injury. Although it is according to in-house data, the vehicle body in this model yielded vehicle body deformation at a level that was GOOD in terms of the SOT index even in oblique mode. Computer simulation was carried out with the configuration of 25% overlap, 30° angle, and 110 km/h speed that has been verified up to this point. Figures 16 and 17 show comparisons of the deformation and the appearance of the deformation produced with that configuration. By comparison with the SOT and oblique test configurations, the SOO configuration showed an overall tendency toward increased deformation. This was especially conspicuous in the A-pillar portion where there was a tendency to increase to the level rated POOR in the IIHS index. The reason for this was the same as in the verification performed using the 11M small passenger car, which is that the tire was turned over on its side and the OMDB honeycomb impacted directly against the A-pillar. It was found from these results that in the SOT that is presently adopted as well as in the oblique mode that is scheduled to be adopted, there is a possibility that vehicle body performance is inadequate with respect to chest injury even in a vehicle body that has the highest ranking of self-protection performance. In other words, the possibility that chest injury caused by contact of the chest with the door trim may not be comprehensively avoidable became clear. In order to pursue reduction of chest injuries and reduction of fatalities and injuries, it would be necessary to implement evaluation in SOO mode that reproduces actual accident circumstances and proceed to devise countermeasures.

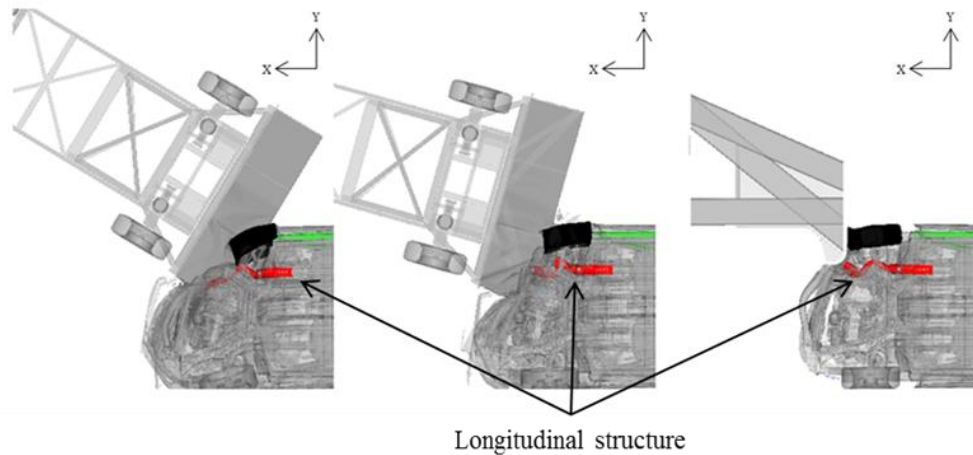


**Figure16. Deformation of longitudinal structure (left:SOO,Center:Oblique,Right:SOT)**

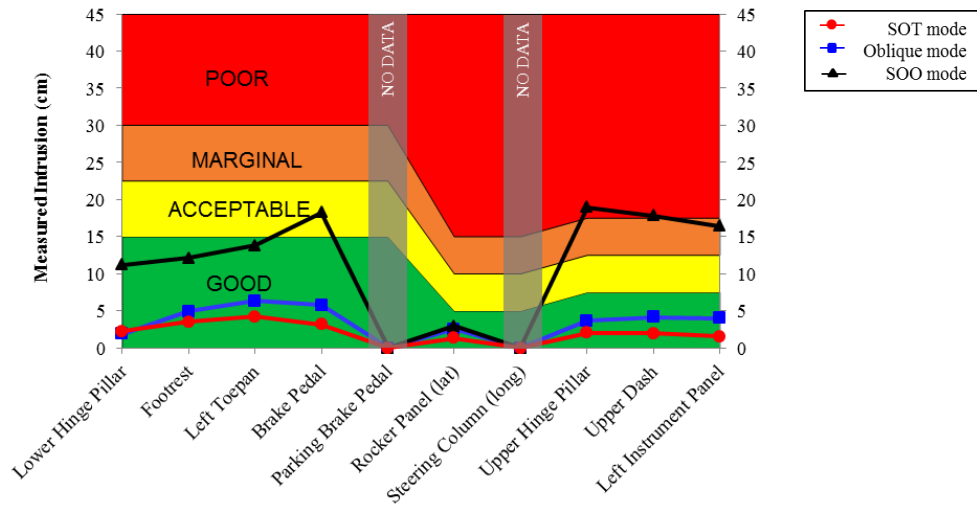


**Figure17. Comparison of occupant compartment intrusion**

**Reduction of chest injury in small overlap and oblique frontal crashes**

**Body strengthening** In investigating approaches to countermeasures, verification was first implemented for countermeasures on the vehicle body side intended to reduce vehicle body deformation. Taking the 11M small passenger car as a baseline, the thickness was changed at five places on members that contribute significantly to vehicle body deformation. For all five parts, the thickness was increased in increments of one rank (RNK) of 0.2 mm each. The OMDB was then crashed into the 11M small passenger car in SOO configuration and computer simulation was performed. Figure 18 shows the vehicle body strengthening areas and a plot of the maximum displacement of the A-pillar portion. As noted above, the 18 M midsize passenger car has the newest vehicle body performance and is positioned at the IIHS GOOD level. The deformation to this 18M midsize passenger car is plotted on the right of the figure. The deformation that occurred at strengthening to the fourth rank (4RANK) showed the same extent of intrusion into the vehicle body as in the 18M midsize passenger car. When further strengthening was applied to raise this to the seventh rank (7RANK) above the BASE, confirmation of occupant movement and occurrence or otherwise of fractures showed that contact with the door was still occurring and fracture injuries were found. Figure 19 shows the fracture status of the respective occupants. The movement of the

respective occupants in the Y direction counter to the vehicle movement is shown in Fig. 18. Although doing such strengthening is not a realistic possibility in terms of the marketability of the vehicle body, even if the rigidity of the vehicle body were to be increased to the point of making it so rigid that the vehicle framework did not undergo any deformation at all, then the vehicle body would rotate by an amount that is in inverse proportion to the decrease in intrusion. It was confirmed that the movement of the occupant in the Y direction would therefore increase, and contact with the door could not be avoided. Although the number of fractures decreased, this resulted in a total of six fractures in ribs 5 to 11, with the lateral load input causing the fractures being concentrated in the ribs on the left side and to the rear from the very left. These fractures are reason for concern about injury to internal organs. It was confirmed, therefore, that there is a limit to countermeasures consisting of increased strengthening of the vehicle body against small overlap and oblique frontal crashes.

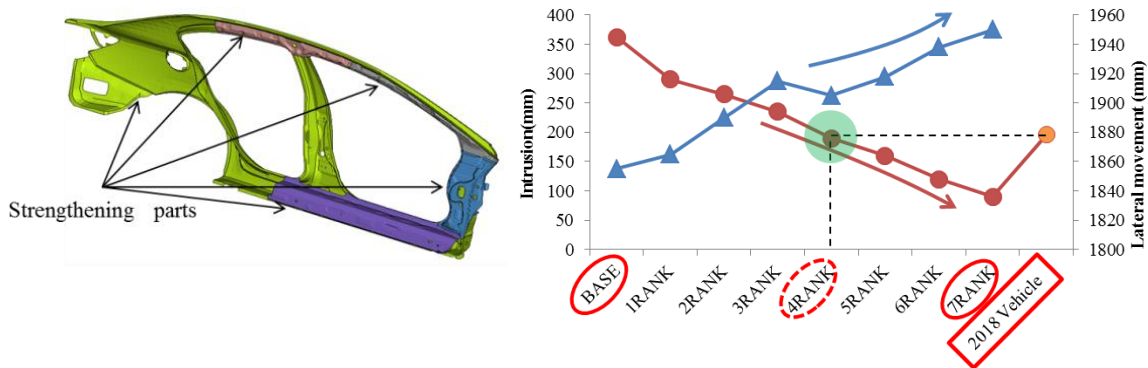


**Figure18. Occupant compartment intrusion and occupant movement to lateral direction by body strengthening(left:strengthened parts)**

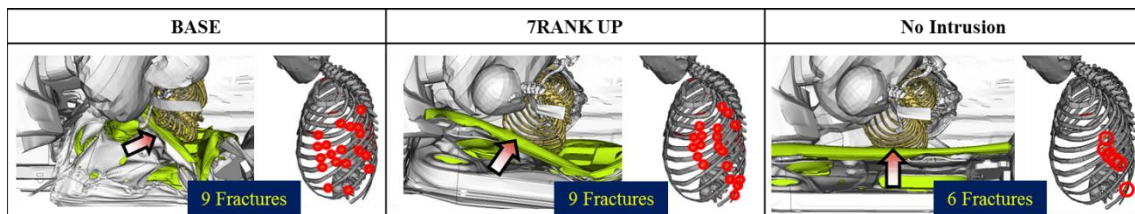


**Figure19.Effect of body strengthening on occupant**

**Restraint device** Verification of the possibility of countermeasures using restraint devices was carried out next. The area that the chest comes in contact with in small overlap and oblique frontal crashes is a blind spot in the area protected by conventional driver (DR) air bag and side air bag. Conceivable methods for addressing this are enlarging the side air bag and enlarging the curtain air bag. The purpose here, however, was to confirm effectiveness against fractures of the ribs. For the present research, therefore, a simple check was made to confirm the magnitude of the effect from installing a side air bag in the door front (FR) portion. Figure 20 shows a conceptual image of the installation and air bag deployment. Figure 21 shows the chest fractures of the computer simulation results. Where nine fractures occurred when there were no air bag in place, adding the air bag resulted in eight fractures, not significantly reducing the number of fractures. However, a check of the way the chest deflection when the fractures occurred showed that in the BASE configuration, the chest crashing against the hard structure of the door caused a load to be applied from the outside toward the internal organs locally so that the ribs were bent in toward the inside of the body. Adding the air bag changed the direction in which the ribs were bent to the opposite direction, away from the internal organs. In the former, there is a high possibility that the fracture end damages the internal organs.



This showed the possibility that the use of the air bag may mitigate the load input locally as well as the extent of injury. The effect of not taking countermeasures on the vehicle body side was confirmed as part of the present research, but for the future, it will be necessary to reduce the number of fractures by adding restraint devices that have been optimized for the characteristics of the air bag, thereby securing a survivable space by combining this approach with vehicle body countermeasures.

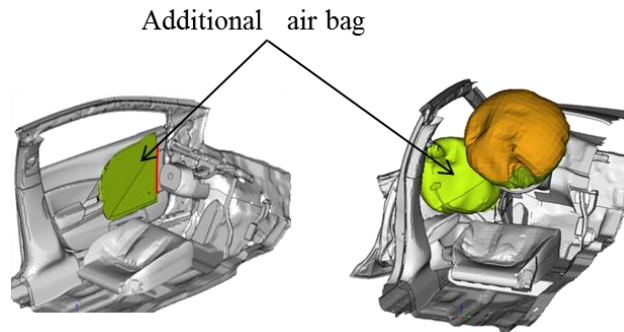


*Figure20. Energy absorbing parts for oblique*

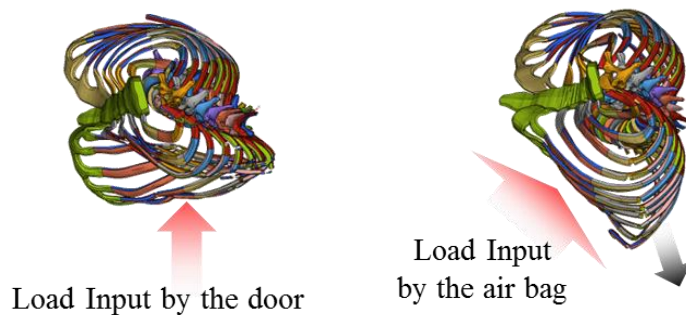


*Figure21. Effect of restraint device on occupant(Left:BASE,Right:With air bag)*

## DISCUSSION

Taking the view that, for the purpose of reducing fatalities and injuries, it would be necessary to establish evaluation methods that conform to actual accident circumstances, the present research focused on chest injuries during small overlap and oblique frontal crashes and sought modes that would recreate those injuries. With a view to achieving evaluation, configurations using the OMDB were calculated. The modes described above are quite severe when viewed from the perspective of  $\Delta V$  in existing evaluation test configurations. However, the reason for this is that the present research has the purpose of concentrating attention on chest injuries in order to reduce further fatalities and injuries. According to the computer simulation, performing verification with severe configurations (weight, speed, angle) that systematically include actual accidents has made it possible to identify mechanisms of chest injury in actual small overlap and oblique frontal crash accidents.

The examination of countermeasures against chest injuries in small overlap and oblique frontal crashes has clarified directions for future countermeasures. There are limits to the reduction in injuries that can be achieved by strengthening the vehicle body, and it will be necessary for countermeasures that go beyond the conventional front and side restraint devices to include combinations with airbags for use in oblique crashes. This indicated the possibility that measures against chest injury may be inadequate even if vehicle body performance supports SOT, including the oblique mode that is currently scheduled to be adopted. Further advances are called for in vehicle body and restraint devices. For that purpose, however, achieving widespread adoption of restraint devices in the necessary areas will be a challenge as long as there is no evaluation of modes involving collision with the chest. The present

research has not gone beyond verification using two passenger cars, which are small and midsize vehicles, and this does not suffice for proposing a complete evaluation method. For the future, it will be necessary to establish an evaluation method with the chest injury perspective. The research that will be needed for that purpose extends beyond the verification of test modes in the present research that conform to actual accident circumstances by the use of a human body model. It will be necessary to conduct future examination of the possibility of using the THOR anthropomorphic test devices (ATD) for appropriate measurement and evaluation of the characteristic displacement in the Y direction that is found in small overlap and oblique frontal crashes.

## CONCLUSION

The present research used computer simulation to identify configurations that reproduce chest injuries from actual small overlap and oblique frontal crash accident circumstances.

- Overlap (LAP) 25%: This mode does not depend on energy absorption by longitudinal members.
- Angle 30°: This angle enables reproduction of occupant movement.
- Speed 110 km/h: The crash energy at this speed results in collision between the occupant and the cabin.

It was confirmed that by tuning the above three points, it was possible to reproduce the collision between chest and door trim that is a distinctive characteristic of chest injury under actual accident circumstances. These injuries were also subjected to numerical simulation using a human body model, and by this means the effectiveness of countermeasures utilizing the vehicle body and restraint devices was confirmed. This indicated that countermeasures that only strengthen the vehicle body have their limits, so that a combination with countermeasures utilizing restraint devices is needed.

## REFERENCES

- [1] NHTSA, "Fatalities in Frontal Crashes Despite Seat Belts and Air Bags", 2009
- [2] Rodney W. Rudd, Mark Scarboro, James Saunders, "INJURY ANALYSIS OF REAL-WORLD SMALL OVERLAP AND OBLIQUE FRONTAL CRASHES", 2011 ESV, Paper Number 11-0384
- [3] Johan Iraeus, Sofie Wistrand, Bengt Pipkorn, "Evaluation of Chest Injury Mechanisms in Nearside Oblique Frontal Impacts", 2013
- [4] Mats O. Lindquist, MSc, Andrew R. Hall, BEng, and Ulf L. Björnstig, MD, PhD, "Kinematics of belted fatalities in Frontal Collisions: A New Approach in Deep Studies of Injury Mechanisms", 2006 J Trauma, 61:1506-1516
- [5] Matthew L. Brumbelow, Charles M. Farmer, "Real-World Injury Patterns Associated With Hybrid III Sternal Deflections in Frontal Crash Tests", Traffic Injury Prevention, 2013, 14:807-815
- [6] Osamu Ito, Yasuhiro Dokko, Kazuki Ohashi, "Development of Adult and Elderly FE Thorax Skeletal Models", 2009 SAE, No2009-01-0381
- [7] NHTSA, "LABORATORY TEST PROCEDURE FOR OBLIQUE OFFSET MOVING DEFORMABLE BARRIER IMPACT TEST", 2015, Docket NHTSA-2015-0119
- [8] James Saunders, Matthew J. Craig, Jeffrey Suway, "NHTSA'S TEST PROCEDURE EVALUATIONS FOR SMALL OVERLAP/OBLIQUE CRASHES", 2011 ESV, Paper Number: 11-0343
- [9] IIHS, "Small Overlap Frontal Crashworthiness Evaluation Crash Test Protocol (Version VI)", 2017,



# **OPTIMIZATION OF FRONT END STRUCTURES FOR IIHS SMALL OVERLAP FRONTAL CRASH TEST**

**Guofei Chen and Ming F. Shi**

United States Steel Corporation  
USA

**Tau Tyan**

Ford Motor Company  
USA

Paper Number 19-0188

## **ABSTRACT**

The Insurance Institute for Highway Safety (IIHS) introduced a small overlap rigid barrier (SORB) crash test in 2012. In the IIHS SORB tests, the rigid barrier primarily impacts a vehicle's outer edges instead of the main longitudinal structures traditionally designed to absorb frontal impact energy. Due to the test condition, the front wheels are often forced to move rearward and into the footwell, contributing to significant and localized intrusion in the occupant compartment. To investigate the design countermeasures for such a severe test mode, the full vehicle model developed in the final phase of the Future Steel Vehicle (FSV) program by WorldAutoSteel was adopted as a baseline. In this study, innovative countermeasure design concepts for the front end structures, especially bumper beam, shotgun, front rail, A-pillar, hinge pillar, and rocker, were proposed and optimized with the FSV full vehicle model. The optimized designs helped the vehicle slide away from the small overlap rigid barrier and converted more impact energy to vehicle kinetic energy. When used together with ultra high strength steel (UHSS), the intrusion into the occupant compartment was reduced and the overall structural rating was improved from "Marginal" to "Good" in the SORB test. In the meantime, the design concepts reduced intrusion in the IIHS 40% overlap deformable barrier (ODB) test and maintained a similar crash pulse in the US-NCAP full frontal crash test. The potential mass reduction opportunity with the design concepts and UHSS was also evaluated.

## **INTRODUCTION**

Over the last several decades, tremendous progress in vehicle frontal crash performance has been achieved. The automotive community has made considerable efforts in developing optimized crumple zone structures with higher strength materials such as advanced high strength steels (AHSS) to absorb the crash energy.

In 2012, the IIHS released the more demanding frontal offset test named the small overlap rigid barrier (SORB) crash test [1, 2]. The new test, which is used in addition to the 40% overlap deformable barrier (ODB) test introduced in 1995, subjects only 25% of the front end of the vehicle to a 64.4 km/hr (40 mph) impact into a 1524-mm-tall (5 feet) rigid barrier. The new test is far more demanding on the vehicle structures than the 40% ODB test. What makes the small overlap crash test so challenging is that the outer front wheel receives the impact forces first rather than the more central crash absorbing structures such as the longitudinal structural members. The crash forces are concentrated on the front suspension, the firewall, the hinge pillar and the base of the A-pillar, which are not traditionally designed to absorb and dissipate crash forces in a front impact.

The vehicle performance in the IIHS small overlap frontal crash test is rated based on three categories: restraints and dummy kinematics, dummy injury measures, and vehicle structural performance [3]. Since the release of the IIHS SORB crash test protocol, the IIHS has evaluated numerous midsize and small cars, with few vehicles earning the top rating of good, particularly due to the structural performance rating. Most of the vehicles on the road in 2012 could not meet the targets for a 'good' rating in this test and all vehicle manufacturers started incorporating countermeasures to improve SORB performance [4].

The advancement in computer optimization technologies and the availability in higher strength of AHSS in GigaPascal-strength levels provide opportunities to develop countermeasure designs to improve the overall

structural rating in the SORB crash test. In this study, a full vehicle finite element model was utilized in the SORB crash test simulation to identify the critical components contributing to the performance in the SORB crash event. Innovative countermeasure design concepts with ultra high strength steels (UHSS) were developed and optimized for the front end structures, especially bumper beam, shotgun, front rail, A-pillar, hinge pillar, and rocker. The potential vehicle weight reduction opportunity with the optimized design concepts and UHSS was also evaluated.

## **SORB CRASH SIMULATION MODEL**

The full vehicle finite element model developed in the final phase of the Future Steel Vehicle (FSV) program [4] by WorldAutoSteel in 2011 was adopted as the baseline in this study, as shown in Figure 1. The FSV features optimized AHSS body structure designs that reduce mass by more than 35 percent over a baseline ICE body structure adjusted for a battery electric powertrain. More than 20 new AHSS grades, representing materials expected to be commercially available in the 2015 – 2020 technology horizon, are applied in the FSV final concept designs. The material portfolio includes dual phase (DP), transformation-induced plasticity (TRIP), twinning-induced plasticity (TWIP), complex phase (CP) and hot formed (HF) steels, which are the newest in steel technology offered by the global industry. The FSV uses 97 percent HSS and AHSS with nearly 50 percent of the steels at GigaPascal-strength levels.

The FSV front end structures feature:

- A front rail sub-system with the optimized section shape of the rails that improved crash energy management while reducing mass. It was manufactured using a laser welded blank with varying gauges of TRIP material.
- A shotgun sub-system resembling a shotgun-type rifle that provided enhanced performance in both full frontal and offset crash simulations. The shot gun was designed with a three-piece hot formed steel tailor welded blank of varying thicknesses.

The FSV final concept designs met a broad list of global crash and durability requirements, including the US-NCAP and the IIHS 40% ODB frontal crash criteria. Since FSV was developed before the SORB crash test was introduced in 2012, the SORB crash test was not considered in the FSV program.

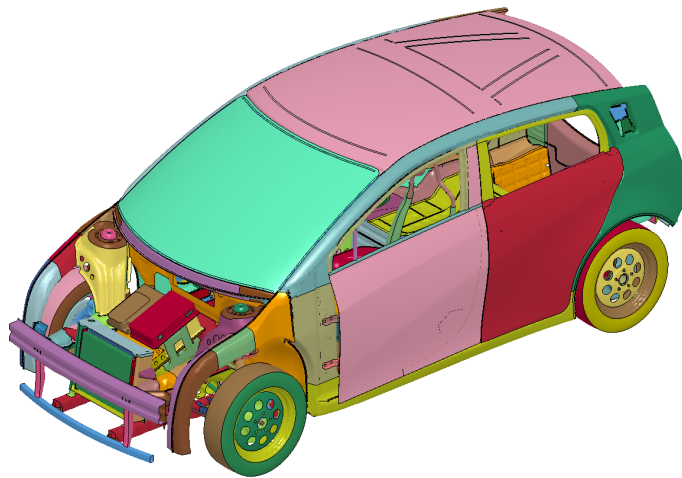


*Figure 1. FSV full vehicle finite element model*

In this study, the crash simulation model for the SORB test was developed using the FSV final concept design as the baseline, as shown in Figure 2. The vehicle was aligned with a rigid barrier such that the right edge of the barrier face is offset to the left of the vehicle centerline by 25 percent of the vehicle's width [2]. The vehicle crashed into the 1524-mm-tall (5 feet) rigid barrier at 64.4 km/hr (40 mph) speed.

The structural rating is based on intrusion measurements on selected points at the lower occupant compartment and the upper occupant compartment [2, 3]. The lower occupant compartment points include the lower hinge pillar, footrest, left toepan, brake pedal, parking brake pedal, and rocker panel measurements. The upper occupant compartment points include the steering column, upper hinge pillar, upper dash, and left instrument panel. The intrusion measurements for the FSV in the SORB crash simulation are shown in Figure 3. The subrating for the lower occupant compartment is “Good” and the subrating for the upper occupant compartment is “Marginal”, therefore the overall structural rating for the FSV is “Marginal” in the SORB crash test.

Table 1 lists the top seven components in crash energy absorption in the SORB crash test along with the steel grades and gauges used in the FSV baseline design. As the front rail crash tip is located outside of the rigid barrier, the shotgun becomes the most important component to engage with the barrier and absorb the crash energy. Other critical components include the front rail rear, rocker, wheel rim, hinge pillar and A-pillar when the front wheel is forced to move rearward and crash into the footwell of the occupant compartment. The bumper beam absorbed less crash energy than those of other components because the bumper beam in the FSV design is short and located at the arc portion of the rigid barrier. The bumper beam immediately slid away from the barrier in the SORB crash test, resulting in reduced crash energy absorption. However, as the first structural member to engage with the crash barrier, the importance of the bumper beam should not be underestimated. A sensitivity study was conducted on the bumper beam length effect. Figure 3 shows that the intrusion into the occupant compartment decreased when the bumper beam was extended outward to align with the body width. The extended bumper beam enlarged the impact zone to help absorb more impact energy and increase vehicle lateral movement.

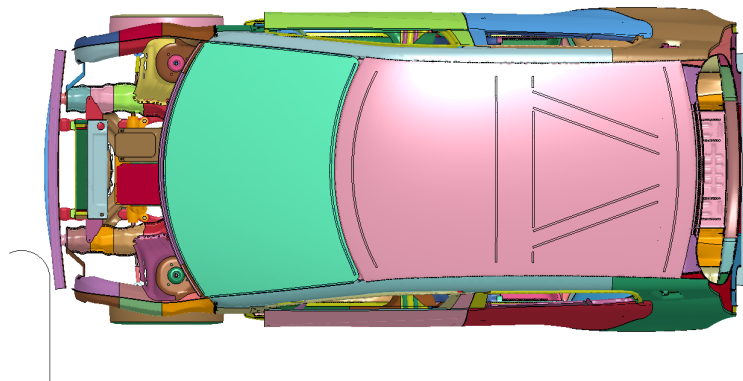


Figure 2. FSV crash simulation model for the SORB test – top view

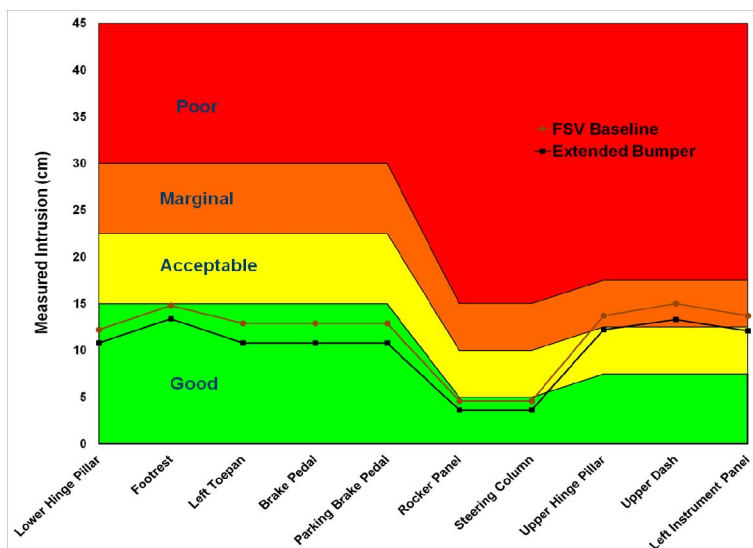


Figure 3. The effect of bumper beam extension in the SORB crash test

**Table 1.**  
**Top components in SORB crash energy absorption**

Part Name	Material	Gauge (mm)	Energy Absorbed (kJ)	Percentage (%)
Shotgun	HF1550	1.0/1.2/1.5	17.80	11.41
Front Rail	TRIP980	1.8/2.0/1.9/1.8	9.00	5.77
Rocker	CP1470	1.0	8.85	5.67
Wheel Rim	HSLA350	2.0	7.56	4.85
Hinge Pillar	DP780	1.2	6.55	4.20
A-Pillar	HF1550	0.7	5.64	3.62
Bumper Beam	DP780	1.0	3.46	2.22

## DESIGN OPTIMIZATION FOR THE SORB

In this study, the bumper beam, shotgun, front rail, A-pillar, hinge pillar, and rocker were selected in the design optimization, including geometry, gauge and steel grade optimization. Before the geometry optimization, the FSV front end structures were modified. The bumper beam was extended outward and the shotgun was extended forward into the extended bumper beam. Then, the shot gun was connected with the front face of the extended bumper beam by bolt joints or spot welds to strengthen the front end side structures so that both the shot gun and the bumper beam can engage with the barrier earlier during the initial impact. As a result, the impact loads could be distributed to the upper and lower body structures. In addition, more impact loads could be transferred to the non-impact side than a traditional design with only the front rails connected to the bumper beam.

The shape variables in the geometry optimization include the extension length of the bumper beam and the transition shape of the shotgun from the body side to the bumper beam. The objective of the optimization is to improve the overall SORB structural rating to “Good” from “Marginal” in the FSV baseline design without mass penalty. In the meantime, the baseline design is optimized to maintain or enhance crash performance in the IIHS 40% ODB and US-NCAP full frontal crash tests. HyperStudy® optimization software and LS-DYNA® nonlinear finite element software were utilized together for the geometry, gauge and steel grade optimization [5, 6].

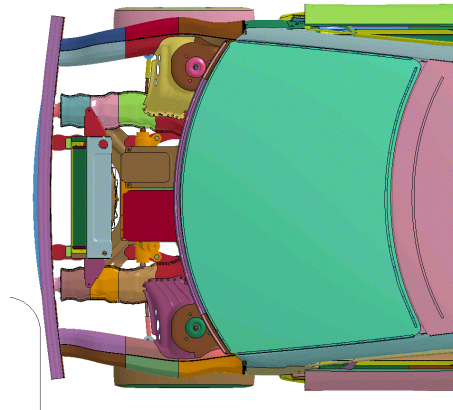


**Figure 4. Connection between the shot gun and the extended bumper beam**

## OPTIMIZED DESIGN CONCEPTS

An optimized design concept for the SORB crash test is shown in Figure 5. It features:

- An extended bumper beam at both ends. The bumper beam was extended as far as possible to align with the body width. The extended bumper beam would enlarge the impact zone to help absorb more crash energy and increase vehicle lateral movement.
- A new connection between the shotgun and the front face of the extended bumper beam. The system with the bumper beam integrated both the shotgun and front rail would strengthen the front end side structures,

engage the shotgun with barriers earlier, distribute impact load to upper and lower body structures, and transfer more impact load to the non-impact side than traditional design with only front rails connected to the bumper beam.

- A shape optimized shotgun with a “snake-shaped” transition from the body side to the corner of the rigid barrier. The optimized shape of the shotgun would increase the vehicle lateral movement by helping the vehicle slide away from the barrier and converting the impact energy to the vehicle kinetic energy. Figure 6 shows the comparison of vehicle lateral movement of the optimized new design with the FSV baseline in the SORB crash test.

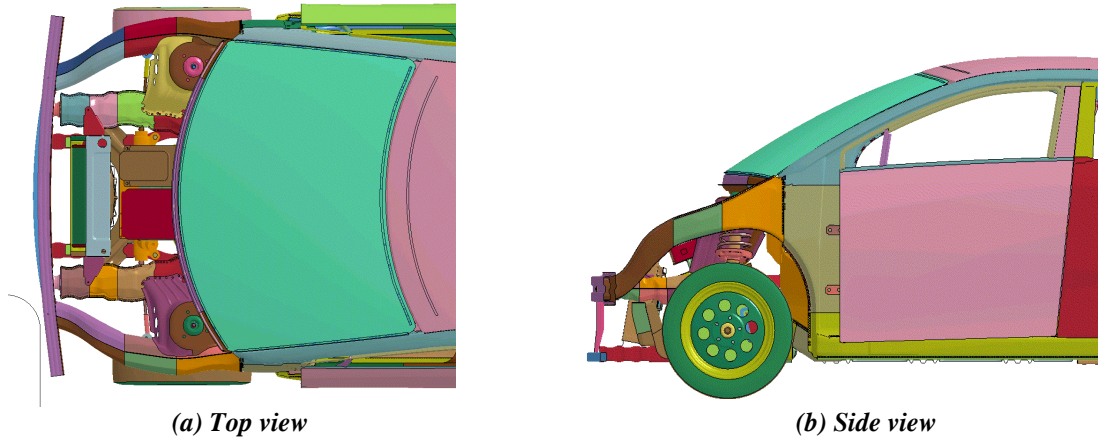


Figure 5. An optimized design concept for the SORB crash test

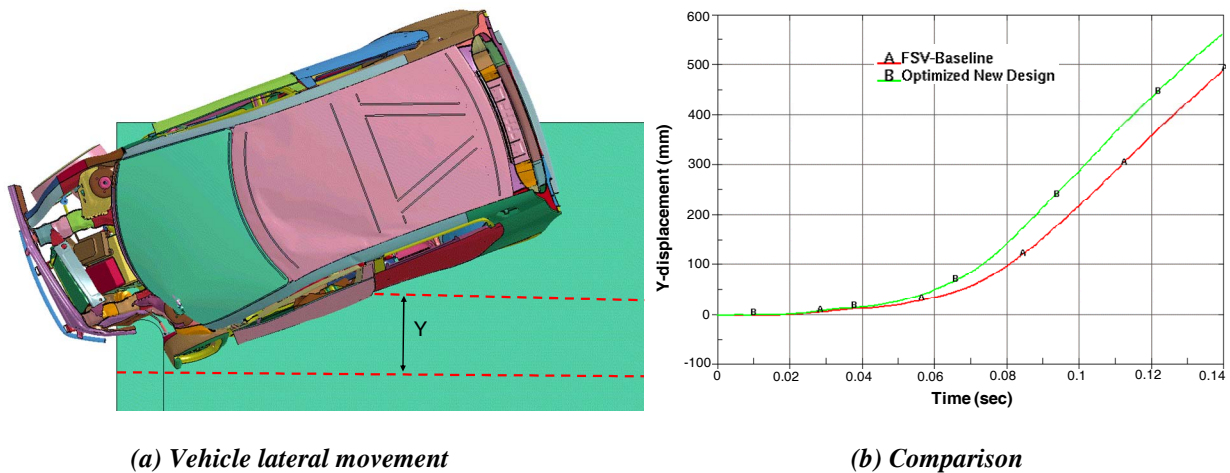


Figure 6. Comparison of vehicle lateral movement in the SORB test

Figures 7 and 8 show the comparison in the vehicle deformation and intrusion into the occupant compartment from the SORB test, respectively. Since the optimized new design helped the vehicle slide away from the SORB, less deformation was observed at the shotgun, hinge-pillar, rocker, roof rail and tire in the optimized new design. As a result, the intrusion into the occupant compartment was reduced, and the overall SORB structural rating was improved to “Good” from “Marginal” in the FSV baseline design.

The optimized shotgun and bumper beam also helped transfer the impact force to the non-impact side and reduced deformation/intrusion on the impact side in the IIHS 40% ODB frontal crash test, as shown in Figure 9(a). The intrusion was improved further to a “Good” structural rating with a higher probability and confidence level.



As both the front rails and the shotgun are connected to the bumper beam, one concern is that the front-end structures may be too stiff and can deteriorate the vehicle crash performance such as the deceleration pulse in the US-NCAP frontal crash test. Figure 9(b) shows the optimized new design had similar pulse responses in the NCAP full frontal test to that of the FSV baseline design, allowing similar occupant responses. This was achieved by slightly reducing the gauges of the front rails, as shown in Table 2, to balance the stiffness of the front rails and the shotgun as both of them were connected to the bumper beam.

Table 2 compares the materials, gauges and mass between the optimized new design and the FSV baseline design for some key components. More ultra high strength steels (UHSS) such as TRIP980 and HF1550 were used in the optimized new design. The total mass of the optimized new design remains similar to that of the FSV baseline with the intrusion reductions in both the IIHS SORB and the 40% ODB crash tests.

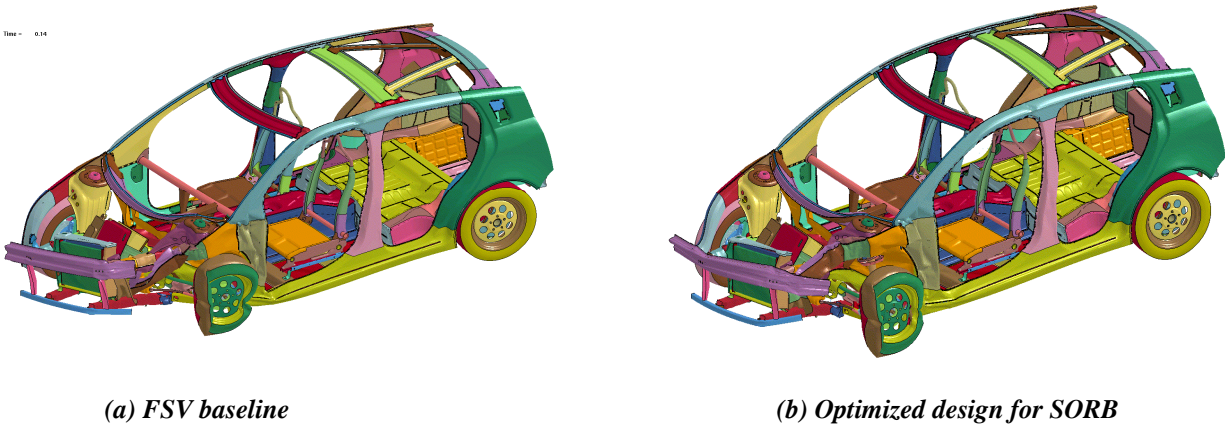


Figure 7. Comparison of vehicle deformation in the SORB test

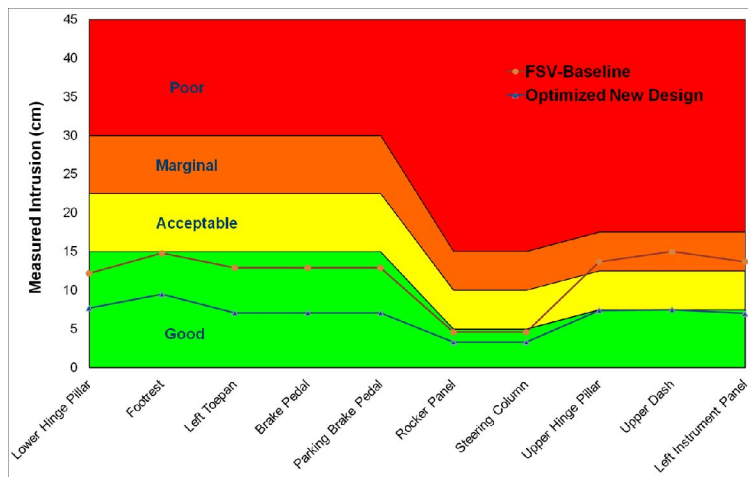
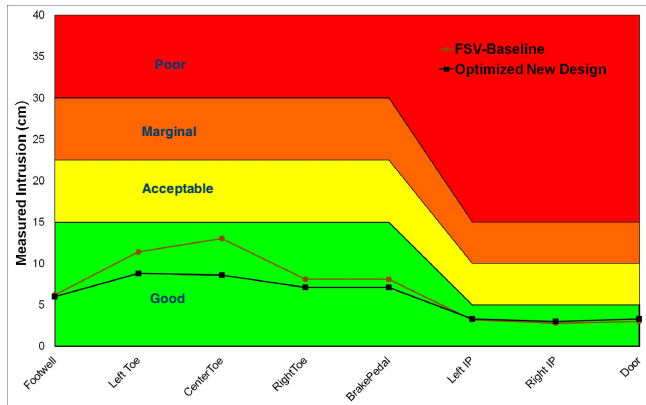
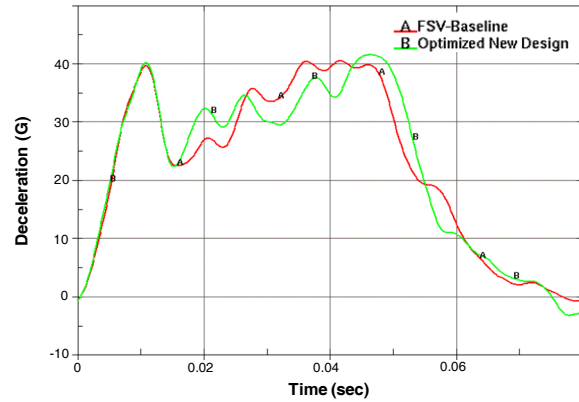


Figure 8. Comparison of intrusion in the SORB test



(a) IIHS 40% ODB



(b) US-NCAP

Figure 9. Comparison of crash performance in the IIHS 40% ODB and the US-NCAP tests

Table 2.  
Optimized materials and gauges for key components

Part Name	FSV-Baseline			Optimized New Design		
	Material	Gauge (mm)	Mass (kg)	Material	Gauge (mm)	Mass (kg)
Shotgun	HF1550	1.0/1.2/1.5	8.9	HF1550	1.2/1.2/1.3	8.5
Bumper Beam	DP780	1.0	3.7	HF1550	0.8	3.5
Rocker Reinf	CP1470	1.0	11.9	CP1470	1.2/1.0	12.7
Rocker Outer	DP590	0.8	6.2	TRIP980	0.8	6.2
Hinge Pillar Inner	DP780	1.2	3.3	HF1550	1.2	3.3
Hinge Pillar Outer	DP590	0.8	2.5	TRIP980	0.8	2.5
A-Pillar Inner	HF1550	0.7	1.7	HF1550	0.7	1.7
A-Pillar Outer	DP590	0.8	5.3	TRIP980	0.8	5.3
Roof Rail Inner	HF1550	0.95/0.8	2.1	HF1550	0.95/0.8	2.1
Roof Rail Reinf	HF1550	0.7	4.1	HF1550	0.7	4.1
Front Rail	TRIP980	1.8/2.0/1.9/1.8	18.7	TRIP980	1.8/1.9/1.8/1.8	18.5
		<b>Total Mass (kg)</b>	<b>68.4</b>			<b>68.4</b>

It is noticed from Figure 7(b) that the front wheel was still forced rearward into the footwell, causing the deformation of the rocker and hinge pillar. To alleviate the impact from the front wheel, a second design concept was proposed based on the previous design concept by optimizing the directions the bumper beam to be extended. As shown in Figure 10 for optimized design concept #2, the straight outward extension in the previous design concept was modified by extending the bumper beam:

- Rearward to be as close as possible to the front edges of the front wheel;
- Downward to be as close as possible to the centerline of the front wheel.

During the impact in the SORB test, the extended bumper beam is intended to move rearward to contact with the outer edges of the front wheel and subsequently to turn the front wheel outward. To turn the front wheel more effectively, the bumper beam was designed with a tailor-welded-blank (TWB) or two parts joined together with a relatively stiffer outside portion.

Figure 11(a) shows the deformation of optimized design concept #2 in the SORB test. As the intended design, the front wheel was turned outward by the bumper beam to reduce the direct impact force from the front wheel to the rocker and hinge pillar. When compared to the deformation of optimized design concept #1 shown in Figure 7(b), optimized design concept #2 had less deformation in the rocker, hinge pillar and the roof rail. Consequently, the intrusion into the occupant compartment was reduced by 2 cm, as shown in Figure 11(b). Optimized design concept #2 further improved the structural rating to “Good” for the upper occupant compartment with higher probability and confidence level, enabling mass reduction while maintaining the “Good” overall structural rating.



Materials and gauges for the two optimized design concepts are compared in Table 3. In optimized design concept #2, the gauges of the bumper beam were increased to 1.2 mm for its outside portions, while the front and middle portions of the TWB shotgun were downgauged to 0.6 and 0.8 mm, respectively. Because concept #2 changed the front wheel kinematics, the front portion of the TWB rocker reinforcement and the rocker outer could be downgauged by 0.1 mm. Total mass reduction of 1.3 kg was achieved with optimized design concept #2, while maintaining the “Good” overall structural rating.

## THE NEXT GENERATION AHSS

The current study focused on the countermeasure design optimizations using the available steels grades used in the FSV vehicle model. Since then, the next generation AHSS with an excellent combination of strength and ductility have become available and been commercialized. For example, U. S. Steel’s third generation steel with 980 MPa minimum tensile strength (980 XG3™ steel) has comparable crash performance to HF1550 with minimum weight penalty [8, 9]. It was demonstrated that same gauged 980 XG3™ steel could replace hot formed HF1550 steel for hinge pillars for a sedan with complex geometry, and achieved a “Good” rating in IIHS SORB crash test [9]. The benefits of cold-stamping versus hot-stamping include cost reduction and improved corrosion protection.

Other currently available next generation AHSS are:

1. Super high formable steel with 1180 MPa minimum tensile strength (1180SHF);
2. Martensitic steel with 1500 MPa minimum tensile strength (MS1500);
3. Martensitic steel with 1700 MPa minimum tensile strength (MS1700);
4. Dual phase steel with 1470 MPa minimum tensile strength (DP1470).

Table 4 shows the potential material recommendation with the next generation AHSS, which have equivalent strength and improved ductility compared to the steel grades used in the FSV model. 980 XG3™ steel can be used to replace HF1550 and TRIP980 for the shotgun, hinge pillars, A-pillar outer, front rail and rocker outer. The HF1550 bumper beam, rocker reinforcement and roof rail can be replaced with MS1500/MS1700, DP1470 and 1180SHF, respectively. The flow stresses of the cold-stamped 980 XG3™ and 1180SHF parts can match that of the hot-stamped HF1550 parts when the work and bake hardening effects are considered. The 980 XG3™ and 1180SHF steels also demonstrate greatly improved fracture resistance performance during crash events because their fracture limit strains are significantly higher than that of HF1550 [10, 11]. It is expected to achieve similar crash performance with the next generation AHSS for the two optimized designs shown in Table 3 at similar mass savings, but reduced costs.

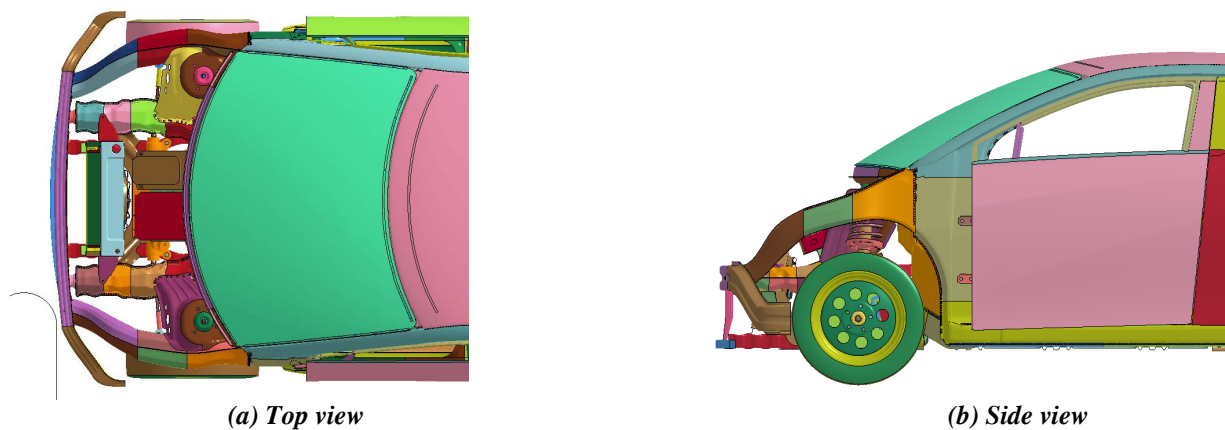
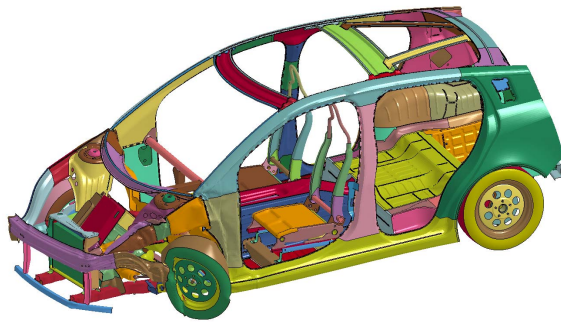
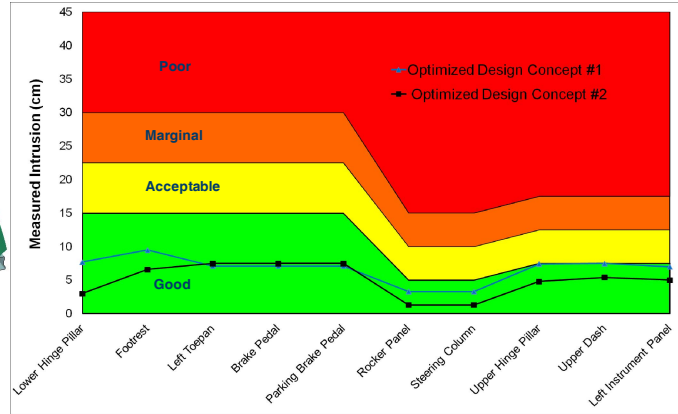


*Figure 10. Optimized design concept #2 for SORB*



(a) Deformation



(b) Intrusion

Figure 11. The optimized design concept #2 in the SORB test

Table 3.  
Materials and gauges for the two optimized design concepts

Part Name	Optimized Design Concept #1			Optimized Design Concept #2		
	Material	Gauge (mm)	Mass (kg)	Material	Gauge (mm)	Mass (kg)
Shotgun	HF1550	1.2/1.2/1.3	8.5	HF1550	0.6/0.8/1.3	6.2
Bumper Beam	HF1550	0.8	3.5	HF1550	0.8/1.2	5.6
Rocker Reinf	CP1470	1.2/1.0	12.7	CP1470	1.1/1.0	12.4
Rocker Outer	TRIP980	0.8	6.2	TRIP980	0.7	5.4
Hinge Pillar Inner	HF1550	1.2	3.3	HF1550	1.2	3.3
Hinge Pillar Outer	TRIP980	0.8	2.5	TRIP980	0.8	2.5
A-Pillar Inner	HF1550	0.7	1.7	HF1550	0.7	1.7
A-Pillar Outer	TRIP980	0.8	5.3	TRIP980	0.8	5.3
Roof Rail Inner	HF1550	0.95/0.8	2.1	HF1550	0.95/0.8	2.1
Roof Rail Reinf	HF1550	0.7	4.1	HF1550	0.7	4.1
Front Rail	TRIP980	1.8/1.9/1.8/1.8	18.5	TRIP980	1.8/1.9/1.8/1.8	18.5
<b>Total Mass (kg)</b>			<b>68.4</b>	<b>67.1</b>		

Table 4.  
Material recommendations with the next generation AHSS

Part Name	FSV Material	Next Gen AHSS
Shotgun	HF1550	980 XG3™
Bumper Beam	HF1550	MS1500/MS1700
Rocker Reinf	CP1470	DP1470
Rocker Outer	TRIP980	980 XG3™
Hinge Pillar Inner	HF1550	980 XG3™
Hinge Pillar Outer	TRIP980	980 XG3™
A-Pillar Inner	HF1550	1180SHF
A-Pillar Outer	TRIP980	980 XG3™
Roof Rail Inner	HF1550	DP1470
Roof Rail Reinf	HF1550	1180SHF
Front Rail	TRIP980	980 XG3™

## CONCLUSIONS

In this study, two optimized countermeasure design concepts for the front end structures were developed for the IIHS SORB crash test. The optimized designs helped the vehicle slide away from the SORB, turned the front wheel outside and converted more impact energy to vehicle kinetic energy. The intrusion into the occupant compartment was reduced and a “Good” overall structural rating was achieved in the SORB test with the optimized design concepts. The optimized design concepts also reduced the intrusion in the IIHS 40% ODB frontal crash test and maintained a similar crash pulse in the NCAP full frontal crash test. The improved crash performance in the IIHS SORB and the 40% ODB frontal crash tests were achieved without mass increase. When used together with UHSS, a potential mass reduction of 1.3 kg could be realized with the optimized design concepts. The potential material replacement with the next generation AHSS is recommended at reduced costs.

## REFERENCES

- [1] C. Sherwood, J. Nolan and D. Zuby. 2009. “Characteristics of Small Overlap Crashes,” 21st Enhanced Safety of Vehicles (ESV) Conference, paper no. 09-0423.
- [2] Insurance Institute for Highway Safety. 2014. Small Overlap Frontal Crashworthiness Evaluation, Crash Test Protocol (Version III), May 2014, Arlington, VA.
- [3] Insurance Institute for Highway Safety. 2012. Small Overlap Frontal Crashworthiness Rating Protocol (Version II), Rating Guidelines for Restraints and Dummy Kinematics, Injury Measures, and Vehicle Structural Performance, Weighting Principles for Overall Rating, December 2012, Arlington, VA.
- [4] E. Elliott, C. Roche and J. Reddy, “Small Overlap Impact Countermeasure-Front Door Hinge Pillar Dual Box,” SAE Technical Paper 2016-01-0142, 2016, doi:10.4271/2016-01-0142.
- [5] J. Shaw, Y. Kuriyama and M. Lambriks. 2011. "Achieving a Lightweight and Steel-Intensive Body Structure for Alternative Powertrains," SAE Technical Paper 2011-01-0425, 2011, doi:10.4271/2011-01-0425.
- [6] G. Chen, M. Shi, and T. Tyan. 2009. "Cross-Section Optimization for Axial and Bending Crushes Using Dual Phase Steels," SAE Int. J. Mater. Manuf. 1(1):537-547, 2009, doi:10.4271/2008-01-1125.
- [7] G. Chen, M. Shi, and T. Tyan. 2012. "Optimized AHSS Structures for Vehicle Side Impact," SAE Int. J. Mater. Manf. 5(2):304-313, 2012, doi:10.4271/2012-01-0044.
- [8] T.M. Link, and B.M. Hance, “Axial and Bending Crash Performance of Advanced High-Strength Steels,” Intl. Symp. On New Developments in Advanced High-Strength Steels, 19-30, AIST 2017, Keystone, CO.
- [9] P. McKune, A. Khutorsky and K. Butala, “Replacing Press Hardenable Steel with 980 MPa Generation 3 Steel for Automotive Pillars,” SAE Technical Paper 2018-01-0117, 2018, doi:10.4271/2018-01-0117.
- [10] X. Chen, G. Chen and L. Huang, “Validation of GISSMO Model for Fracture Prediction of a Third Generation Advanced High Strength Steel,” SAE Technical Paper 2018-01-0107, 2018, doi:10.4271/2018-01-0107.
- [11] X. Chen, G. Chen, L. Huang and M.F. Shi, “Calibration of GISSMO Model for Fracture Prediction of A Super High Formable Advanced High Strength Steel,” 15<sup>th</sup> International LS-DYNA User Conference, June 2018, Dearborn, MI.

## ACKNOWLEDGEMENT

The authors would like to thank United States Steel Corporation and Ford Motor Company for permission to publish this manuscript.

## DISCLAIMER

The material in this paper is intended for general information only. Any use of this material in relation to any specific application should be based on independent examination and verification of its unrestricted availability for such use and a determination of suitability for the application by professionally qualified personnel. No license under any patents or other proprietary interests is implied by the publication of this paper. Those making use of or relying upon the material assume all risks and liability arising from such use or reliance.

# **ROLE OF TRAUMATIC SEATBELT FAT STRANDING IN AUTOMOTIVE CRASH INJURY ANALYSIS**

**Chandrashekhar K. Thorbole**

Thorbole Simulation Technologies LLC  
United States

**Prashant Naik**

SKN Medical College, Radiology Department  
India

Paper Number 19-0137

## **ABSTRACT**

The seatbelt is a primary and the most important passive safety device protecting occupants in all crash modes. The belt must work in harmony with other passive safety devices such as the frontal airbag, knee bolster and the seat to increase the level of occupant protection in a head-on crash. Failure of any component to restrain the occupant effectively in conjunction with the seatbelt can produce adverse occupant kinematics. Occupant submarining in a frontal crash is an occurrence when the belt moves from the desired stronger skeletal site and loads undesired anatomical location during the forward excursion of the occupant. The focal loading of the abdomen and ribs by the seatbelt produces abdominal and thorax severe injuries.

Subcutaneous fat appears typically darker on the radiographic film with an appropriate window. The focal loading from the seatbelt on the body tends to increase the density of the fat along the course of the seatbelt routing. The increase in the density of fat rises its attenuation and makes the fat appear lighter/whiter on the film. The change in the density, due to traumatic seatbelt loading, can be used in conjunction with other medical and physical evidence to demonstrate the occurrence of submarining. This type of analysis is also useful for the medical provider to take appropriate actions when the trauma patient first appears in the emergency department.

The purpose of this study is twofold: (1) to demonstrate the submarining detection techniques and methodologies using the NHTSA crash-test instrumentation data; and (2) to present real-world crashes as evidence of occupant submarining using fat-stranding analysis in conjunction with other medical and physical evidence.

## **INTRODUCTION**

Automotive passive safety performance in a frontal crash scenario depends on how well the seatbelt and other safety components work together to dissipate occupants kinetic energy while exerting a load on the stronger osseous anatomy[1,2,3,4,5]. However, if the seatbelt transfers load on the body regions such as the abdomen and the ribs, it changes the injury pattern and its severity[6,7]. Occupant submarining in a frontal crash involves slipping of properly placed lap belt from the iliac spine on to the abdomen[8,9]. The traumatic contact between the lap belt and the abdomen as a result of submarining produce direct compressive and shear forces tangential to the abdominal wall exerted by the belt. This force application pattern is evident from the crash testings belt dynamics on the abdomen at the instant of submarining.

The abdominal wall anatomy is composed of skin, superficial subcutaneous fat (Camper fascia), Scarpa fascia and muscle layers separated by their fascia's. The subcutaneous fat, a low dense substance appears darker on the scans due to decreased attenuation. However, with the application of compressive and shear loading on the subcutaneous fat can increase its density in the load application regions. The increase in the density compared to the surrounding local area cause pockets of increased attenuation that appears lighter on the CT scans. Figure 1 shows an example of increased fat density causing increased attenuation making the pockets of fat in the subcutaneous tissue to appear lighter on the CT scan. Figure 2 shows the typical appearance of the subcutaneous fat without any fat stranding.

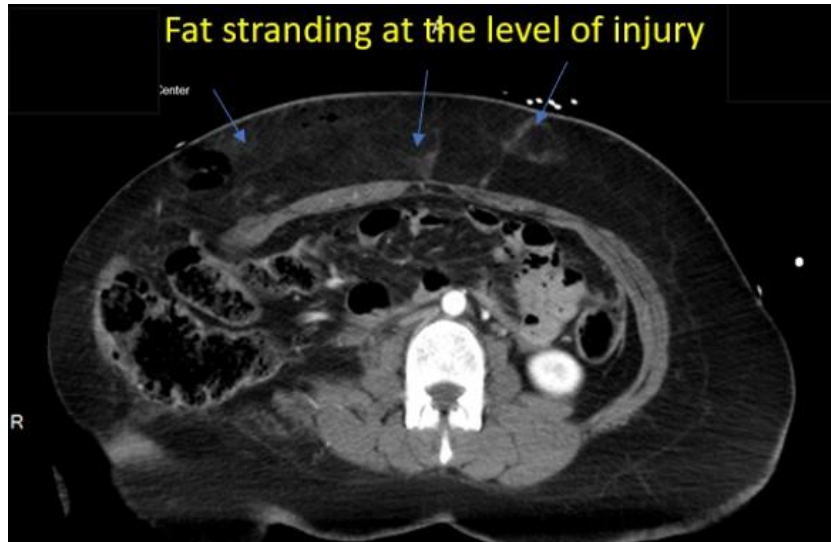


**Figure 1. Subcutaneous fat stranding at the level of seatbelt injury.**



**Figure 2. Subcutaneous fat appearance on the CT scan in absence of traumatic fat stranding.**

Submarining detection in itself is separate research as submarining prevention. Detection of submarining is mainly challenging due to the use of mechanical crash dummies used for the design and performance evaluation process. The Hybrid III 5th is sensitive to submarining compared to the 50th and the 95th crash dummies[10,11] making it a relative better choice to detect the submarining.

The seatbelt load profile, A.S.I.S load cell output, and the film analysis can be effectively used to detect the occupant submarining or risk of submarining in a frontal crash scenario. The primary objective of this paper is to demonstrate the submarining detection method using standard regulatory test data and to discuss the application of fat-stranding analysis to explain submarining in real-world crashes and factors dictating the outcome.

## METHODOLOGY

NHTSA crash-test database [12] is searched for the frontal tests with 5th percentile ATD in the rear seat. Two rigid barrier tests were selected to compare the data and to demonstrate the submarining detection techniques using film and the seatbelt data. Vehicles in both tests belonged to the same class.

### Test-1 (NHTSA Test No 9332)

This test involves a 2015 Chevrolet Malibu four-door sedan impacted into a flat rigid barrier at 35 mph (56 kph). Figure 3 shows the film kinematics sequence of the right rear 5th ATD that demonstrates no occurrence of submarining. Figure 4 and 5 show the lap and shoulder belt plots. Figure 6 and 7 shows the right and left ASIS Force plots.



*Figure 3. ATD kinematics with no submarining.*

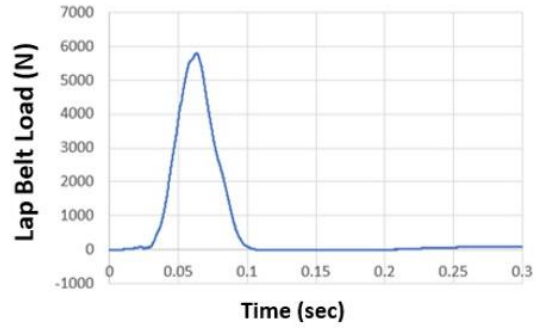


Figure 4. Lap belt load.

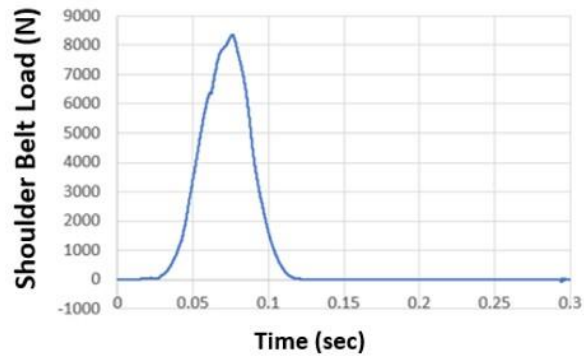


Figure 5. Shoulder belt load.

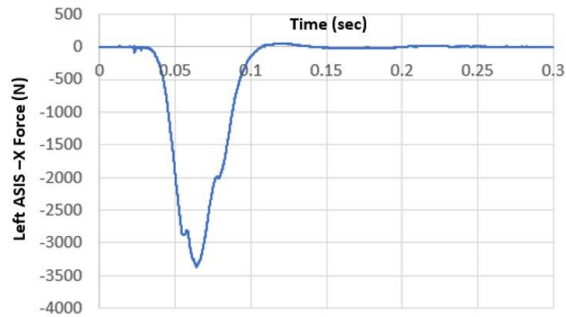


Figure 6. Left ASIS load.

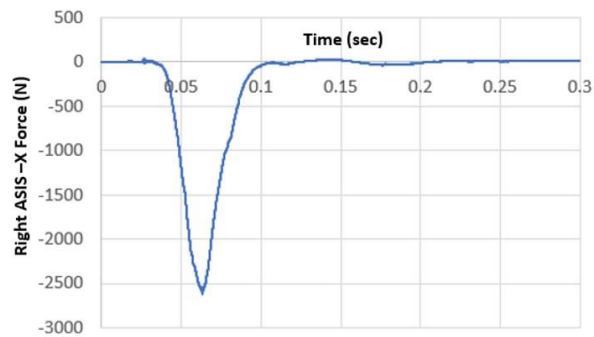


Figure 7. Right ASIS load.



**Test-2 (NHTSA Test No 9336)**

This test involves a 2015 Mazda 3 four-door hatchback sedan impacted into a flat rigid barrier at 35 mph (56 kph). Figure 8 shows the film kinematics sequence of the right rear 5th ATD that demonstrates no occurrence of submarining. Figure 9 and 10 show the lap and shoulder belt plots. Figure 11 and 12 shows the right and left ASIS Force plots.



**Figure 8. ATD kinematics with submarining.**

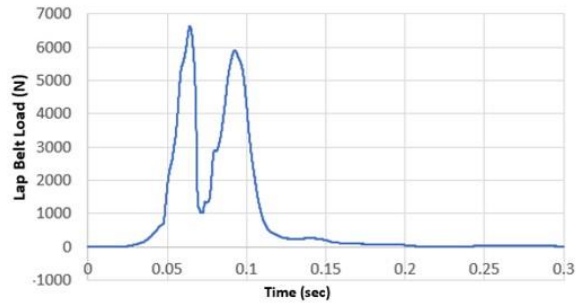


**Figure 9. Lap belt load for Mazda 3 test.**

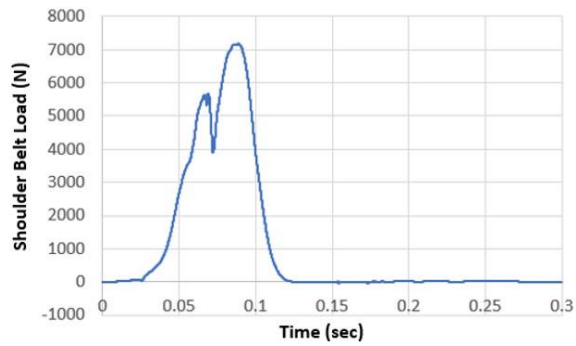


**Figure 10. Shoulder belt load for Mazda 3 test.**

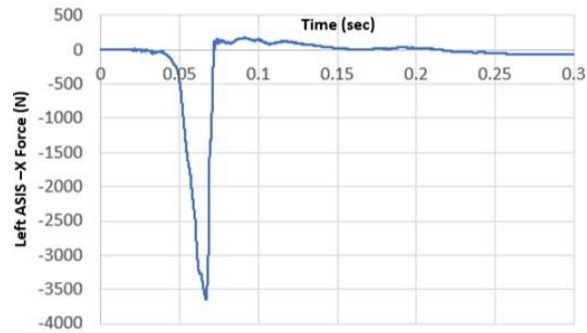


**Figure 11. Left ASIS load for Mazda 3 test.**

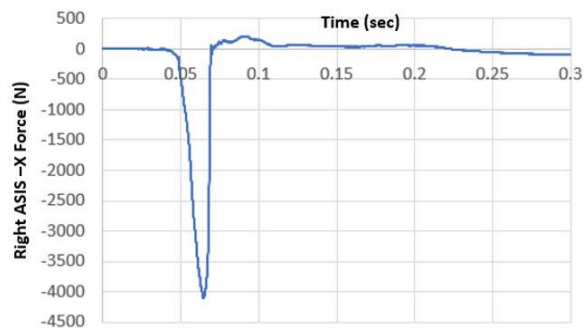


**Figure 12. Right ASIS load for Mazda 3 test.**

## NHTSA TEST COMPARISON

### Film Analysis

The film comparison for the ATD kinematics analysis indicates submarining in Test 9336 with 2015 Mazda 3 producing unfavorable ATD kinematics. Test 9332 with 2015 Chevy Malibu shows the favorable occupant kinematics with no submarining of the ATD. The film analysis shows the lap belt kinematics with respect to the ATD pelvis. In the case with submarining, the pelvis rotates backward while moving forward allowing the lap belt to slip from the ASIS zone and migrate upwards and into the abdomen. However, in case of no submarining scenario, the backward pelvis rotation is prevented causing the lap belt to firmly hold on to the ASIS zone during its forward excursion. Figure 13 shows the still image from the film analysis of the Mazda test highlighting the lap belt into the abdominal cavity during the forward excursion of the pelvis. The image also shows the upper torso recline with shoulder point (S-point) lagging behind the H-point. Figure 14 shows the still image from the Chevrolet test highlighting the lap belt on the pelvis during the forward excursion of the pelvis. The image also shows that the shoulder point is not lagging the H-point.



Figure 13. Unfavorable kinematics with submarining.

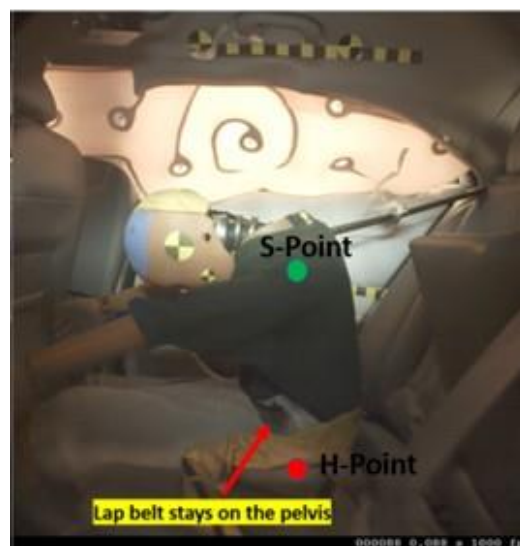


Figure 14. Favorable occupant kinematics without submarining.

### Seat Belt Load Analysis

The seat belt load profile, with and without submarining, shows a clear difference. Figure 9 shows the lap belt profile with submarining and Figure 4 without submarining. The belt load profile with submarining always shows a classic hump as visible in Figure 9. This load profile occurs when the pelvis is allowed to rotate backward during its forward excursion on the seat. The backward rotation causes the lap belt to slip from the pelvis causing the drop in the lap belt load. However, the load starts rising once the belt again engages with the abdomen during the ATD's forward excursion. This pelvis rotation kinematics produce the double hump belt load profile. The single loop nature of the belt with the free belt transfer at the latch plate also affects the shoulder belt load profile and demonstrates the hump as shown in Figure 10.

### A.S.I.S Load Analysis

The Hybrid III 5<sup>th</sup> pelvis is equipped with an A.S.I.S load cell capable to measure the belt load and the moment on the pelvis. Figure 15 shows the location of the A.S.I.S load cell on the pelvis of the hybrid 5<sup>th</sup> ATD.

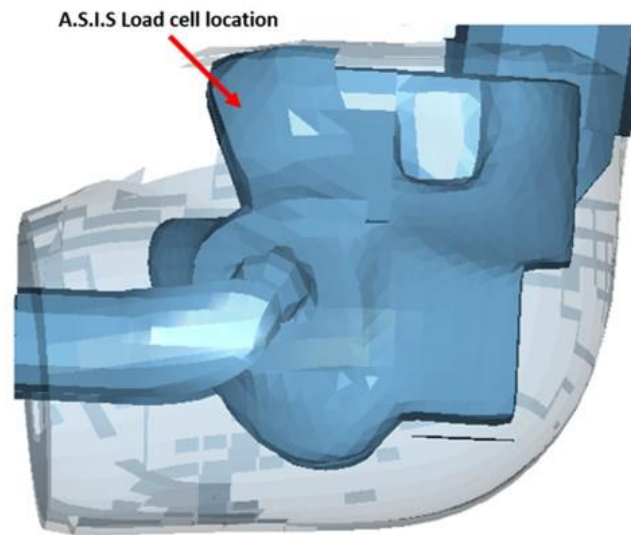


**Figure 15. Location of A.S.I.S load cell on the pelvis to measure belt load on the pelvis.**

Both tests measured the A.S.I.S loads and moments. In case of submarining, the lap belt slips off from the pelvis producing a sudden drop of the load on the pelvis. Figure 11 and 12 shows the sudden load drop at the right and left A.S.I.S. load cell. With no submarining, the load gradually drops until the ATD starts its rebound as shown in Figure 6 and 7.

## REAL WORLD FRONTAL CRASH AND SUBMARINING

In a real-world frontal crash, the occupant's injury pattern in conjunction with a detailed analysis of all other factors provides crucial insight regarding the occupant's motion and injury-producing cause. The subcutaneous fat stranding an increase in its density due to the seatbelt loading can manifest increased attenuation on the CT scan [13,14,15]. The traumatic seatbelt fat stranding observations using CT scan facilitate over-all injury mechanism analysis.

### Case Report-1

A 42-year-old female passenger in a right front seat in a mid-size four-door sedan, who was wearing her seatbelt, was involved in a left frontal offset crash. The vehicle EDR data showed 33 mph longitudinal delta V and 11 mph lateral delta-V towards the driver side. She was 5ft 4 inches (164cm) tall and weighed 169 lb (76 kg) at the time of the crash. She sustained head and neck injuries including cervical neck fractures and disruption of posterior ligaments and complex at C1-C2 level with spinal cord injury. Her injury at the C1-2 level is classified as flexion-distraction type injury. She also sustained multiple abdominal injuries including mesenteric defects at mid and distal ileum, 1cm

perforation on the lateral border of the cecum and a large right lower abdominal wall traumatic hernia. She also sustained severe bilateral lower lobe atelectasis. Her overall injury pattern and severity was consistent with her submarining on the right front seat. Her CT scan review demonstrated fat-stranding at the hips and the final lap belt position on the abdomen. Figure 16 shows the subcutaneous fat stranding at the A.S.I.S level on the axial CT. Figure 17 shows the corresponding display of fat stranding on the coronal view. Figure 18 shows the fat-stranding at the final displaced position of the lap belt. The lap belt total displacement on the abdomen was 5.2 inches consistent with the marks on the CT scan and her abdominal injuries. Figure 19 shows the schematics of the initial and final belt position with respect to her abdominal injuries. Her submarining produced unfavorable kinematics causing her neck interaction with the shoulder belt producing flexion-distraction injuries at the C1-C2 level.

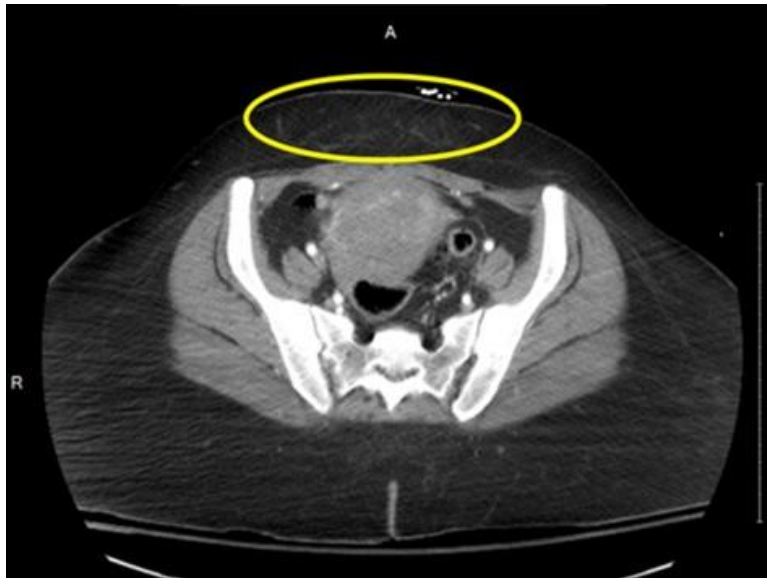


**Figure 16. Axial CT at slightly below A.S.I.S level.**

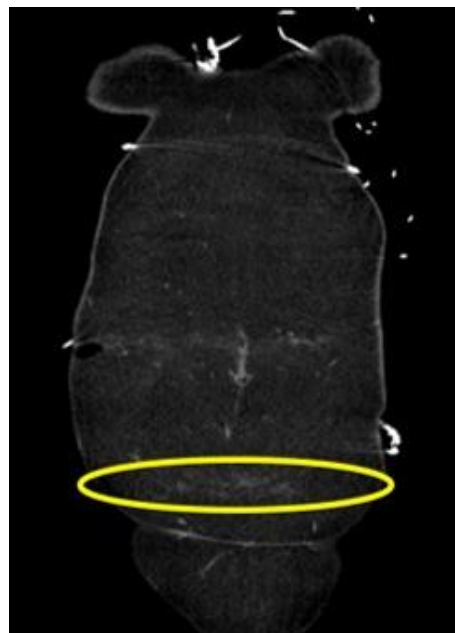


**Figure 17. Coronal view of the fat stranding marks at the A.S.I.S level.**

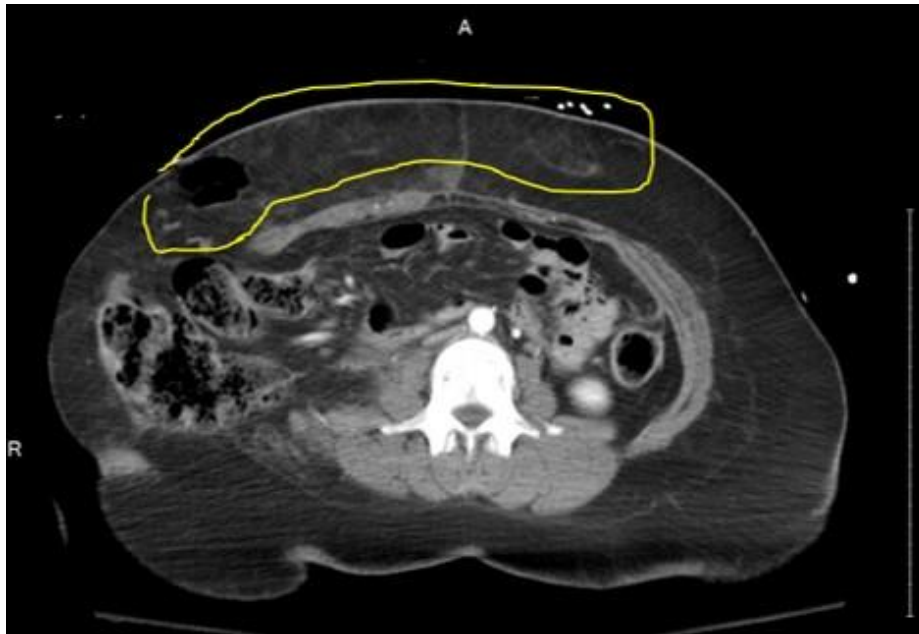


**Figure 18. Axial CT at the level of L2-L3 with prominent fat stranding abdominal injuries.**

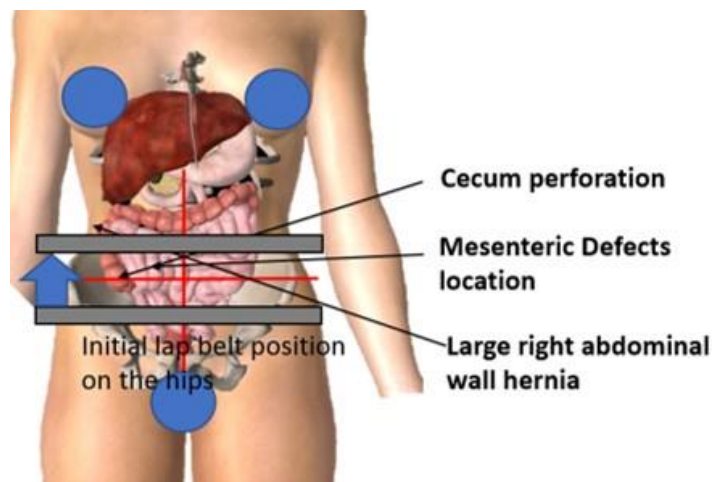


**Figure 19. Schematics of the belt movement and abdominal injuries.**

### **Case Report-2**

An 11-year-old female passenger in the second row right seat, who had her seatback reclined to approx. 58-60 deg with the vertical, was sleeping with her back on the seatback. She was a properly belted occupant. However, the seatback recline caused her shoulder belt positioned away from her upper torso as the D-ring in this vehicle is mounted on the B-pillar. The frontal crash caused the vehicle to experience a longitudinal change in velocity of 20mph with a minor lateral change in velocity. The seatback recline at the time of crash caused her to submarine under the lap belt. Her acute injury pattern involved clavicle fracture, chance fracture at L2-L3 level in association with several abdominal injuries. She also sustained upper and lower extremity fractures along with facial fractures. Figure 20 shows the axial CT at the level of the chance fracture demonstrating prominent traumatic fat stranding in the anterior abdomen.





**Figure 20. Fat stranding at the level of chance fracture.**

Figure 21 shows the axial CT at the level of A.S.I.S of the child occupant that shows the fat-stranding. The increase in the fat density at this level confirms the traumatic contact between the belt and the pelvis. However, due to her reclined position, the pelvis failed to hook the A.S.I.S firmly to prevent her slipping under the lap belt. Figure 22 shows the zoomed anterior portion between the left and right A.S.I.S. Figure 23 shows the schematics of lap belt travel on her body.



**Figure 21. Fat stranding at the level of A.S.I.S**

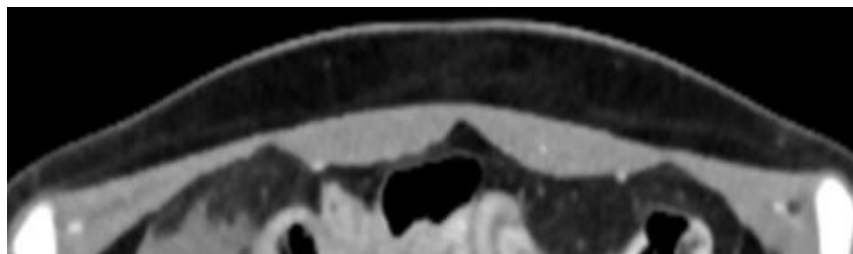


**Figure 22. Zoomed image at the level of A.S.I.S demonstrating fat stranding in the subcutaneous fat.**



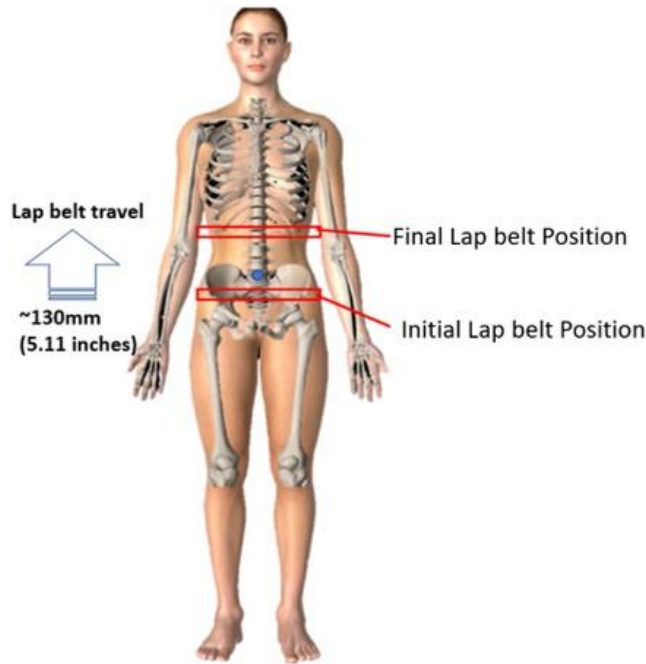


**Figure 23. Lap belt displacement from the pelvis to upper abdomen during the crash.**

## CONCLUSIONS

Occupant submarining in a frontal crash scenario is explained using standard regulatory test data and video. The paper discusses the submarining detection techniques using the film, seatbelt data, and A.S.I.S data. The belt data shows a classic double hump characteristic in the presence of the pelvis backward rotation during its forward excursion on the seat. The film and data analysis show that preventing the backward pelvis rotation during its forward excursion produces overall favorable occupant kinematics by preventing the occupant submarining. This paper shows how the increased attenuation in the subcutaneous fat, below the skin (Camper's fascia) manifest on the CT scan when the belt exerts the compressive and shear loading on the body. Traumatic fat-stranding analysis can be successfully employed in injury causation analysis in conjunction with other available information and data. Seatbelt use, its initial and final position can be determined using the fat stranding analysis.

## REFERENCES

- [1] Adomeit, Dieter. Evaluation methods for the biomechanical *quality of restraint systems during frontal impact*. No. 770936. SAE Technical Paper, 1977.
- [2] Adomeit, D. "SEAT DESIGN-A SIGNIFICANT FACTOR FOR SAFETY BELT EFFECTIVENESS. IN: SEAT BELTS: THE DEVELOPMENT OF AN ESSENTIAL SAFETY FEATURE." In Paper No. 791004, presented at the 23rd Stapp Car Crash Conference, San Diego, CA, October 1979. 2003.
- [3] Foret-Bruno, Jean-Yves, et al. "Comparison of Thoracic Injury Risk in Frontal Car Crashes for Occupant Restrained without Belt Load Limiters and Those Restrained with 6 kN and 4 kN Belt Load Limiters." *Stapp car crash journal* 45 (2001): 205-224.
- [4] Adomeit, Dieter, and Alfred Heger. Motion sequence criteria and design proposals for restraint devices in order to avoid unfavorable biomechanic conditions and submarining. No. 751146. SAE Technical Paper, 1975.
- [5] Håland, Yngve. "The evolution of the three point seat belt from yesterday to tomorrow." In *IRCOBI Conference, Madrid*. 2006.

- [6] Thorbole, Chandrashekhar K. "Seatbelt submarining injury and its prevention countermeasures: How a cantilever seat pan structure exacerbate submarining." *Journal of family medicine and primary care* 4.4 (2015): 587.
- [7] Elhagediab, Ali M., and Stephen W. Rouhana. "Patterns of abdominal injury in frontal automotive crashes." In *16 th International ESV Conference Proceedings*, pp. 327-337. 1998.
- [8] Leung, Y. C., C. Tarriere, D. Lestrelin, C. Got, F. Guillon, Manish M. Patel, and Jacques Hureau. "Submarining injuries of 3-point belted occupants in frontal collisions-description, mechanisms and protection." In *Proceedings: Stapp Car Crash Conference*, vol. 26, pp. 173-205. Society of Automotive Engineers SAE, 1982.
- [9] Luet, Carole, Xavier Trosseille, Pascal Drazétic, Pascal Potier, and Guy Vallancien. *Kinematics and Dynamics of the Pelvis in the Process of Submarining using PMHS Sled Tests*. No. 2012-22-0011. SAE Technical Paper, 2012.
- [10] Couturier, Stéphane, Jacques Faure, Ricardo Satué, Joaquim Huguet, and Julien Hordonneau. "Procedure to assess submarining in frontal impact." In *20th International Technical Conference on the Enhanced Safety of Vehicles (ESV) National Highway Traffic Safety Administration*, no. 07-0481. 2007.
- [11] Uriot, Jerome, Pascal Baudrit, Pascal Potier, Xavier Trosseille, Philippe Petit, Hervé Guillemot, Laurent Guérin, and Guy Vallancien. *Investigations on the belt-to-pelvis interaction in case of submarining*. No. 2006-22-0003. SAE Technical Paper, 2006.
- [12] <https://www-nrd.nhtsa.dot.gov/database/VSR/veh/QueryTest.aspx>
- [13] Hartka, Thomas, G. Poplin, Kenadeed Hersi, Abigail Booker, and M. Sochor. "Comparison of Visual and CT 3D Reconstructed Abdominal Seatbelt Sign Locations." *TRAFFIC INJURY PREVENTION* 15 (2014): S247-S249.
- [14] Hartka, Thomas, 2013 CIREN Presentations " Determination of Seat Belt Use and Positioning with Three-Dimensional CT Fat Volume Rendering in CIREN Frontal Crash Case" [https://one.nhtsa.gov/Research/Crash-Injury-Research-\(CIREN\)/2013-CIREN-Presentations](https://one.nhtsa.gov/Research/Crash-Injury-Research-(CIREN)/2013-CIREN-Presentations)
- [15] Thorbole, Chandrashekhar." Traumatic Seat Belt Abdominal Fat Stranding Diagnosis on the CT Scan as a Potential Tool for Injury Causation Analysis" Technical Reference Bulletin 2017, Symposium on International Automotive Technology 2017, Pune, INDIA.

## **STRUCTURAL COUNTERMEASURE STUDY ON OBLIQUE OFFSET FRONTAL IMPACT**

Mahendran, Paramasuwom  
Velayudham, Ganesan  
EDAG Inc  
United States of America

Harjinder, Singh  
United States Steel Corporation  
United States of America

Paper Number 19-0131

### **ABSTRACT**

National Highway Traffic Administration (NHTSA) has been investigating an oblique offset frontal impact test. This project evaluates test and simulation results to determine structural changes to reduce occupant compartment intrusion. Review of test results indicated that mid-size Sedans and Pickup trucks showed higher structural intrusions and higher passenger compartment decelerations. Existing Computer Aided Engineering (CAE) models for a mid-size Sedan and Pickup truck were used to evaluate structural changes and the corresponding cost impact to improve performance in the oblique offset test condition. This paper describes the CAE study carried out to study structural reinforcement countermeasures for both the driver and passenger sides of the vehicle in left- and right-side oblique offset frontal impacts. This paper presents the structural mass changes due to reinforcement countermeasures and the cost impact.

### **INTRODUCTION**

The objective of this research was to demonstrate necessary changes to a vehicle's structure and their associated cost in order to reduce the occupant compartment intrusion from NHTSA's oblique offset frontal crash condition. The finite element (FE) models of vehicle to be studied had to meet the structural intrusion requirements for a "Good" or "Acceptable" structural rating in the IIHS small overlap test, "Good" rating in IIHS moderate overlap test rating. The mentioned tests are as shown in Figure 1.

The vehicle models chosen for this study were based on the availability of NHTSA oblique test results, and the availability of a good correlated CAE model. The CAE model should be modified with minimum effort to represent the vehicle for the NHTSA oblique test simulation. It also should represent a latest possible production year vehicle meeting NHTSA's 5-star rating as well as "Good" or "Acceptable" rating of IIHS small overlap frontal impact and "Good" rating of IIHS moderate overlap frontal impact.

Therefore, for the passenger car category, the chosen vehicle was the 2014 Honda Accord with "Good" IIHS ratings, 5-star NHTSA rating. The test results of 2014 Honda Accord were obtained from two NHTSA oblique tests.

For the pick-up category, the chosen vehicle was the 2014 Chevrolet Silverado 1500 with 5-star NHTSA ratings. In this case, the IIHS small overlap test results were not available when the model was developed. But IIHS has already conducted two small overlap tests on the 2016 Chevrolet Silverado, so the test results of 2016 Chevrolet Silverado 1500 were used for this study.

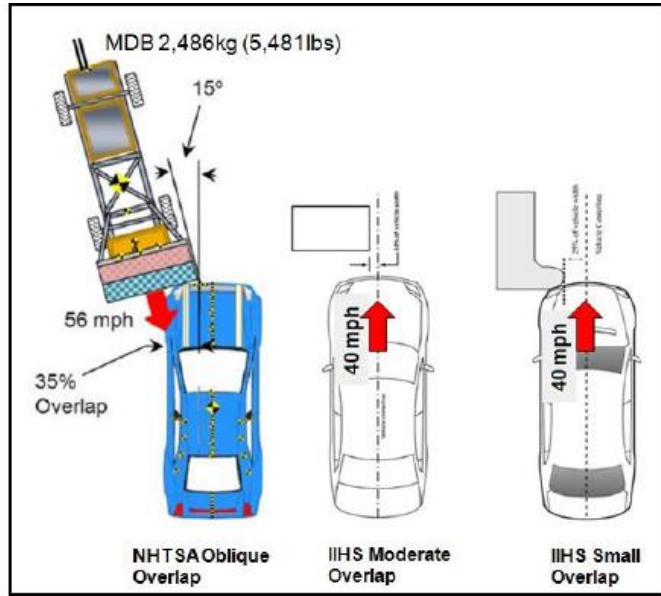


**Figure 1. Vehicle Frontal Offset Tests.**

During a high-speed crash event, the structural intrusions into the toe pan and dash panel are generally caused by hard contact between the intruding wheel and/or the engine/transmission assembly. In general, there are three methods applied to reduce structural intrusions. First is by absorbing as much energy as possible by the deforming structures. Second is by introducing failure points at key locations to deflect the intruding surfaces away from the critical zones on toe pan and dash panel and finally by reinforcing the passenger compartment by using high strength materials with optimized load paths.

This paper outlines the structural countermeasures undertaken to reduce the intrusions by including these three methods. The detailed design of reinforcing components considered manufacturability, joining, and assembly into the vehicle design. Additionally, the cost impact of implementing the countermeasures was also studied.

The technical cost modeling (TCM) approach developed by Massachusetts Institute of Technology’s Materials Systems Laboratory research was used in this research to estimate additional cost accrued due to the countermeasures. The TCM application allows consideration of the whole production process from part production, assembly, logistics and overhead cost.

## COUNTERMEASURE STUDY

The countermeasure study included two vehicles Honda Accord 2014 and 2014 Chevrolet Silverado 1500. In each vehicle study, the FE model was developed first to obtain a baseline model compared to the corresponding crash tests. Upon validating the baseline model with acceptable correlation in terms of structural intrusions, it was used in the countermeasure development.

### Passenger Car – 2014 Honda Accord

The full vehicle FE model of the 2012 Honda Accord which was developed and correlated for NHTSA’s study <sup>[1]</sup> was updated to represent the 2014 MY Honda Accord. A few structural modifications going from 2012 to 2014 vehicle were undertaken by remodeling and updating the 2012 full vehicle model into 2014 full vehicle model. Necessary structural changes were obtained by white light scanning and CAD update of the 2014 vehicle parts accordingly. The details of updating 2012 Honda Accord full vehicle model is out of scope of this paper (it can be found in the NHTSA report [1]).

The updated FE model – 2014 Honda Accord full vehicle model is shown in Figure 2. The 2014 Honda Accord full vehicle model was setup for the following crash load cases.

1. NHTSA Oblique Offset Test (simulating left- and right-side frontal oblique offset)
2. Frontal NCAP Test

3. IIHS Moderate (40%) Frontal Offset Test
4. IIHS Small (25%) Overlap Front Test
5. Lateral NCAP Moving Deformable Barrier Test
6. Lateral NCAP Pole Test
7. IIHS Roof Crush Test
8. IIHS Lateral Moving Deformable Barrier Test

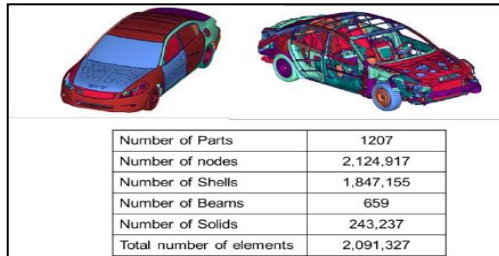


**Figure 2. 2014 Honda Accord CAE Model.**

LS-DYNA simulations were run for each of the load cases. The simulation results were compared to the available test results. The review of the comparison between the FE results and test results concluded that, the overall correlation was acceptable to use the FE model for the oblique frontal impact requirements:

The details of baseline model development and FE results comparisons with test results can be found in [2]. The correlated FE model was used to identify suitable countermeasures design to reduce the occupant compartment intrusions. The countermeasures were based on observed body structure deformations when subjected to oblique impact on the driver and passenger sides. Higher intrusion values were mainly observed in the mid to lower section of the dash panel impacted by battery and brake booster assemblies on the driver side and by the transmission and engine block on the passenger side of the dash panel. Several CAE iterations were conducted to find the optimal set of structural changes. The recommended changes have to be fine-tuned in such a way that vehicle crash performance is not jeopardized for all other crash requirements, and also to make sure the design-packaging space for other vehicle systems is not violated.

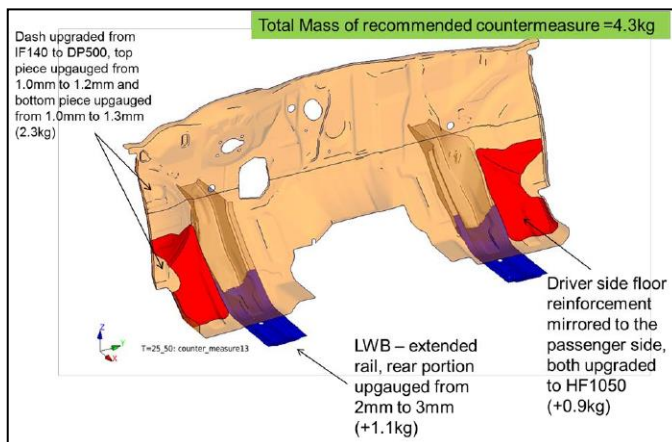


**Figure 3. Structural Countermeasures to Reduce Occupant Compartment Intrusions.**

The recommended changes are shown in Figure 3. These countermeasures added up to an additional mass increase of 4.3 kg for the entire body structure. These changes are given as follows:

1. The dash panel was changed to a laser-welded blank stamping, with increase in thickness from 1.00 mm to 1.20 mm upper segment and to 1.3 mm lower segment, incurring a mass penalty of 2.3 kg. Its material steel grade was also changed from low-strength steel to higher strength dual phase DP500. The dash panel using the higher grade can be successfully formed. The DP500 grade is a good formable grade with over 20 percent elongation.
2. The front rail extensions (left and right) stamped parts that were positioned under the lower dash panel and front floor panels were converted into laser-welded blank (LWB) stampings with two thicknesses. The

thickness of the rear of this part was increased from 2.00mm to 3.00mm, incurring a mass penalty of 1.1 kg for both parts.

- The driver side front floor reinforcement panel (shown in red in Figure 3) was duplicated (mirror image) on to the passenger at an additional mass of 0.90 kg. The grade of steel was also changed to advance high-strength steel HF1050/1500 suitable only for hot-stamping.

Figure 4 shows the comparison of the dash panel before countermeasure (Baseline) and after countermeasure (CM). It can be observed that the countermeasure significantly reduced the intrusion levels of the dash below 150mm (>150mm intrusion is shown in red).

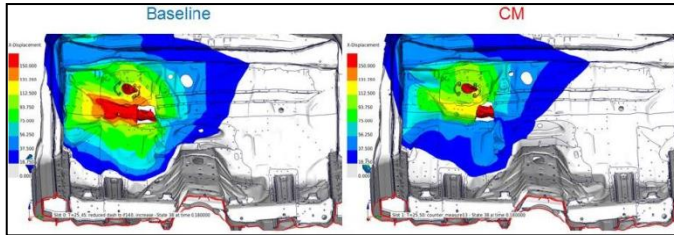


**Figure 4. Baseline vs Countermeasure CAE - Dash View.**

The countermeasure implementation affected little on the assembly process but significantly on the manufacturing process. Therefore, the manufacturing cost changes were estimated. The manufacturing costs of baseline parts and the corresponding countermeasure parts were calculated using the EDAG’s TCM-based cost model mentioned in the introduction section. Incremental manufacturing and assembly costs of the added/subtracted components are summarized in Table 1 and Table 2. The cost of baseline parts weighing 14.73kg was estimated as \$35.54 and the cost of countermeasure parts weighing 19.0kg was estimated as \$59.91. The total cost increase for the countermeasures is \$24.37 (\$59.91 - \$35.54). Total mass increase for the countermeasures is 4.3 kg (19.0 kg – 14.7 kg).

**Table 1. 2014 Honda Accord Baseline Model - Subtracted Parts.**

2014 Honda Accord - Baseline Parts							
Item #	Part Name	Qty per Veh	Steel Grade	Mass ( kg)	Manufacturing Process	Part Piece Cost	
1	Dash Panel	1	Mild 140/270	8.300	Stamping Single Thickness	\$14.64	
2	Dash Panel Bracket Lh	1	DP 500/800	0.900	Stamping Single Thickness	\$3.68	
3	Reinforcement Dash Panel Longitudinal Lh	1	Mild 140/270	2.765	Stamping Single Thickness	\$8.61	
4	Reinforcement Dash Panel Longitudinal Rh	1	Mild 140/270	2.765	Stamping Single Thickness	\$8.61	
				<b>Total Mass</b>	<b>14.73</b>	<b>Total Part Piece Cost</b>	<b>\$35.54</b>

**Table 2. 2014 Honda Accord Countermeasure Model - Added Parts.**

2014 Honda Accord - Counter-Measure Parts							
Item #	Part Name	Qty per Veh	Steel Grade	Mass ( kg)	Manufacturing Process	Part Piece Cost	
1	Dash Panel	1	DP 500/800	10.600	Laser Welded Blank	\$26.76	
2	Dash Panel Bracket Lh	1	HF 1050/1500	0.900	Hot Stamped Single Thickness	\$5.66	
3	Dash Panel Bracket Rh	1	HF 1050/1500	0.900	Hot Stamped Single Thickness	\$5.66	
4	Reinforcement Dash Panel Longitudinal Lh	1	DP 500/800	3.300	Laser Welded Blank	\$10.15	
5	Reinforcement Dash Panel Longitudinal Rh	1	DP 500/800	3.300	Laser Welded Blank	\$10.15	
Additional Assembly Cost						\$1.53	
				<b>Total Mass</b>	<b>19.000</b>	<b>Total Part Piece Cost</b>	<b>\$59.91</b>



## Light-Duty Pickup Truck – 2014 Chevrolet Silverado 1500

A very detailed FE model of the 2014 Chevrolet Silverado 1500 shown in Figure 5 was developed and correlated for NHTSA's lightweighting study [3]

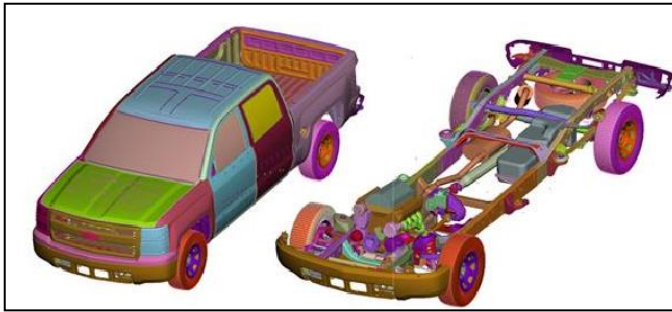


**Figure 5. 2014 Chevrolet Silverado 1500 CAE Model.**

For this study, the FE model was further modified from four-wheel-drive (4WD) to rear-wheel-drive (RWD) to represent the power train similar to NHTSA oblique-tested vehicles. The front drive differential, front drive shafts and power transfer unit were removed from the FE model as shown in Figure 6.

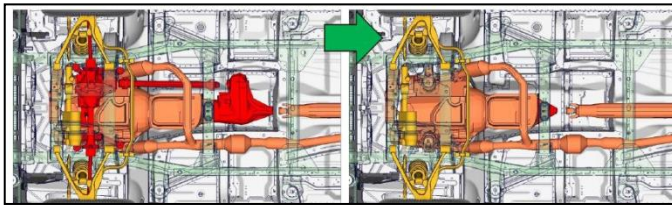


**Figure 6. 2014 Chevrolet Silverado 1500 with the Front Wheel Drive Components Shown in Red.**

For clarification a comparison of the tested vehicle and the updated FE model is shown Table 3.

**Table 3. Oblique Test Vehicle Versus CAE Model.**

Description	Tahoe (Test)	Silverado 1500 (Test)	CAE Model Silverado 1500
Model Year	2016	2012	2014
Drive	RWD	RWD	RWD
Engine Size (L)	5.3	4.8	5.3
Tested Weight ( kg)	2722	2624	2582
Body Style	SUV	Crew-Cab	Crew-Cab

The FE model was correlated with the following crash load cases prior to using it for countermeasure study for the Oblique Impact:

1. NHTSA Oblique Offset Test (simulating left-side frontal oblique offset)
2. IIHS Small (25%) Overlap Front Test. Similarly, the correlated FE model was used to identify suitable countermeasures design to reduce the occupant compartment intrusions. The countermeasures were based on observed structure deformations when subjected to IIHS small offset and NHTSA oblique impact tests on the driver and passenger sides.

Higher intrusion values were observed mainly in the mid to lower section of the dash panel. The mid dash to lower area was impacted by the left front wheel and transmission on the passenger side. The rearward front wheel base intrusions were reduced by adding additional structure to the frame structure which is shown in red in Figure 7.



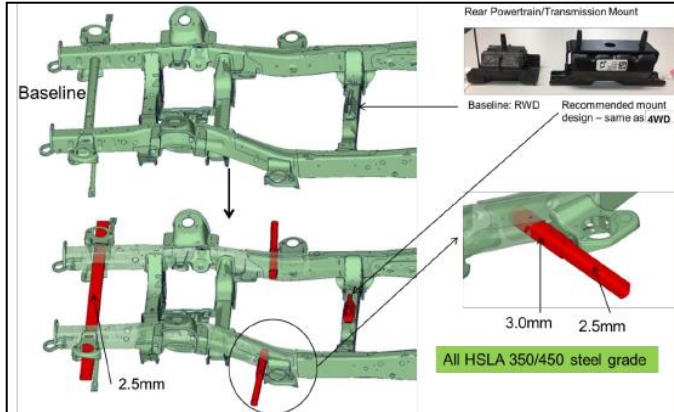


**Figure 7. Structural Countermeasures to Reduce Occupant Compartment Intrusions.**

Higher deformations were also observed for the IIHS small overlap results as shown in the intrusion chart in Figure 8. The developed countermeasures reduced the intrusion values for both load cases but slightly higher intrusions were found for the IIHS small overlap impact. However, the countermeasures improved the intrusions level within the acceptable range. Therefore, the developed countermeasures were decided still as a successful implementation. The countermeasure changes are shown in Figure 7. It increased the parts weight up to 9.0kg. These changes are symmetrical on the left and right sides of the vehicle. These changes are given as follows:

1. Modified front cross member to extend beyond frame rails, to be positioned in front of the front wheel/tires
2. Front wheel blocker bar positioned in front of the cab front mount
3. Change of the rear powertrain/transmission mount to the more robust design used on the 4WD Chevrolet Silverado 1500. It should be note that the 4WD mount is 1.0 kg heavier than the baseline.

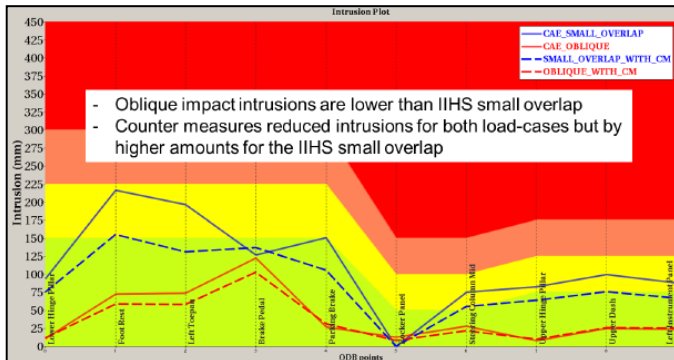


**Figure 8. Structural Countermeasures: Reduce Occupant Compartment Intrusions for Oblique and IIHS Small Overlap.**

Similar to 2014 Honda Accord, the manufacturing costs were estimated for Chevrolet Silverado 1500. In this case, the countermeasure implementation affected both manufacturing and assembly process. Therefore, both manufacturing and assembly costs of baseline parts and the corresponding countermeasure parts were calculated using EDAG's TCM-based cost model. Incremental manufacturing and assembly costs of the added/subtracted components are summarized in Table 4 to Table 7. From these tables, it can be noted that the total cost increase for the countermeasures is \$17.35, total mass increase for the countermeasures is 9.0 kg and the cost impact is \$1.93 per kilogram increase of weight.

**Table 4. 2014 Chevrolet Silverado Baseline Model - Subtracted Parts.**

Silverado Chassis Frame Baseline Manufacturing Costs							
Item #	Part Name	Qty per Veh	Material	Mass ( kg)	Manufacturing Process	Part Piece Cost	
1	Tube Front Crossmember	1	Mild 140/270	3.29	Hydoform Single Thickness	\$5.08	
2	Transmission Rear Mount	1	Various	0.65	Various	\$2.77	
				<b>Total Mass</b>	<b>3.94</b>	<b>Total Parts Cost</b>	<b>\$7.85</b>

**Table 5. 2014 Chevrolet Silverado Countermeasure Model - Added Parts.**

Silverado Chassis Frame Countermeasures Manufacturing Costs							
Item #	Part Name	Qty per Veh	Material	Mass ( kg)	Manufacturing Process	Part Piece Cost	
1	Tube Front Crossmember	1	HLSA 350/450	6.50	Roll Form Closed Profile	\$7.40	
2	Side Frame Tube Inner Upper	2	HLSA 350/450	1.00	Roll Form Open Profile	\$1.82	
3	Side Frame Tube Inner Lower	2	HLSA 350/450	1.20	Roll Form Open Profile	\$2.14	
4	Side Frame Tube Outer	2	HLSA 350/450	2.60	Roll Form Closed Profile	\$6.08	
5	Transmission Rear Mount	1	Various	1.66	Various	\$8.12	
				<b>Total Mass</b>	<b>12.96</b>	<b>Total Part Cost</b>	<b>\$25.56</b>

**Table 6. 2014 Chevrolet Silverado Countermeasure Model - Assembly Cost.**

Silverado Chassis Frame Baseline and Countermeasure Assembly Costs				
Item #	Part Name	Number of Fasteners or MIG Weld Length (mm)	Assembly Process	Cost
1	Chassis Frame Baseline	600 mm	MIG Weld	-\$0.98
2	Chassis Frame Assembly Counter-Measure	1400 mm (additional assembly steps and fixtures cost)	MIG Weld	\$3.78
		4 (washers, step bolts and nuts)	Mechanical Fasteners	\$1.86
Chassis Frame Assembly Cost Increase for the additional Countermeasures				<b>\$4.66</b>

**Table 7. 2014 Chevrolet Silverado Countermeasure Model - Summary Cost and Mass Increase.**

Silverado Chassis Frame Baseline Versus. Countermeasure Costs				
Item #	Part Name	Process	Cost	Mass ( kg)
1	Chassis Frame (Baseline)	Manufacture	-\$7.85	3.94
		Assembly	-\$0.98	
		<b>Total</b>	<b>-\$8.83</b>	
2	Chassis Frame (Counter-Measure)	Manufacture	\$20.54	12.96
		Assembly	\$5.64	
		<b>Total</b>	<b>\$26.18</b>	
<b>Δ Cost / Mass</b>			<b>\$17.35</b>	<b>9.02</b>

## CONCLUSIONS

The 2014 Honda Accord and 2014 Chevrolet Silverado were chosen to conduct countermeasure implementation for NHTSA's oblique offset frontal impact. Both the vehicle has "good" to "acceptable" rating in IIHS small overlap test and "good" rating in IIHS Moderate overlap test. The FE models for both vehicles were correlated to selected crash load cases. CAE based structural modifications were implemented as countermeasures for oblique offset frontal impact targets. The intrusion levels were achieved within 150 mm target for 2014 Honda Accord and within acceptable range for 2014 Chevrolet Silverado 1500. Also, in case of 2014 Chevrolet Silverado, structural deformation was higher in IIHS small overlap compared to NHTSA's oblique offset frontal impact test. In order to reduce the structural deformation of the 2014 Honda Accord, the structural countermeasures caused 4.3kg of mass increase which in turn increased the cost by \$24.37. Whereas, for 2014 Chevrolet Silverado 1500, the countermeasures required 9kg of mass increase and a cost increase of \$17.35.

## REFERENCES

- [1] Singh, H., Kabeer, B., Jansohn, W., Davies, J., Kan, C.-D., Kramer, D., et al. (2012). Mass Reduction for Light-Duty Vehicles for Model Years 2017-2025. NHTSA.
- [2] Singh, H., Ganesan, V., Davies, J., Paramasuwom, M., Gradischnig, L., Wood, P., et al. (2018). Structural Countermeasure/ Research Program: Mass and Cost Increase Due to Oblique Offset Moving Deformable Barrier Impact Test. NHTSA.
- [3] Singh, H., Ganesan, V., Davies, J., Paramasuwom, M., Gradischnig, L., Wood, P., et al. (2016). Mass Reduction for Light-Duty Vehicles for Model Years 2017-2025. NHSTA.

# THE ANALYSIS AND EXPERIMENTAL DEVELOPMENT OF ASPIRATED AIRBAGS FOR CONVENTIONAL AND AUTONOMOUS VEHICLES

**David Breed**

Automotive Technologies International, Inc.  
USA

**Nina Yurchenko,  
Pavlo Vynogradskyy,  
Konstantin Kuzmenko**

Institute of Hydromechanics, National Academy of Sciences of Ukraine  
Ukraine

**Shawe Zhang,**

**Bobby Li**

Shanghai East Joy Long Motor Airbag Co., Ltd., #219 Qingda Rd., Pudong New Area, Shanghai 2011201, China

Paper Number 19-0025

## ABSTRACT

As a part of the Automated Driving Systems (ADS) strategy, the developed aspirated inflation system is applicable for conventional and autonomous motor vehicles where larger airbags are required and the location of vehicle occupants is less precise. It is built to provide for the air entrainment into an airbag from the car passenger compartment. The objective is set to inflate a 50 L airbag within 30 ms with an aspiration ratio,  $A \geq 4$ . Advantageous features of the offered system are a much smaller (less than 1/3) gas generator and stopped airbag deployment on contact with an occupant that eliminates out-of-position occupant injuries.

Regarding engineering, the aspirated inflator is a supersonic pulse ejector designed on the basis of Prandtl-Meyer effect realization. The modeling includes numerical flow simulation combined with subsequent engineering design, fabrication, and experimental testing of models. The results are presented for the “cold-gas” inflator testing where the gas generator operation is imitated by a jet generation from a compressed-air tank using a specially designed high-speed valve. Such an approach enables the verification of the numerical procedure and calculation results obtained for “cold” and “hot-gas” cases. The experimentally found “cold-gas” aspiration ratio is in a good agreement with the numerical prediction varying within  $A=3.1 - 2.1$  depending on a particular design and the operational motive pressure. For the gas generator case, the aspiration ratio values are calculated to be  $\geq 4$ .

Several different designs of the supersonic pulse aspirator are modeled, designed, manufactured, and tested including outer and inner circumferential slit nozzle and multi-nozzle systems. To meet the engineering requirements, multi-stage multivariate studies of measured pressure fields and airbag inflation process are performed.

## INTRODUCTION



*Figure 1. Safety is our goal*

According to NHTSA, the Automated Driving Systems (ADS) must handle the whole task of safe driving by ~2025. The automation is successively provided by technology development both in hardware and software areas starting from cruise control and seat belts within 1995-2000 to lane departure warning, blind spot detection, automated emergency braking, traffic jam assist, self-parking, adaptive cruise control, and many other systems showing features of partially automated safety.

In this connection, the herein offered system of airbag aspirated inflation can significantly contribute to the further development of safety systems up to fully autonomous vehicles with arbitrarily located occupants.

The initial goal is to develop a supersonic pulse ejector for an airbag inflation system to cause air aspiration from a car compartment into the 50-60 L airbag to inflate it within 30 ms with the aspiration ratio above 4. This technology

should have an application potential for larger airbags such as passenger side airbags, side curtain airbags, side-impact airbags and airbags for autonomous vehicles.

The main advantages of the offered aspirated inflator are as follows [1-5],

- the airbag stops deploying on contact with an occupant;
- the required gas generator is less than 1/3 the size of conventional gas generators (see e.g. [6]);
- most of the gas to inflate the airbag comes from the passenger compartment that prevents sudden pressure jump within a vehicle compartment (Figure 2);
- injuries to out-of-position occupants are eliminated;
- the need for staged airbag deployments is eliminated;
- the need for satellite crash sensors for frontal impact sensing is eliminated;
- occupant weight and position sensors are not required.

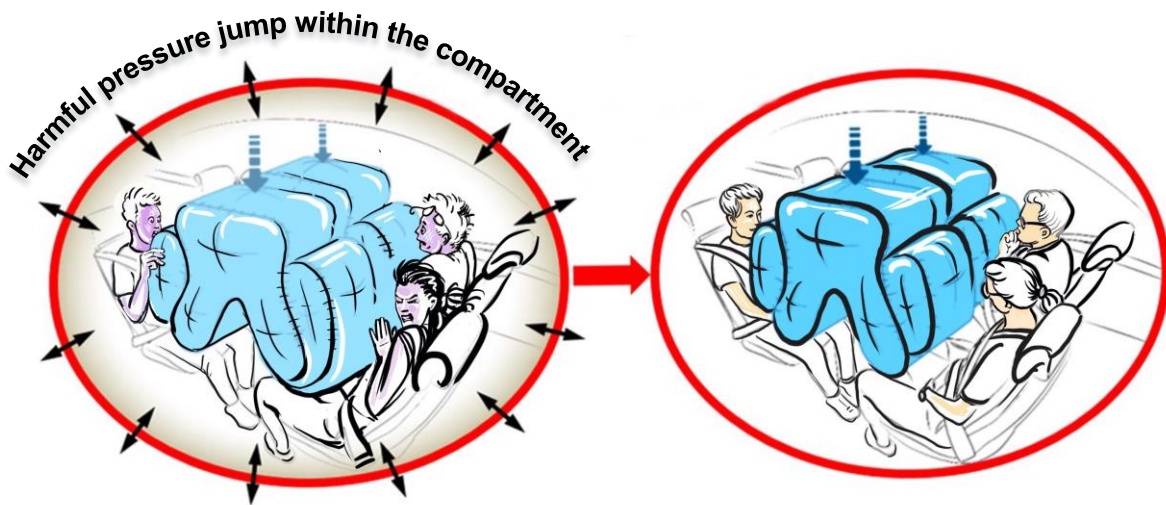


*Figure 2. Illustrated impact of big deployed airbags: operation with conventional (left) and aspirated inflator systems (right)*

The driver side system development comprises numerical modeling and laboratory experiments including the engineering aspirator design and its operation testing in a range of motive pressure values causing air entrainment. Achievement of high performance characterized by the aspiration (entrainment) ratio was realized through a search of an optimal geometry combined with an optimal operational mode.

Numerical simulation provides initial guidance on the aspirator geometry and flow parameters for two temperature regimes. The “cold-gas” regime strictly corresponds to experiments in the compressed-air facility equipped with a high-speed valve which are performed in the Laboratory for Advanced Aerodynamics & Interdisciplinary Research, National Academy of Sciences of Ukraine. Experimental results enable to verify the numerical procedure and calculation results as well as to distinguish flow features overlooked in the numerical studies. The “hot-gas” regime models the aspirator operation with a gas generator; it is tested experimentally using the commercial airbag gas generator technology in the laboratory of the Shanghai East Joy Long Motor Company.

## **METHOD OF INVESTIGATIONS AND INSTRUMENTATION**

The research approach consists in matched and feedback-connected numerical and experimental investigations. As guidance to build a supersonic ejector, the Prandtl-Meyer flow is considered [3, 5]. A supersonic jet-flow generated by a small gas generator should change its direction over the blunt angle coupling between a nozzle and a mixing chamber which causes a suction wave similar to that of Prandtl-Meyer flow. It is the proper pressure distribution in this area which motivates ejection of the atmospheric air into the mixing chamber.

Thus, the basic task of numerical simulation is to roughly determine the device geometry with its particular linear and angular dimensions which would create the required pressure fields in the inflator. To determine optimal operational parameters for the given geometry, instantaneous and integral gas-dynamic parameters are found for viscous incompressible gas using nonstationary Reynolds equations. To validate the numerical

problem formulation and used assumptions, 2 cases of “cold air” and “hot air” inflator operation are considered numerically. The first one imitates the laboratory conditions of the inflator operation using the compressed air tanks as a high-pressure source. The second one, models the situation of the inflator operation using a small pyrotechnic gas generator as the motive pressure source.

Obtained recommendations on slit, nozzle, mixing chamber parameters for a range of high motive pressure are taken as a basis for the engineering design which resulted in the detailed technological drawings and precision manufacture of the model.

The experimental task is to provide, thorough measurements of pressure fields in the aspirator system, a description of the jet behavior and, consequently, the air entrainment process. In addition to the measured values of aspiration ratio for different models and their operation conditions, this is visualized with the video recordings of airbag deployments using a high-speed camera.

**Experiment arrangement. Test models.**

The “cold air” system operation is realized experimentally due to the specially designed universal high-speed valve (UHSV-1). Its basic parameters are given in the Table 1.

*Table 1.*

*Basic operating parameters of the UHSV-1 high-speed valve*

Opening time	≤ 0.004 s
Closing time	≤ 0.005 s
Pressure range	0.6-6 MPa
Temperature range	+5 °C ÷ +65 °C
Supply voltage	80±6 V
Material	Steel 14X17H2
Dimensions	79 mm x 125 mm x 141mm
Weight	3 kg

These parameters enable to form a motive pulse jet from the nozzle to initiate the ambient air entrainment into the inflator mixing chamber as it is shown in Figure 3.

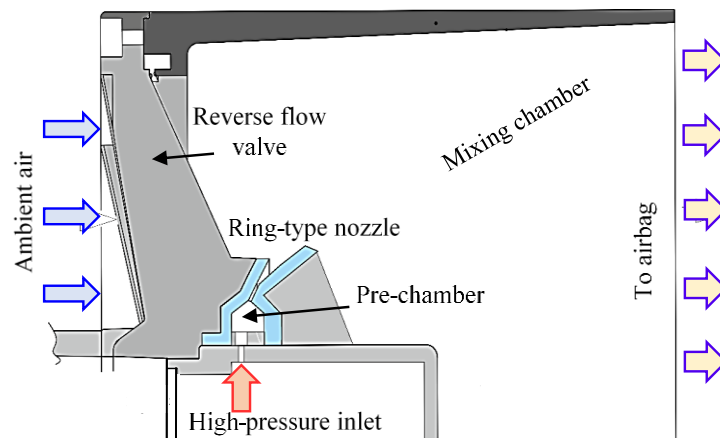


*Figure 3. Sketch of an axisymmetric design of the aspirated inflator according to the numerically outlined geometry*

A nozzle for the supersonic flow is designed to match the output pressure in the jet with the pressure in the mixing chamber. Consecutive investigation stages covered a range of varying angles of the slit and nozzle opening, slit width, geometry and sizes of pre-chamber and mixing chamber to determine an optimal set of design parameters.



Several aspirator models were designed, manufactured and tested as is partly described in [2-4]. They are axisymmetric following an overall design of the system to be located in the steering wheel. An essential feature of the first set is an external slit relative to the mixing chamber, i.e. the motive ring-type nozzle was located close to the internal wall of a mixing chamber. The second type combines aspirators with an internal slit ejecting the ring jet closer to the aspirator axis. The second type is considered here with its design illustrated by Figures 4 and 5.

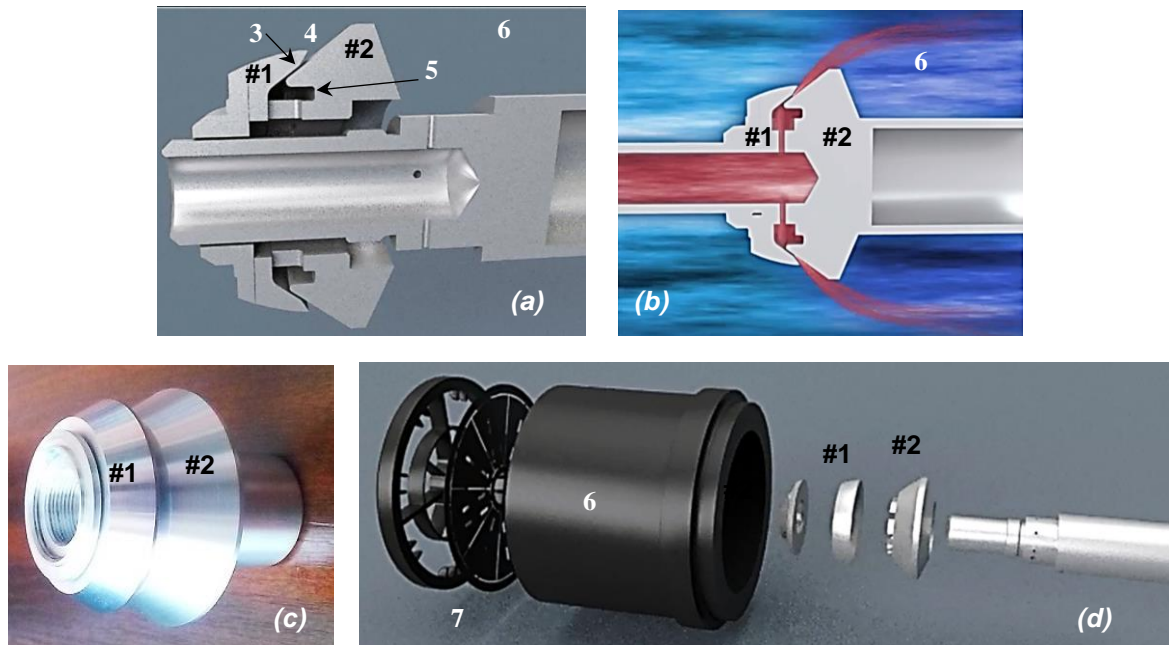


**Figure 4. Internal-slit aspirated inflator: 3D model (a); aspirator operation (b); fabricated test model (c); aspirator assembly (d).  
 #1, #2 – two metal disks forming a relevant nozzle geometry for a supersonic jet injection,  
 3 – slit,  
 4 – nozzle,  
 5 – pre-chamber,  
 6 – plastic mixing chamber/housing,  
 7 – reverse flow valve**

The sharp bent edge of one of the metal disks #1 or #2 is designed to realize the Prandtl-Meyer flow conditions. The whole design of the supersonic pulse ejector is to be substantially different from known ejectors made for operation in stationary flow conditions. Two basic design modifications of the internal-slit aspirator are shown in Figure 5. Other tested modifications embrace combinations of varied linear and angular dimensions of the basic aspirator elements like a slit, nozzle, pre-chamber, location of a motive pressure outlet in the pre-chamber, and mixing chamber including its shape, cylindrical or conical.

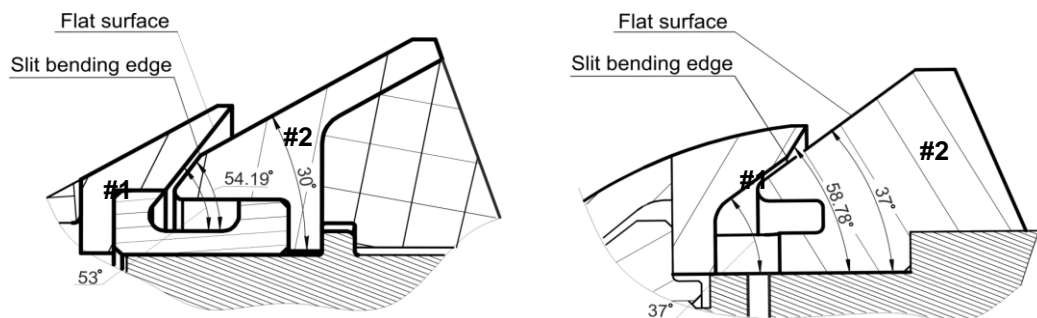


**Figure 5. Geometry of the slit initiating aspiration in the internal-slit aspirator design, 2 versions:  
 (a) aspirator #1; (b) aspirator #2**



Overall dimensions were maintained the same according to the engineering requirements, i.e. the aspirator length is no more than 117 mm, its diameter is 120 mm.

Finally, an attempt was made to stabilize the supersonic jet with streamwise grooves over the #2 disk with the circumferentially regular spacing (Figure 6, a) for several values of a filling factor,  $F=c/C=6.7\%$ ,  $13.3\%$ ,  $26.7\%$ ,  $53.3\%$ ,  $100\%$  (Figure 6, b) [see 7-9]. Effective slit width was calculated to vary within  $d=0.35\text{mm}$ — $0.45\text{mm}$ .

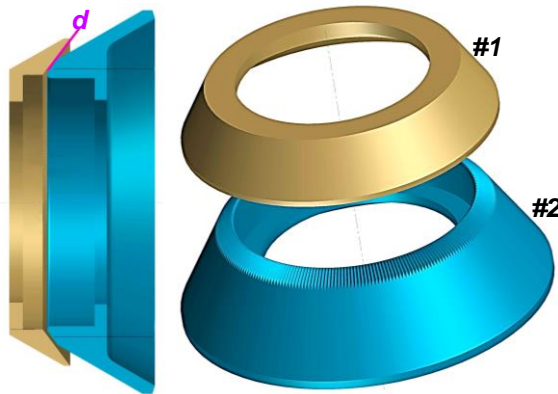


**Figure 6, a. Grooved disk #2 modified to stabilize behavior of the supersonic jet**

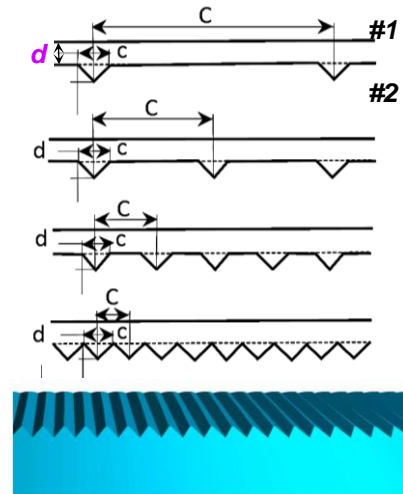


**Figure 6, b. Grooved surface with various filling factors**

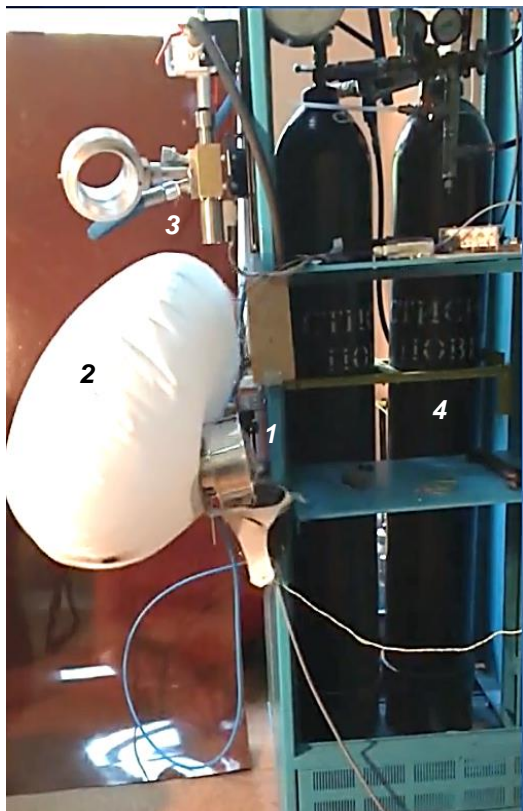


**Figure 7. Experimental facility [2, 4, 10]:**

- 1 – aspirated inflator model;**
- 2 – airbag;**
- 3 – high-speed valves;**
- 4 – compressed air tanks, 0-100 bar**

(2-10 locations shown in Figure 8, b). A number of other pressure probes are mounted so as to measure static pressure values along the mixing chamber wall (11-15 locations) and in the pre-chamber (probe location 1).

### Experimental facility

The stage of experimental testing of the inflator operability started from the design and manufacturing of the compressed-air facility (Figure 7) and a number of appliances including the automated data acquisition and processing system, pressure-probe rakes, the aspiration ratio stand, etc.

During testing, the air is pumped into the 40-L high-pressure 250 bar tank by the high-pressure PE-100W compressor up to 100 bar. From this tank, air goes to the 40-L receiver of 150 bar through a reduction valve. The reduction valve is adjusted according to the range of motive pressure values,  $P_m$ , required in experiments. The UHSV-1 electronically controlled and the alternative commercial KB-20 pneumatically controlled high-speed valves are switched in the pneumatic tract. High-pressure sensors for 1-70 bars are mounted after each valve to measure pressure losses. Due to very short opening and closing time, high-speed valves form a jet flow within 20-40 ms similar to gas generators to initiate the ambient air entrainment as it is shown in Figure 4, b. Excessive pressure in the airbag is 0.2 bar that stops the inflation process.

The measurement program aims at the determination of the supersonic jet location and behavior inside a mixing chamber to find conditions for stable air entrainment. For that, corresponding to the particular inflator design, the pressure-probe rake (Figure 8, a) is fabricated to measure dynamic pressure at the mixing chamber outlet

Other series of experiments were conducted under the same conditions with an airbag mounted to the inflator outlet. The process of airbag deployment is recorded using a high-speed 1000 f/s camera. It enables the analysis of the visualized inflation process together with corresponding measured pressure distributions.

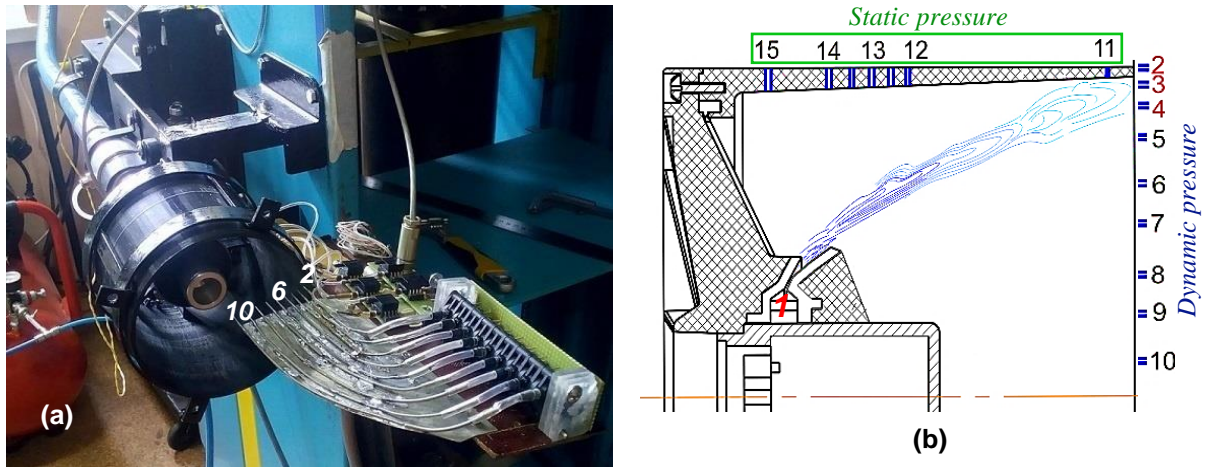


Figure 8. Pressure probe rake (a) and numbering of pressure probes (b)

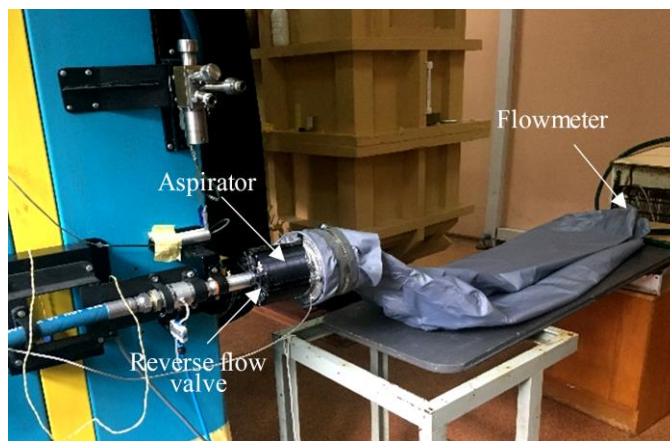


Figure 9. Stand for aspiration ratio measurements

The series of experimental tests is completed with measurements of the aspiration ratio values depending on motive pressure for every tested inflator design. Figure 9 shows the stand for aspiration ratio,  $A$ , measurements. It uses a 200 L bag mounted to the inflator outlet and to the flowmeter to measure the air volumes with and without the operating aspirated inflator:

$$A = \frac{V_{bag \text{ with aspiration}}}{V_{bag \text{ without aspiration}}}$$

Automated remote control of experimental runs and simultaneous data processing is illustrated in Figure 10.



Figure 10. Automated remote experiment control

## RESULTS AND DISCUSSION

The key feature of the formulated multivariate problem is a certain compromise between an optimal aspirator geometry with its specified dimensions and optimal parameters of its operation. This compromise is the only solution to satisfy the given engineering requirements. Thus, it is important to determine experimentally the ranges of acceptable operational parameters for an outlined aspirator design such as motive pressure  $P_m$  as well as a dominant jet direction and intensity within the aspirator housing (mixing chamber) which would result in the best air entrainment.

## Pressure measurements

Pressure fields are measured in a process of air aspiration using 15 pressure probes distributed around the mixing chamber interior and in the inflator nozzle (Figure 8). #1 probe measures pressure in the nozzle, ##2-10 probes register the dynamic pressure at the exit from the mixing chamber, ##11-15 probes show the static pressure along the mixing chamber wall. The obtained patterns of the type shown in Figure 11 enable the reconstruction of the jet behavior (intensity, shape and location) to determine its optimal location for best aspiration for a given aspirator model depending on the operational motive pressure  $P_m$ . The latter is correlated with a video-recorded airbag inflation process as well as with the measured values of aspiration ratio. For instance, jet instability can result in a significantly decreased entrainment of ambient air despite growing  $P_m$ .

The ejecting slit width,  $d$ , is a key parameter varied in experiments stepwise as 0.25, 0.35, 0.40, 0.45 mm within a pressure range of  $P_m=18-60$  bar. Sets of measurements are made for  $P_m$  growing with a step of  $P=1-3$  bar.

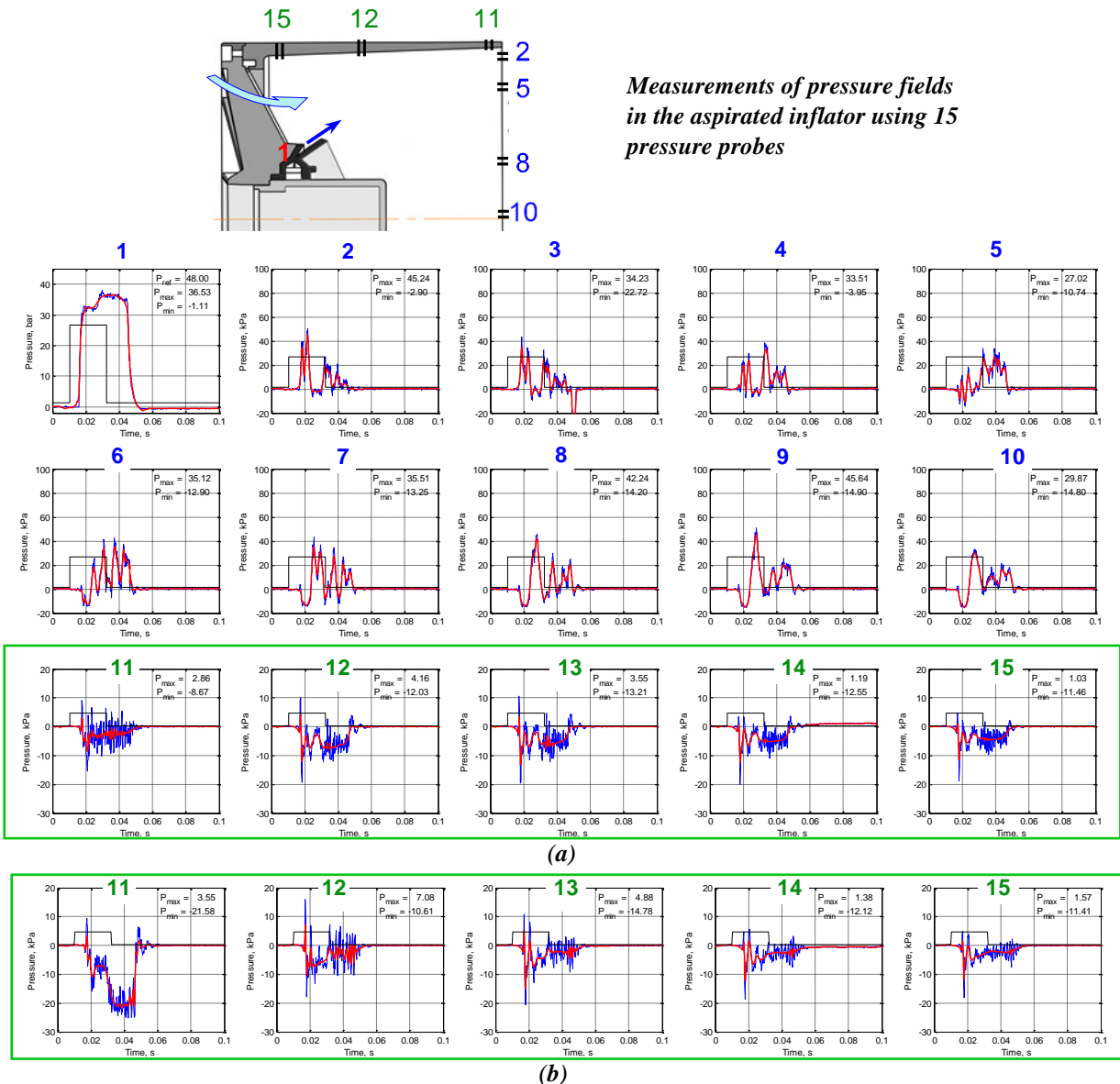


**Figure 11.** Measured dynamic pressure, 1-10, and static pressure, 11-15;  $d=0.4$  mm;  $P_m = 48$  bar (a); measured static pressure, 11-15 probes;  $d=0.4$  mm;  $P_m = 51$  bar (b)

Figure 11 shows a pretty wide jet flow with a moderate intensity distinguished by probes 2-10. Vacuum static pressure provides the air suction from the aspirator inlet with a reverse flow valve.  $P_m$  increased from 48 to 51 bar shows an area in the axial part (6-10 probes) with a formed reverse flow though maintained suction along the aspirator wall (Figure 11, b). A possibility to eliminate this flow instability was investigated on the basis of



earlier fundamental flow control studies [7-9]. Here, it was implemented using a modified disk surface shown in Figures 6 and 12. Formed circumferential flow regularity resulted in a much more intense flow in the aspirator mixing chamber especially near its peripheral part registered by ##2-5 probes. Simultaneously, it noticeably reduced the axial reverse flow.

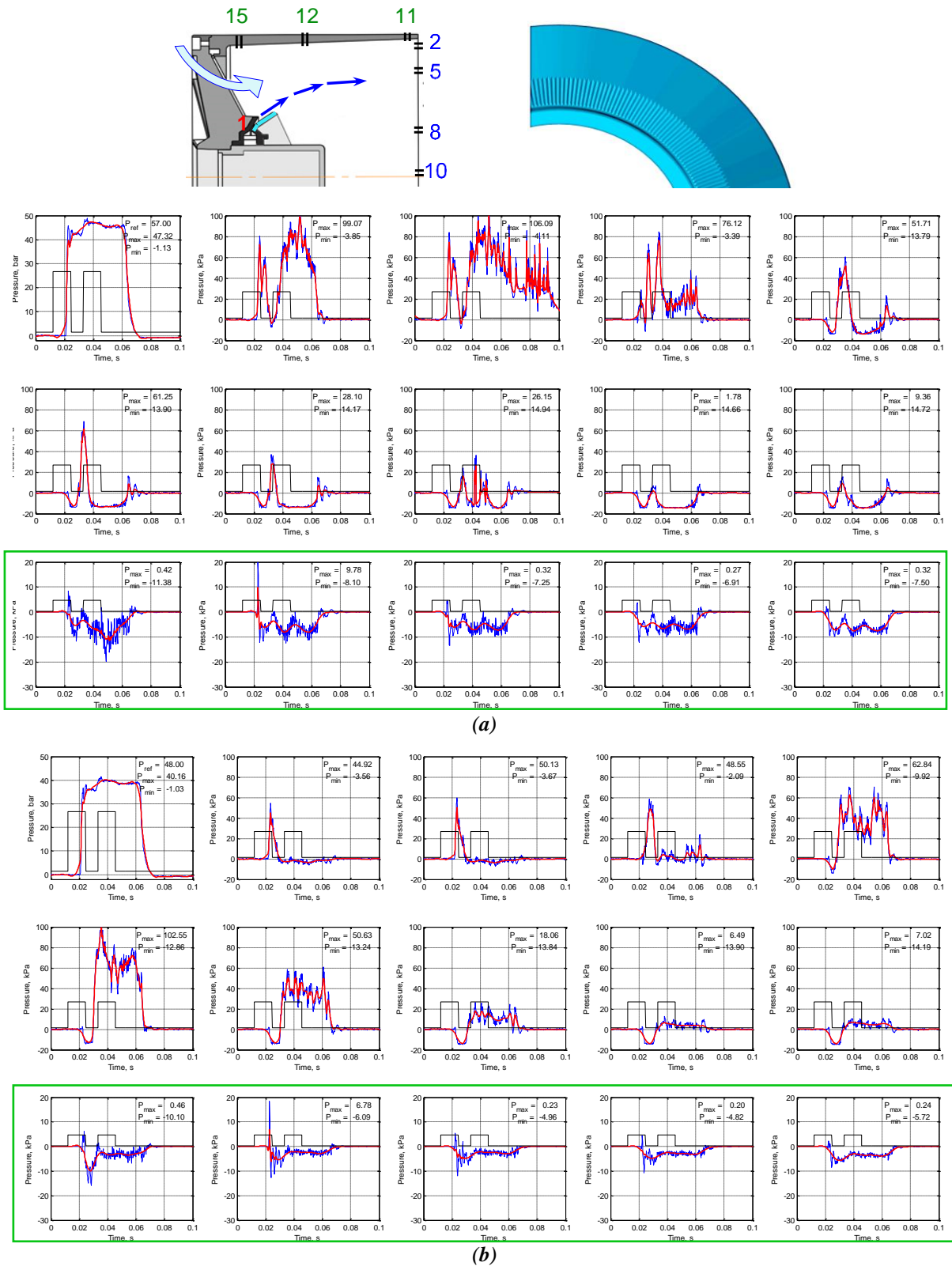


Figure 12. Measured pressure fields in the aspirated inflator with a grooved surface of #2 disk, filling factor  $F=53$ , 3% (see Figure 6, b);  $d_{eff}=0.4$  mm;  $P_m = 57$  bar (a) and  $P_m = 48$  bar (b).

The modified design with  $F=53.3\%$  resulted in the slightly enlarged slit width from 0.35 to 0.4 mm and demonstrated its operability in a wider range of motive pressure. Results of Figures 12, a, b obtained for  $P_m = 57$  bar and 48 bar as well as for the values beyond this range do not differ as drastically as in the case of a smooth disk surface, while the values of suction pressure are more uniform along the aspirator mixing chamber.

### Airbag inflation

A high-speed camera was used for video-recording of the airbag inflation within 30, 35, 40 ms, the inflation time having been regulated by a high-speed valve. Aspirators with a varying slit width were tested in a pressure range of 24-60 bar with a step of 3 bar. Figure 13 shows a sequence of pictures characterizing the airbag process inflation using optimized operation parameters for the aspirator design of Figure 5, a.  $P_m$  increased to 50 and 55 bar also showed good airbag inflation.

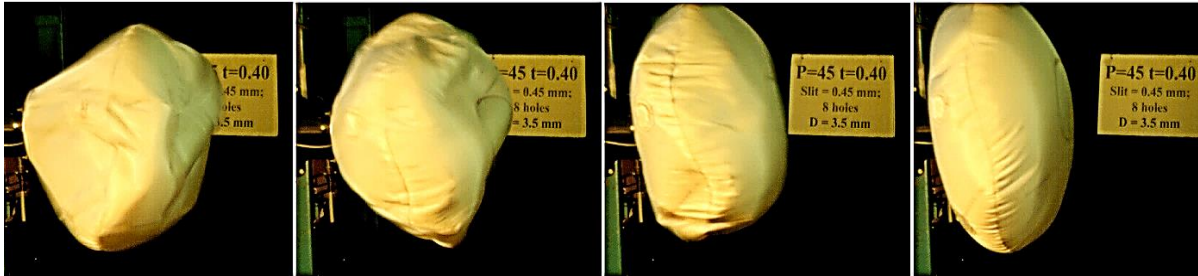


Figure 13. Successive stages of the airbag inflation process:  $d=0.35$  mm;  $P_m = 45$  bar.

Thus, the video-recorded inflation process of an airbag supplemented results of pressure measurements and enabled to recommend optimal sets of parameters for a given inflator design. These recommendations were also confirmed by aspiration ratios measured for various experimental conditions.

### Measurements of the aspiration ratio

Values of aspiration ratio were measured both for the smooth model design of Figure 5, a and the grooved disk #2 surface of Figures 6 and 12. A 200-liter bag was connected to the aspirated inflator and to the flowmeter to enable the air easy filling with further volume measurement. Statistically obtained A values for every case of design and flow parameters are shown in Figure 14 where numerically obtained curves are placed for comparison, the red curve having described the “cold-gas case” comparable with experiments.

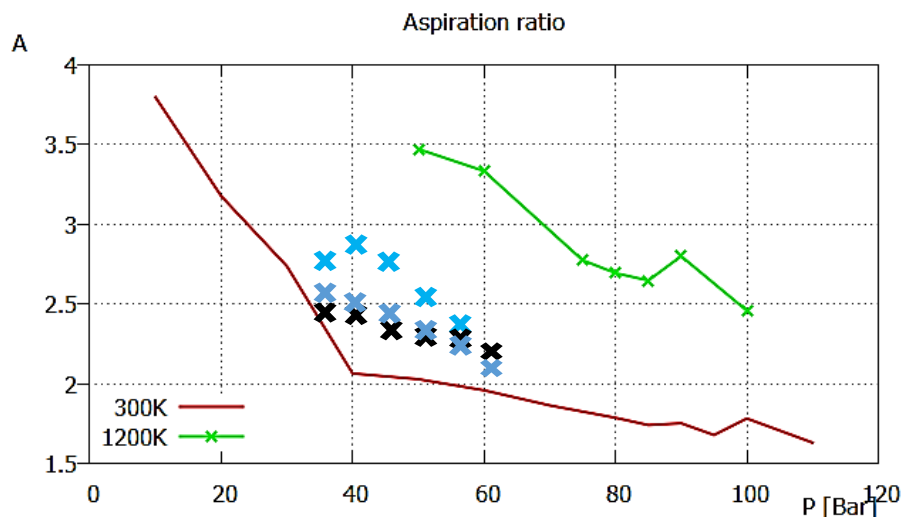


Figure 14. Aspiration ratio for cold (red curve) and hot (green curve) gas found numerically;  
 × - experiment, baseline smooth disk surfaces;  
 × - experiment, grooved surface,  $F=6.7\%$ ;  
 × - experiment, grooved surface,  $F=53.3\%$

All of the experimental aspiration ratio values are higher of the numerical values. Therefore, taking into account 1.5-2 times higher hot gas volume aspiration, one can expect to satisfy the engineering requirement of  $A \geq 4$  in case of the aspirated inflator initiated with a pyrotechnic gas generator. The combination of design and operation parameters play a significant role in the inflator operation which can be optimized using a proper choice of these parameters.

## CONCLUSIONS

The aspirated inflation system is developed for a 50 L driver's airbag with an aspiration ratio,  $A \geq 4$  which can be applicable for airbags of larger sizes. It provides the air entrainment into an airbag from the car passenger compartment due to the realized Prandtl-Meyer supersonic jet flow over a bent nozzle wall. The jet motivating the air entrainment is generated by a small gas generator; its operation is imitated in experiments by a system of high-pressure tanks controlled by a high-speed valve. One of the features built into the design is the 0.2 bar overpressure in the airbag which discontinues the air entrainment that stops airbag deployment on contact with an occupant and thus eliminates out-of-position occupant injuries.

The experimental investigation of the system operation is a multivariate problem where optimal combinations of design geometry and operation parameters are sought. The built experimental facility, appliances, automated measurement complex, and several manufactured and tested models enabled the validation of the numerical approach and results and to show the potential of the developed aspirated inflator.

Various modifications of the design including the circumferential surface regularity over one ring wall of the nozzle can result in noticeable variation of the motive jet behavior. As such, it can be stabilized providing a wider range of acceptable parameters for optimal inflator operation. In its turn, it can be very important in terms of less severe requirements to flatness of pressure curve produced by a pyrotechnic gas generator and thus to the motive gas generator itself.

## REFERENCES

- [1] Breed, David S. (2014), "Steering Wheel Mounted Aspirated Airbag System", United States Patent No. US20140361522A1, Pub. date: Dec. 11, 2014.
- [2] Kuzmenko, K., Yurchenko, N., Vynogradskyy, P., Paramonov, Y. Optimization of ejector design and operation. EPJ Web of Conferences Volume 114, 2016, 02063-p.1-4
- [3] D. Breed, G. Voropaiev, N. Yurchenko, Yu. Paramonov, A. Koshil. Airbag inflators including aspirators, *Internat. Patent Application Number PCT/US2018/013088, Int. Publication # WO 2018/132420 A1, published 19 July 2018.*
- [4] David Breed, \*Nina F. Yurchenko, Pavlo M. Vynogradskyy, Konstantin Kuzmenko, Yuriy Paramonov, Novel inflation system for airbags, *Proc. AASEM18/Structures18 Symposium Proceedings, Incheon, Korea, 2018, 27-31 Aug., [http://www.i-asem.org/publication\\_conf/structures18/12.ICAAE18/XH3A.1.AE1761\\_4762F3.pdf](http://www.i-asem.org/publication_conf/structures18/12.ICAAE18/XH3A.1.AE1761_4762F3.pdf).*
- [5] D. Breed, S. Zhang, N. Yurchenko, G. Voropaiev, Development of an aspirated inflator for preventing out-of-position occupant injuries. *Proc. 14<sup>th</sup> Int. Symp. on Sophisticated Car Safety Systems, Mannheim, Germany, 2018, Nov. 26-28, 17 pp.*
- [6] Kyoung-Su Im, Zeng-Chan Zhang, Grant. O. Cook Jr. Airbag Inflator Models in LS-DYNA. Proc. 14<sup>th</sup> Int. LS-DYNA Users Conf., June 2016.
- [7] Yurchenko, N. A method of active boundary-layer control over bodies of complex geometry, 2009, "Patent of Ukraine № 45240 (registered in Ukr. Patenting Office 26.10.2009)
- [8] Yurchenko, N.F. Energy-efficient flow control around blunt bodies, *Intl. J. of Advances in Aircraft and Spacecraft Science*, DOI: [http://dx.doi.org/10.12989/aas](http://dx.doi.org/10.12989/aas.2013.1.1.000). 2013.1.1.000. V. 1, No. 1, pp. 15-25.
- [9] N. Yurchenko. Smart flow control based on generated spanwise flow regularity. *Lecture, 4 Dec. 2018, Dep of Chemical/Applied Sciences, Delft University of Technology, Netherlands.*
- [10] Aerodynamic Complex for Interdisciplinary Research with an integrated system for data acquisition and processing. N. Yurchenko, P. Vynogradskyy, Yu. Paramonov, V. Tsymbal, A. Koshil, K. Kuzmenko, R. Pavlovsky, A. Zhdanov, 2012, *Proc. World Congress "Aviation in the XXI-st Century", Kyiv, Ukraine (in Russian).*